

(2)

**ELECTRO-OPTICS DISPLAY RESEARCH, TEST, AND
EVALUATION LABORATORY PROGRAM**

AD-A270 947



Final Report

Dr. Mohammad A. Karim and Dr. Donald L. Moon

June 29, 1993

U. S. Army Research Office

DAAL03-87-K-0121

**University of Dayton
Dayton, Ohio**



93-24973



Approved for Public Release

Distribution Unlimited

REPORT DOCUMENTATION PAGE

Form Approved
OMB No 0704-0188

Public reporting burden for this collection of information is estimated to average 1 hour per response, including the time for reviewing instructions, searching existing data sources, gathering and maintaining the data needed, and completing and reviewing the collection of information. Send comments regarding this burden estimate or any other aspect of this collection of information, including suggestions for reducing this burden, to Washington Headquarters Services, Directorate for Information Operations and Reports, 1215 Jefferson Davis Highway, Suite 1204, Arlington, VA 22202-4302, and to the Office of Management and Budget, Paperwork Reduction Project (0704-0188), Washington, DC 20503.

1. AGENCY USE ONLY (Leave blank)		2. REPORT DATE 6/29/93	3. REPORT TYPE AND DATES COVERED FINAL Sept. 1987 - June 1993	
4. TITLE AND SUBTITLE Electro-Optics Display Research, Test, and Evaluation Laboratory Program			5. FUNDING NUMBERS DAA03-87-K-0121	
6. AUTHOR(S) M. A. Karim and D. L. Moon				
7. PERFORMING ORGANIZATION NAME(S) AND ADDRESS(ES) University of Dayton Electrical Engineering Department 300 College Park Avenue Dayton, OH 45469-0226			8. PERFORMING ORGANIZATION REPORT NUMBER	
9. SPONSORING / MONITORING AGENCY NAME(S) AND ADDRESS(ES) U.S. Army Research Office P. O. Box 12211 Research Triangle Park, NC 27709-2211			10. SPONSORING / MONITORING AGENCY REPORT NUMBER ARO 25557.10-EL	
11. SUPPLEMENTARY NOTES The views, opinions and/or findings contained in this report are those of the author(s) and should not be construed as an official Department of the Army position, policy, or decision, unless so designated by other documentation.				
12a. DISTRIBUTION / AVAILABILITY STATEMENT Approved for public release; distribution unlimited.			12b. DISTRIBUTION CODE	
13. ABSTRACT (Maximum 200 words) The goal of the research effort is to analyze and develop model to characterize overall electro-optical display systems of particular interest to US Army Center for Night Vision and Electro-Optics at Ft. Belvoir, Virginia. The main thrust of the research reported herein is to implement accepted standards for evaluating displays, take an active role in forming new measurement standards, and provide unbiased evaluation of displays in use or contemplated for military missions. Measurement parameters include display brightness, contrast, resolution, chromatic range, frequency response, angular field-of-view, reliability, and sensitivity to environment. Another important facet of this research is to determine image dynamics involving the response time between sensor input and the reaction of the observer for influencing what display improvements, such as variable acuity displays, color, contrast, or brightness lead to significant improvement in performance.				
14. SUBJECT TERMS Infrared imaging systems, modulation transfer function, minimum resolvable temperature difference, signal-to-noise ratio, contrast transfer function, impulse response.			15. NUMBER OF PAGES 60	
			16. PRICE CODE	
17. SECURITY CLASSIFICATION OF REPORT UNCLASSIFIED	18. SECURITY CLASSIFICATION OF THIS PAGE UNCLASSIFIED	19. SECURITY CLASSIFICATION OF ABSTRACT UNCLASSIFIED	20. LIMITATION OF ABSTRACT UL	

TABLE OF CONTENTS

	Page
I. Cover letter	1
II. Table of Contents	2
III. List of Appendixes	3
IV. Final Report	4
V. Appendixes	7

[REDACTED]

Accession For	
NTIS GRA&I	<input checked="" type="checkbox"/>
DTIC TAB	<input type="checkbox"/>
Unannounced	<input type="checkbox"/>
Justification	
By _____	
Distribution/ _____	
Availability Codes	
Dist	Availability
A-1	

LIST OF APPENDIXES

J. C. Feltz, and M. A. Karim, "Modulation transfer function of charge-coupled devices," Applied Optics, Vol. 29, pp. 717-722, 1990.

M. L. Gao, S. H. Zheng, M. A. Karim, and D. L. Moon, "Restoration of dynamically degraded gray level images in phosphor based display devices," Optical Engineering, Vol. 29, pp. 878-882, 1990.

J. C. Feltz, "Development of the modulation transfer function and contrast transfer function for discrete systems, particularly charge-coupled devices," Optical Engineering, Vol. 29, pp. 893-904, 1990.

M. L. Gao, M. A. Karim, and S. H. Zheng, "Device nonspecific minimum resolvable temperature difference for infrared imaging systems characterization," Optical Engineering, Vol. 29, pp. 905-910, 1990.

A. A. S. Awwal, A. K. Cherri, M. A. Karim, and D. L. Moon, "Dynamic modulation transfer function of a display system," Applied Optics, Vol. 30, pp. 201-205, 1991.

A. K. Cherri, A. A. S. Awwal, M. A. Karim, and D. L. Moon, "Restoration of moving binary images degraded owing to phosphor persistence," Applied Optics, Vol. 30, pp. 3734-3739, 1991.

M. L. Gao, M. A. Karim, and S. H. Zheng, "Device nonspecific dynamic performance model for thermal imaging systems," Optical Engineering, Vol. 30, pp. 1779-1783, 1991.

M. A. Karim, M. L. Gao, and S. H. Zheng, "Minimum resolvable temperature difference model: a critical evaluation," Optical Engineering, Vol. 30, pp. 1788-1796, 1991.

Introduction

This final report describes the results obtained on a research effort entitled "Electro-Optics Display Research, Test and Evaluation Laboratory Program" funded by the U. S. Army Research Office contract DAAAL03-87-K-0121.

STATEMENT OF THE PROBLEM

The goal of the research effort is to analyze and develop model to characterize overall electro-optical display systems of particular interest to US Army Center for Night Vision and Electro-Optics at Ft. Belvoir, Virginia. The main thrust of the research reported herein is to implement accepted standards for evaluating displays, take an active role in forming new measurement standards, and provide unbiased evaluation of displays in use of contemplated for military missions. Measurement parameters include display brightness, contrast, resolution, chromatic range, frequency response, angular field-of-view, reliability, and sensitivity to environment. Another important facet of this research is to determine image dynamics involving the response time between sensor input and the reaction of the observer for influencing what display improvements, such as variable acuity displays, color, contrast, or brightness lead to significant improvement in performance.

SUMMARY OF THE MOST IMPORTANT RESULTS

1. A theoretical model for characterizing the dynamic response of a non-scanning electro-optic display system is developed. The model interrelates the spatial frequency degradations of an image display with both phosphor characteristics and relative velocity of the displayed object. Thereafter, the analysis is extended to compare the performances of types P-20, P-42, and P-1052 phosphor based displays.
2. The degraded images of dynamic objects obtained by using a phosphor-based electro-optical display are analyzed in terms of dynamic modulation transfer function (DMTF) and temporal characteristics of the display system. The direct correspondence between the DMTF and image smear is used in developing real-time techniques for the restoration of degraded images.
3. The concepts of dynamic modulation transfer function (DMTF) and degree of degradation (DD) are used for analyzing gray level image display of a phosphor based display system. Real-time restoration of the motion-degraded display images may be accomplished using one or more inverse filters whose characteristics depend on the magnitude and direction of the motion. Both DMTF and DD characteristics are used in the restoration of motion-degraded images.

4. A method for calculating the modulation transfer function (MTF) of charge-coupled devices (CCD) is presented. The analysis accommodates both the time- and space-variant properties of CCDs as well as input images moving with constant velocity within a scan interval. The model developed accounts for both the static and the dynamic MTF of CCD imaging systems.

5. The modulation transfer function (MTF) and contrast transfer function (CTF) are considered for discrete systems. The MTF and CTF are derived for the charge-coupled device (CCD). The analysis presented considers the full effects of sampling on device response. Experimental tests of the CTF for a line-array CCD are presented. The MTF and CTF are shown to be multi-valued functions for discrete systems.

6. A generalized minimum resolvable temperature difference (MRTD) formulation is identified for the characterization of infrared detection systems. The generalized MRTD equation can be adapted to suit the needs of any IR system to be tested. As an illustration, the MRTD of a staring IR detection system is derived from the generalized MRTD formulation.

7. A device nonspecific dynamic minimum resolvable temperature different performance model is developed for characterizing thermal imaging systems capable of displaying moving targets.

8. Discrepancies between the predicted minimum resolvable temperature difference (MRTD) and field performances are indicative of the fact that the modeling of MRTD has certain inherent problems. Several sources for MRTD error are identified. MRTD is found to be a special case of a more general minimum resolvable luminance difference (MRLD) measure. The MRLD measure involves absolute temperature and can be used to describe more generic targets.

LIST OF PUBLICATIONS GENERATED

The research effort resulted into eight refereed journal publications in Applied Optics and Optical Engineering. They are listed below:

J. C. Feltz, and M. A. Karim, "Modulation transfer function of charge-coupled devices," Applied Optics, Vol. 29, pp. 717-722, 1990.

M. L. Gao, S. H. Zheng, M. A. Karim, and D. L. Moon, "Restoration of dynamically degraded gray level images in phosphor based display devices," Optical Engineering, Vol. 29, pp. 878-882, 1990.

J. C. Feltz, "Development of the modulation transfer function and contrast transfer function for discrete systems, particularly charge-coupled devices," Optical Engineering, Vol. 29, pp. 893-904, 1990.

M. L. Gao, M. A. Karim, and S. H. Zheng, "Device nonspecific minimum resolvable temperature difference for infrared imaging systems characterization," Optical Engineering, Vol. 298, pp 905-910, 1990.

A. A. S. Awwal, A. K. Cherri, M. A. Karim, and D. L. Moon, "Dynamic modulation transfer function of a display system," Applied Optics, Vol. 30, pp. 201-205, 1991.

A. K. Cherri, A. A. S. Awwal, M. A. Karim, and D. L. Moon, "Restoration of moving binary images degraded owing to phosphor persistence," Applied Optics, Vol. 30, pp. 3734-3739, 1991.

M. L. Gao, M. A. Karim, and S. H. Zheng, "Device nonspecific dynamic performance model for thermal imaging systems," Optical Engineering, Vol. 30, pp. 1779-1783, 1991.

M. A. Karim, M. L. Gao, and S. H. Zheng, "Minimum resolvable temperature difference model: a critical evaluation," Optical Engineering, Vol. 30, pp. 1788-1796, 1991.

These articles are included in the appendix.

PARTICIPATING SCIENTIFIC PERSONNEL

The scientific personnel supported by this project included two faculty members,

Dr. Donald L. Moon, PI
Dr. Mohammad A. Karim,

and seven graduate research assistants. All of these graduate students were pursuing and eventually received advanced degrees in electrical engineering as summarized below.

Mr. Dean Adams,	M.S.
Mr. Abdul Awwal,	Ph.D.
Mr. Abdallah Cherri,	Ph.D.
Mr. John C. Felz,	M.S.
Mr. Ming-Lun Gao,	Ph.D.
Mr. Robert A. Michaels,	M.S.
Ms. Song-Hua Zheng,	Ph.D.

Modulation transfer function of charge-coupled devices

John C. Feltz and Mohammad A. Karim

A method for calculating the modulation transfer function (MTF) of charge-coupled devices (CCD) is presented. The analysis accommodates both the time- and space-variant properties of CCDs as well as input images moving with constant velocity within a scan interval. The model developed accounts for both the static and the dynamic MTF of CCD imaging systems.

I. Introduction

Charge-coupled devices (CCD) are discrete imaging systems in both time and space.¹ Imaging systems are generally characterized by the modulation transfer function (MTF), which assumes a linear space-invariant system.² Consequently, the MTF calculation, when applied to CCDs, poses a serious problem. CCDs are time and space variant at the scales needed to calculate the MTF, and therefore the MTF turns out to be a multivalued function. This multivaluation gives rise to the beating phenomenon when the MTF is measured repeatedly along a CCD.³ The multivaluation significantly reduces the utility of the MTF in specifying CCD hardware capabilities.

The MTF is a commonly used measure of the spatial frequency response of optical systems. Practical resolution limits of systems are commonly specified by MTF cutoff values. Because discrete imaging devices, particularly CCDs, and discrete display devices are useful and common devices, an extension of the MTF to discrete systems is necessary to provide continuity between continuous and discrete analysis and design procedures. The present work particularly examines the MTF of CCDs.

CCDs are most commonly fabricated with silicon MOS technology and a rectangular geometry. The significant feature of CCD operation for this analysis is the integration and sampling of the incident image in time and space. The aperture effect of this integration and sampling gives the limiting values of the MTF for CCDs.⁴ The goal of this work is to accurately predict the range of variation of the MTF for input

images of any spatial frequency and of constant velocity. Accordingly, this work extends the MTF definition for CCDs to account for variations of the MTF, as calculated at a particular location, due to alignment effects and images with constant velocity.

This work considers the case of uniform rectangular CCD pixels with linear response, both within a pixel and between pixels, when subjected to a monochrome illumination. Synchronous charge integration and charge transfer for all pixels is assumed for simplicity. Because the MTF is separable along the two pixel axes, the model developed is limited to one spatial dimension only. For simplicity of analysis, however, nonlinear effects such as blooming and incomplete charge transfer are not considered in this work.

II. Development of the CCD MTF Expression

We first consider the MTF expression for a static image, i.e., an image with no motion relative to the CCD. The expressions will then be expanded to handle image motion characterized by a constant velocity within one scan interval. The input illumination pattern for evaluation of the MTF is commonly given by²

$$I = 0.5[1 + \cos(s)], \quad (1)$$

where s is a general spatial parameter.

This input pattern specifies the charge generation rate in the active areas of the CCD, during the active charge generation time. The MTF is defined by the response of the CCD to the input:

$$\text{MTF} = \frac{B_{\max} - B_{\min}}{B_{\max} + B_{\min}}, \quad (2)$$

where B_{\max} and B_{\min} are the values of a neighboring maximum and minimum, respectively, of the output. For CCDs, B_{\max} and B_{\min} will be considered as the output of two specific pixels.

Figure 1 gives an illustration of the following parameters defined for the 1-D analysis:

T = period of input pattern (mm),

The authors are with University of Dayton, Department of Electrical Engineering, Dayton, Ohio 45469-0001.

Received 24 March 1989.

0003-6935/90/050717-06\$02.00/0.

© 1990 Optical Society of America.

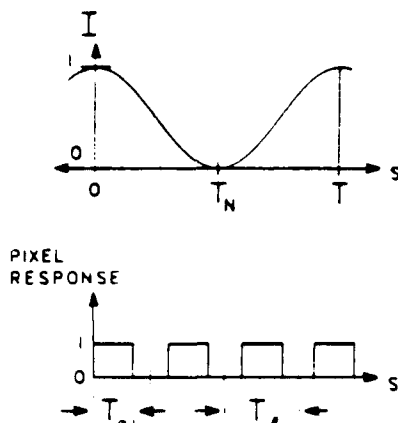


Fig. 1. Definition of spatial parameters.

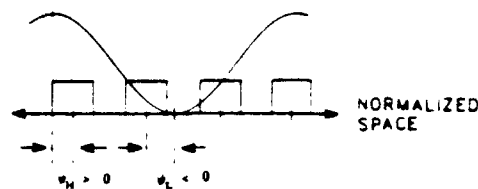


Fig. 2. Definition of offset parameters.

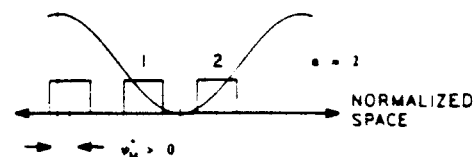


Fig. 3. Definition of pixel index and critical offset.

T_N = Nyquist period of input (mm),
 T_α = active width of CCD pixels (mm), and
 T_β = CCD pixel spacing, or pixel pitch (mm).
 We define the normalized pixel width α and the normalized pixel spacing β as

$$\alpha = \pi T_\alpha / T_N, \quad (3a)$$

$$\beta = \pi T_\beta / T_N, \quad (3b)$$

The alignment between the CCD pixels and the input pattern is important in calculating the MTF.³ Accordingly, we also define the following parameters in normalized units, as illustrated in Fig. 2:

ψ_H = offset between a maximum of the input pattern and the center of the nearest pixel (rad) and
 ψ_L = offset between a minimum of the input pattern and the center of the nearest pixel (rad).

These offsets, or phase parameters, are limited by

$$-\frac{\beta}{2} \leq \psi_H \leq \frac{\beta}{2}, \quad (4a)$$

$$-\frac{\beta}{2} \leq \psi_L \leq \frac{\beta}{2}. \quad (4b)$$

For any arbitrary input pattern period, once a pixel generating B_{\max} is determined, there are in general two pixels which could generate B_{\min} , depending on ψ_H . If ψ_H is gradually scanned from $-\beta/2$ to $\beta/2$, the location of B_{\min} will change from one pixel to the next. We define ψ_H^* to represent the critical value of ψ_H , corresponding to the case when the minimum of the input pattern lies at the boundary between two pixels, as shown in Fig. 3. Accordingly, the pixel index n is given by

$$n = \text{int}(T_N/T_\beta) + 1, \quad (5)$$

where $\text{int}(x)$ represents the integer value of x , so that

$$\psi_H^* = \pi - (n - 1/2)\beta. \quad (6)$$

These definitions for n and ψ_H^* allow ψ_L to be expressed as

$$\psi_L = \psi_H + k\beta, \quad (7)$$

where

$$k = \begin{cases} n: & \psi_H \leq \psi_H^* \\ n-1: & \psi_H > \psi_H^* \end{cases} \quad (8)$$

The above definition of ψ_L removes the uncertainty over the location of B_{\min} and makes ψ_L a function of ψ_H and the physical dimensions. When ψ_H is less than ψ_H^* , B_{\min} is generated by the pixel n pixels distant from the pixel generating B_{\max} . When ψ_H is greater than ψ_H^* , B_{\min} is generated in the pixel $(n-1)$ pixels distant from the pixel generating B_{\max} . When ψ_H equals ψ_H^* , the two pixels n and $(n-1)$ distant, bordered by the input minimum, generate equal values for B_{\min} .

B_{\max} and B_{\min} are defined, respectively, as

$$B_{\max} = \int_{\psi_H - \alpha/2}^{\psi_H + \alpha/2} 0.5[1 + \cos(\theta)] d\theta \\ = 0.5[\alpha + 2 \sin(\alpha/2) \cos(\psi_H)], \quad (9)$$

$$B_{\min} = \int_{\psi_L - \alpha/2}^{\psi_L + \alpha/2} 0.5[1 + \cos(\theta)] d\theta \\ = 0.5[\alpha + 2 \sin(\alpha/2) \cos(\psi_L)]. \quad (10)$$

Using Eq. (2), (9), and (10), we determine the CCD MTF for static images to be

$$\text{MTF} = \frac{\sin(\alpha/2)[\cos(\psi_H) - \cos(\psi_H + k\beta)]}{\alpha + \sin(\alpha/2)[\cos(\psi_H) + \cos(\psi_H + k\beta)]}, \quad (11)$$

where k has already been described by Eq. (8). Note that, when $k\beta = \pi$, $\psi_L - \psi_H = \pi$. This special case occurs when T_N/T_β is an integer. For this special case, the MTF reduces to

$$\text{MTF} = \frac{2 \sin(\alpha/2) \cos(\psi_H)}{\alpha}. \quad (12)$$

A dynamic MTF⁵ is calculated next by using a moving image. To incorporate linear motion, the following additional terms may be defined:

v = image velocity (mm/s),

γ = CCD charge integration time (s), and

δ = CCD scan interval (s).

For simplicity, a normalized velocity ν (rad/s) is defined as

$$\nu = \pi v / T_v \quad (13)$$

For the sake of consistency with the static MTF expression, the parameters ψ_H , ψ_L , ψ_H , n , and k are defined at the center of a scan time, as illustrated in Fig. 4.

The expressions for B_{\max} and B_{\min} for the dynamic case are defined, respectively, as

$$B_{\max} = \int_{t=-\gamma/2}^{\gamma/2} \int_{\theta=\psi_H+\pi/2-\alpha/2}^{\psi_H+\pi/2+\alpha/2} 0.5[1 + \cos(\theta)] d\theta dt$$

$$= 0.5[\alpha\gamma + (2/\nu) \sin(\alpha/2) \sin(\nu\gamma/2) \cos(\psi_H)], \quad (14)$$

$$B_{\min} = \int_{t=-\gamma/2}^{\gamma/2} \int_{\theta=\psi_L+\pi/2-\alpha/2}^{\psi_L+\pi/2+\alpha/2} 0.5[1 + \cos(\theta)] d\theta dt$$

$$= 0.5[\alpha\gamma + (2/\nu) \sin(\alpha/2) \sin(\nu\gamma/2) \cos(\psi_L)]. \quad (15)$$

Equation (2) can now be evaluated using Eqs. (14) and (15) to give the MTF for the dynamic case:

$$\text{MTF} = \frac{\sin(\alpha/2) \sin(\nu\gamma/2) [\cos(\psi_H) - \cos(\psi_H + kd)]}{\alpha\nu\gamma/2 + \sin(\alpha/2) \sin(\nu\gamma/2) [\cos(\psi_H) + \cos(\psi_H + kd)]} \quad (16)$$

Note that, when $\nu = 0$, Eq. (16) degenerates to the static case of Eq. (11).

It has been shown that the spatial and temporal responses of imaging systems cannot be separated in all conditions.⁶ In particular, CCDs are systems where separation is not valid, because of their space-variant properties. If separation of the velocity effect were possible, the MTF for a moving image would be the product of the MTF calculated from that image held stationary and a function dependent only on velocity. Equation (16) above shows that this is not, in general, true for CCDs, because it is not possible to separate the velocity terms out of the denominator of Eq. (16).

Two special cases exist, however, where separation of a velocity function gives a good approximation of the true MTF value. The first occurs when $\nu\gamma/2$ is small, allowing the approximation $\sin(\nu\gamma/2) = \nu\gamma/2$ to be used on the second term of the denominator of Eq. (16). The second occurs when T_N/T_B is an integer, or $\psi_L - \psi_H = \pi$, eliminating the second term of the denominator, as in Eq. (12) above for the static case. In either case, the MTF can be expressed as

$$\text{MTF} = \frac{\sin(\nu\gamma/2)}{\nu\gamma/2} \text{MTF}_{\text{stat}} \quad (17)$$

where MTF_{stat} is the MTF evaluated without any velocity effects, as in Eq. (11) or (12).

III. Simulation Results

A fast Fourier transform (FFT) based simulation has been developed to evaluate the imaging abilities of CCDs. This simulation performs the charge-integration calculations numerically by a convolution operation. The FFT simulation program has the advantages of speed and the ability to calculate CCD output from more general input conditions and nonuniform pixel response. The FFT simulation has been used as

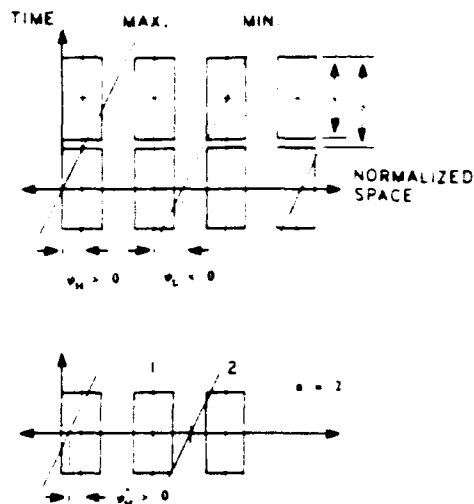


Fig. 4. Definition of parameters for the case of image velocity.

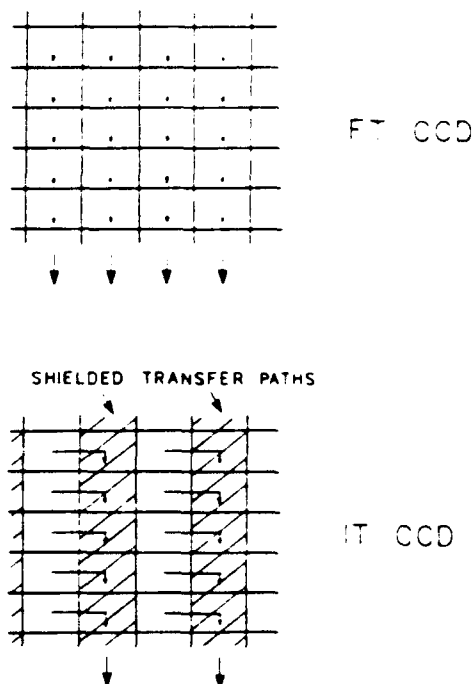


Fig. 5. Frame transfer (FT) and interline transfer (IT) CCD geometries and transfer paths.

a numeric check of the expressions developed in Sec. II. The results discussed below have been calculated by implementing the expressions developed in Sec. II on a personal computer spreadsheet program.

The results discussed below are intended to simulate two common CCD geometries, shown in Fig. 5. The frame transfer CCD (FT CCD) is designed with T_a and T_b equal or nearly equal for both dimensions. The interline transfer CCD (IT CCD) is designed with shielded charge transfer paths parallel to one axis of the device, with the result that T_a and T_b are equal or nearly equal for the dimension parallel to the charge transfer paths and that T_a and $T_b/2$ are equal or nearly equal for the dimension orthogonal to the charge trans-

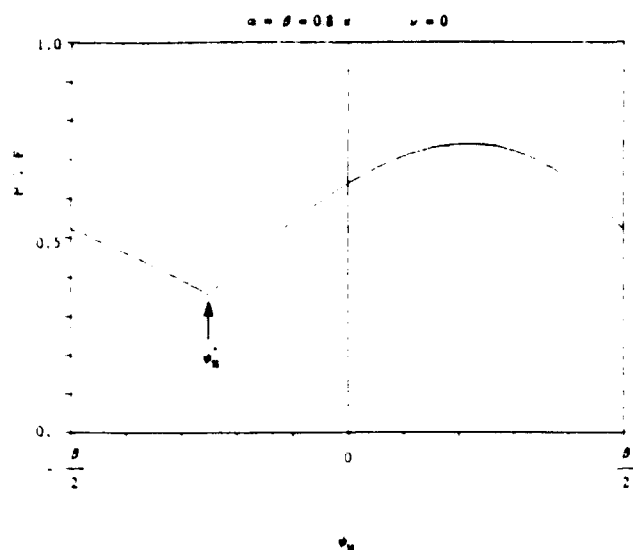


Fig. 6. MTF variation due to phase parameter with no image velocity.

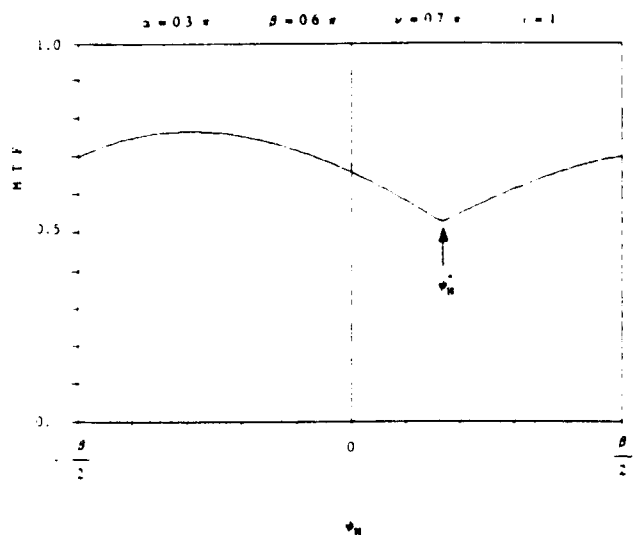


Fig. 7. MTF variation due to phase parameter with image velocity.

fer paths. The results below, therefore, evaluate the MTF for the two general cases of $T_\alpha = T_\beta$ and $T_\alpha = T_\beta/2$.

Figures 6 and 7 show typical MTF curves as a function of ψ_H . Figure 6 shows the case where $\alpha = \beta = 0.8\pi$ and $\nu = 0$, while Fig. 7 shows the case where $\alpha = 0.3\pi$, $\beta = 0.6\pi$, $\nu = 0.7$, and $\gamma = 1$. These results, and those following, are calculated by allowing ψ_H to vary from $-\beta/2$ to $\beta/2$ with a step size of $\beta/100$. Note that the minimum of each curve occurs when $\psi_H = \psi_H^*$, where the slope of the curve is discontinuous.

Figures 8 and 9 show the MTF as a function of spatial frequency for the cases $\alpha = \beta$ and $\alpha = \beta/2$, respectively, with no image velocity. Any MTF value between the two extreme curves on the graphs is possible, with the mean values represented by the central curves. Figure 8 is the static MTF calculated for either dimension of a FT CCD, or for the dimension of

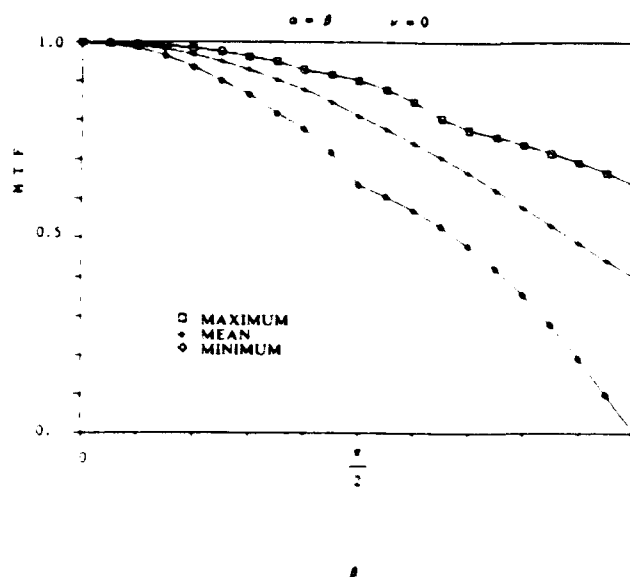


Fig. 8. Static MTF.

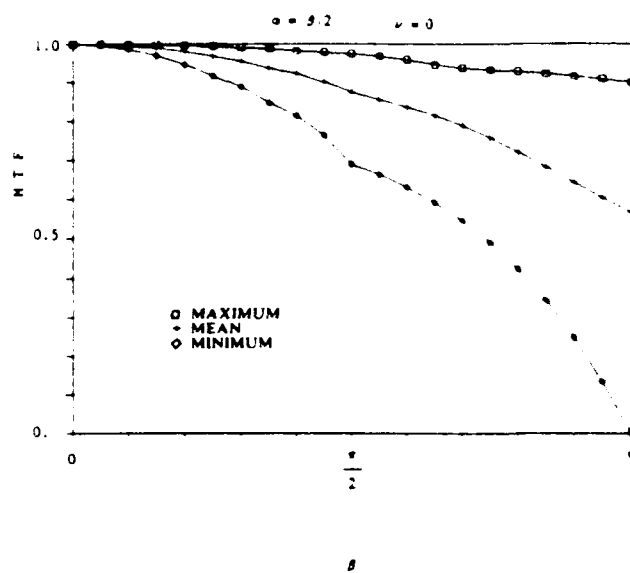


Fig. 9. Static MTF.

an IT CCD that is parallel to the charge transfer paths. Similarly, Fig. 9 is the static MTF calculated for the dimension of an IT CCD that is orthogonal to the charge transfer paths. The data points for the maximum MTF curve are obtained by searching the data generated at each spatial frequency. The data points for the minimum MTF curve are obtained by evaluating the MTF at ψ_H^* for each spatial frequency. The data points for the mean MTF curve are obtained by performing an arithmetic mean of the data generated at each spatial frequency. This mean calculation is justified because any offset ψ_H in the $-\beta/2$ to $\beta/2$ range is equally likely in actual use. The upper limit on the spatial frequency axis occurs when $\beta = \pi$, or $T_\beta = T_N$, corresponding to the Nyquist sampling limit of the CCD.

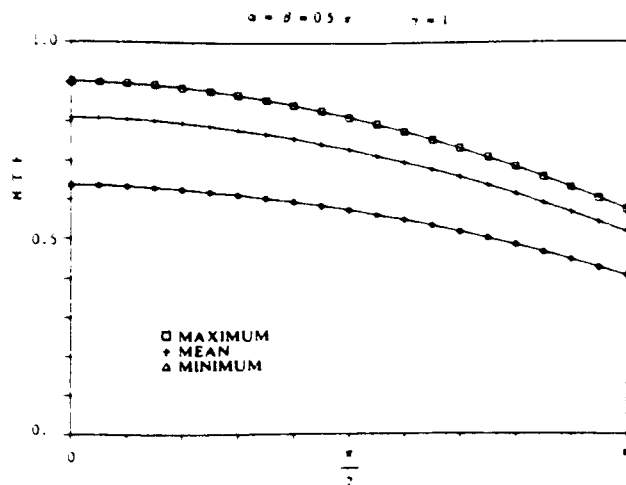


Fig. 10. Dynamic MTF.

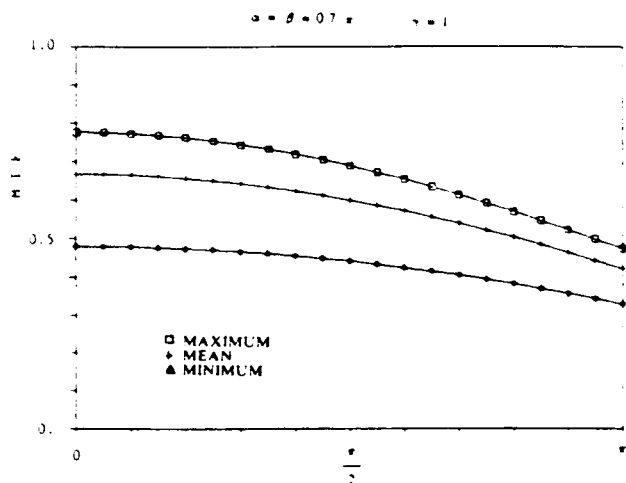


Fig. 11. Dynamic MTF.

Figures 10 and 11 show the MTF as a function of image velocity for the cases of $\alpha = \beta = 0.5\pi$ and $\alpha = \beta = 0.7\pi$, respectively. Figure 12 shows a comparison between the actual maximum MTF curve of Fig. 11 and the result of using the velocity approximation of Eq. (17). The numeric data for Fig. 12, along with percent error information, are presented in Table I. The error values support the conclusion reached earlier that velocity effects are not separable from the overall MTF expression. However, the approximation of Eq. (17) is applicable to the case shown in Fig. 10, because it satisfies the conditions discussed in Sec. II.

Figure 13 shows the mean MTF curve as a function of spatial frequency for several velocities, with $\alpha = \beta$ and $\gamma = 1$. It can be observed here that the mean MTF is degraded significantly for all spatial frequencies

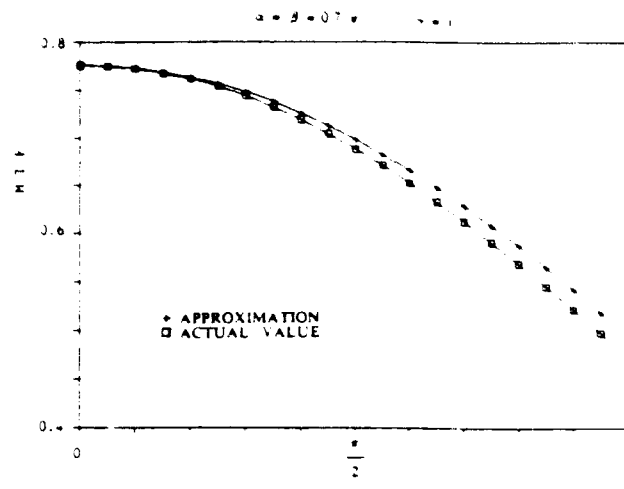


Fig. 12. Error introduced by separating the velocity effects from the dynamic MTF when not justified.

when ν is greater than $\sim 0.5\pi$. This can also be seen by observing the roll-off of the curves in Figs. 10-12.

An observation of the static MTF graphs, Figs. 8 and 9, reveals that wide variations in the MTF of CCDs occur due only to the alignment between the pixels and image.^{7,8} Any experimental procedure for measuring the performance of CCDs must recognize this wide variation. The three MTF curves, maximum, minimum, and mean, are the most important values for system designers, as they indicate the extremes and the expected value of the CCD response. Systems incorporating CCDs can better meet specifications when designers have this more complete information about device response.

Table I. Comparison of the Actual Dynamic MTF with the Dynamic MTF Calculated by Using the Velocity Separation Approximation.

$\alpha = \beta = 0.7\pi \quad \gamma = 1 \quad T_N = 1$			
ν/π	True MTF	Approximated MTF	Percent error (%)
0	0.7764	0.7764	0.00
0.05	0.7755	0.7756	0.02
0.10	0.7727	0.7732	0.07
0.15	0.7682	0.7693	0.14
0.20	0.7618	0.7637	0.25
0.25	0.7537	0.7566	0.39
0.30	0.7439	0.7480	0.56
0.35	0.7324	0.7379	0.75
0.40	0.7193	0.7263	0.97
0.45	0.7049	0.7134	1.21
0.50	0.6889	0.6990	1.47
0.55	0.6716	0.6834	1.75
0.60	0.6532	0.6665	2.03
0.65	0.6336	0.6484	2.34
0.70	0.6129	0.6292	2.65
0.75	0.5913	0.6089	2.97
0.80	0.5689	0.5876	3.29
0.85	0.5458	0.5654	3.61
0.90	0.5220	0.5424	3.92
0.95	0.4976	0.5187	4.24
1.00	0.4728	0.4943	4.55

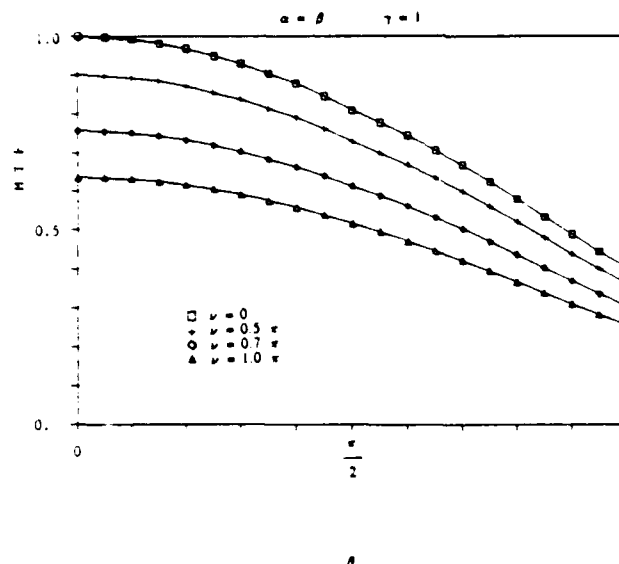


Fig. 13. Mean MTF for several image velocities.

The dynamic MTF graphs, Figs. 10, 11, and 13, display the effect of velocity on CCD performance. In all cases, the MTF is reduced significantly by image motion for all spatial frequencies. Figure 12 and Table I show conclusively that the velocity effect is not in general separable from the overall MTF calculation. However, for low velocities, the errors introduced by using the separation approximation of Eq. (17) are low. In addition, the other case for separability mentioned in Sec. II also holds, with no error introduced.

IV. Conclusion

This work has shown that the MTF of CCDs depends strongly on alignment between the image and the CCD pixels. A wide range of MTF values is possible for any given spatial frequency input. Designers should have complete information available about this variation to meet specifications of imaging systems incorporating CCDs.

In addition, this work has shown that the effect of image velocity significantly reduces the MTF of the static case for all spatial frequencies. This work has also shown that the velocity effect is not separable from the general MTF expression. However, approximating the true MTF with a separation of velocity terms is valid for only two special cases.

The authors would like to acknowledge the research support provided in part by the U.S. Army Research Office (for Night Vision & Electro-Optics Laboratory, Ft. Belvoir) contract DAA103-87-K-0121 and the Department of Electrical Engineering of the University of Dayton.

References

1. W. S. Boule and G. E. Smith, "Charge Coupled Semiconductor Devices," *Bell Syst. Tech. J.* **49**, 587-593 (1970).
2. J. W. Coltman, "The Specification of Imaging Properties by Response to a Sine Wave Input," *J. Opt. Soc. Am.* **44**, 468-471 (1954).
3. S. B. Campana, "Techniques for Evaluating Charge Coupled Imagers," *Opt. Eng.* **16**, 267-274 (1977).
4. A. Nordbryhn, "The Dynamic Sampling Effect with CCD Imagers," presented at SPIE Technical Symposium-East, Washington, DC (Mar. 1978).
5. A. A. S. Awwal, A. K. Cherri, M. A. Karim, and D. L. Moon, "Dynamic Response of an Electro-Optical Imaging System," *Proc. Soc. Photo-Opt. Instrum. Eng.* **1116**, 185-197 (1989).
6. L. Levi, "Spatiotemporal Transfer Function: Recent Developments," *Appl. Opt.* **22**, 4038-4041 (1983).
7. S. K. Park, R. Schowengerdt, and M. Kaczynski, "Modulation-Transfer-Function Analysis for Sampled Image Systems," *Appl. Opt.* **23**, 2572-2582 (1984).
8. W. Wittenstein, J. C. Fontanella, A. R. Newberry, and J. Baars, "The Definition of the OTF and the Measurement of Aliasing for Sampled Imaging Systems," *Opt. Acta* **29**, 42-50 (1982).

Restoration of dynamically degraded gray level images in phosphor based display devices

M. L. Gao

S. H. Zheng

M. A. Karim, MEMBER SPIE

D. L. Moon

University of Dayton

Electrical Engineering Department

300 College Park Avenue

Dayton, Ohio 45469-0226

Abstract. The concepts of dynamic modulation transfer function (DMTF) and degree of degradation (DD) are used for analyzing gray level image display of a phosphor based display system. Real-time restoration of the motion-degraded display images may be accomplished using one or more inverse filters whose characteristics depend on the magnitude and direction of the motion. Both DMTF and DD characteristics are used in the restoration of motion-degraded images.

Subject terms: electro-optical displays; dynamic modulation transfer function; motion-degraded displays; inverse filters; impulse response.

Optical Engineering 29(8), 878-882 (August 1990).

CONTENTS

1. Introduction
2. Review of dynamic modulation transfer function
3. Degree of degradation
4. Simulation of image degradation and restoration
5. Identification of the optimal restoration filter
6. Conclusions
7. Acknowledgment
8. References

1. INTRODUCTION

Traditionally, displays are evaluated using the modulation transfer function (MTF) in stationary mode.¹ However, the temporal response of an imaging system is expected to play an important role in the degradation of dynamic images. The absence of temporal response considerations in the formulation of the MTF limits its scope in analyzing degraded modulation contrast, especially at higher spatial frequencies.² This shortcoming of the MTF formulation has been overcome recently³ by the introduction of a newer measure, referred to as the dynamic MTF (DMTF). It also has been shown that the DMTF characteristics can be used for the restoration of motion-degraded display images in real time.

Another recent work⁴ has already identified several inverse filter⁵ based systems (both adaptive and nonadaptive) for the restoration of binary degraded images. However, most of the displayed images of interest are nonbinary in character. In this paper, we extend the work of Ref. 4 by exploring the capability of real-time restoration schemes in processing gray level images. For better quantitative analysis, a newer measure, referred to as the degree of degradation (DD), is introduced. Both DD and histograms are used to study gray level degraded images. Finally, an optimal set of inverse filters is identified for restoring motion-degraded display images.

2. REVIEW OF DMTF

By incorporating the sense of time and space, one may define a three-dimensional impulse response^{3,6} that behaves like an impulse function in both space and time. Using linear system

theory, therefore, the output image $g(x,y,t)$ is given in terms of the three-dimensional impulse response $h(x,y,t)$ by

$$g(x,y,t) = i(x,y,t) * h(x,y,t) \quad (1)$$

where $i(x,y,t)$ represents the input image and the asterisk denotes a convolution operation. However, for an object moving along the x - y plane with a constant velocity, the input image $i(x,y,t)$ can be characterized by $i(x+mt, y+nt)$, where m and n denote velocity components in the x and y directions, respectively. Accordingly, Eq. (1) can be rewritten as

$$g(x,y,t) = i(x+mt, y+nt) * h(x,y,t) \quad (2)$$

Now, by taking the Fourier transform of Eq. (2), one gets

$$G(u,v,f) = \iiint g(x,y,t) \exp[-j2\pi(ux + vy + ft)] dx dy dt \quad (3)$$

where u and v are the respective spatial frequency components along the horizontal and vertical directions and f is the temporal frequency.

Provided the point impulse response function $h(x,y,t)$ can be expressed as a product of a purely spatial function and purely temporal function, such as

$$h(x,y,t) = s(x,y)\Delta(t) \quad (4)$$

Eq. (3) can be evaluated³ to give

$$G(u,v,f) = D(f)S(u,v)I(u,v)\delta(f - um - vn) \quad (5)$$

where $D(f)$, $S(u,v)$, and $I(u,v)$ are the dynamic transfer function, the static transfer function, and the input spatial spectrum, respectively. The overall transfer function, dynamic MTF, is thus given by

$$H(u,v) = S(u,v)I(u,v) \quad (6)$$

where $D(u,v) = D(um + vn)$. Equation (6) dictates the effect of both velocity and static transfer function on the quality of the displayed image. Accordingly, it can be used to characterize the motion-degraded images as well.

It has already been determined that phosphor persistence af-

Invited Paper EO-107 received Nov. 10, 1989; revised manuscript received Jan. 29, 1990; accepted for publication May 22, 1990.
© 1990 Society of Photo-Optical Instrumentation Engineers

fects the temporal response of a CRT display.^{7,8} When the objects are moving very fast, the phosphor characteristics of the display screen cause the displayed images to appear blurred. In particular, image tube phosphor characteristics have been shown to be exponential in nature, given by⁹

$$\Delta(t) = \frac{1}{\tau} \exp\left(-\frac{t}{\tau}\right), \quad (7)$$

where τ is the time constant defined as the duration in which the phosphorescence decays to $1/e$ of its maximum value. Taking the Fourier transform of Eq. (7), the dynamic component of the DMTF of the phosphor screen can be obtained:

$$D(f) = \frac{1}{1 + j2\pi f\tau}. \quad (8)$$

By definition, therefore, the inverse filter is given by

$$[D(f)]^{-1} = 1 + 2\pi f\tau. \quad (9)$$

However, to estimate $[D(f)]^{-1}$, one needs to estimate the time constant of the phosphors used in the electro-optical display under consideration. One may make use of the fact that type P-1052 phosphor, for instance, takes 20 ms to decay to 10% of its maximum value. This implies that the corresponding time constant is 8.68 ms (Ref. 4). In this work, for simplicity, we approximate it by 0.008 s.

3. DEGREE OF DEGRADATION

Using the concept of mean-square deviation, the degree of degradation of an $N \times M$ image can be defined as

$$DD = \left[\sum_{i=1}^N \sum_{j=1}^M \frac{1}{NM} (D_{ij} - O_{ij})^2 \right]^{1/2}, \quad (10)$$

where D_{ij} is a parameter of the degraded image measured at location $\{i, j\}$, while O_{ij} is an identical quantity of the original image measured at the same location. For example, D_{ij} and O_{ij} both can be gray levels at location $\{i, j\}$ of the degraded and original image, respectively. The DD measure can be used to quantify the extent of image degradation.

For simplicity, we may measure the intensity function $f(x, y)$ of the original image and intensity function $g(x, y)$ of the corresponding degraded image. The corresponding DD may be referred to as the zeroth-order DD, denoted by DD_0 . Likewise, we may also measure the first derivative $f'(x, y)$ of the original image and the first derivative $g'(x, y)$ of the degraded image. Accordingly, $f'(x, y)$ and $g'(x, y)$ can be used to evaluate the first-order DD, denoted by DD_1 . While DD_0 indicates the degree of degradation of gray levels between the degraded and original images, DD_1 indicates the degree of degradation of the gray-gradient between the degraded and original images.

4. SIMULATION OF IMAGE DEGRADATION AND RESTORATION

In this work, we use inverse filters to restore the motion-degraded images. The actual optical implementation of an inverse filter would involve employing either a hologram or a spatial light modulator (SLM) in a system like that shown in Fig. 1.

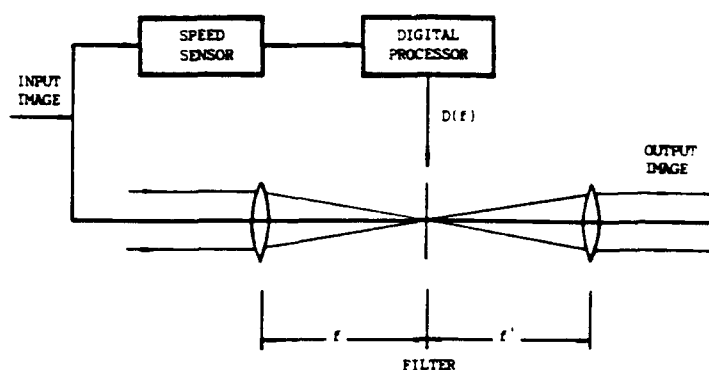


Fig. 1. Real-time image restoration system.



Fig. 2. 64x64 pixel, 16 gray level input.

The simulation algorithm for obtaining the degraded images involves the following three steps: (1) Obtain the fast Fourier transform (FFT) of the static image. (2) Obtain the FFT of $\Delta(t)$. (3) Take the inverse FFT of the product (point by point) of the FFTs obtained in steps (1) and (2).

The restored image can be obtained from the degraded image in accordance with the following four steps: (1) Obtain the FFT of the degraded image $g(x, y)$. This provides $S(u, v)D(f)$. (2) Given the velocity of the object and its direction, an inverse filter, i.e., $[D(f)]^{-1}$, is calculated. (3) The results obtained in steps (1) and (2) are multiplied (point by point) in the frequency domain. (4) Take the inverse FFT of the result of step (3).

Since the modulus of the temporal function $[D(f)]^{-1}$ is non-zero, it is possible to have a perfect recovery of the input image using inverse filters. In an adaptive restoration system, the actual speed V_o needs to be estimated first and then the corresponding inverse filter needs to be placed at the Fourier plane of the optical system. However, the estimation of the value and direction of motion may not be a trivial problem. Alternatively, therefore, we devise a nonadaptive scheme whereby a preprocessed inverse filter (corresponding to velocity $V_f = V_o$) may already be placed at the Fourier plane. In that case, both the digital processor and the sensor can be avoided from the system shown in Fig. 1. Depending on the value of $|V_f - V_o|$, therefore, this filter may partially restore motion-degraded displayed images.

A 64x64 pixel undistorted image (having 16 gray levels), as shown in Fig. 2, is used as the input for the simulation. Figure 3 shows the degraded images when the displayed input images move at an angle of 45° relative to the x-axis with velocities of 2 cm/s and 10 cm/s, respectively. One can see that both the horizontal and vertical edges of the image are significantly de-

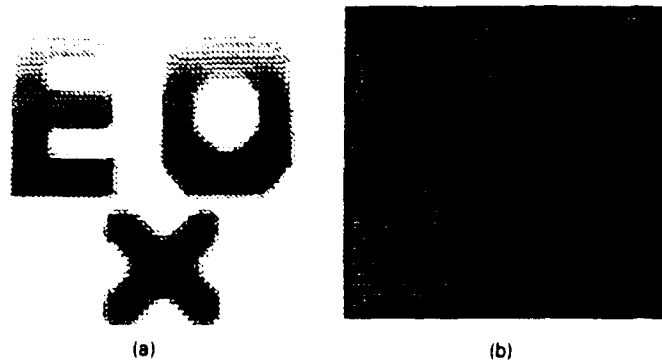


Fig. 3. Degraded images caused by object motions: (a) 2 cm/s and (b) 10 cm/s.

graded. Figure 4 shows the images restored from that of Fig. 3(b) using inverse filters corresponding to velocities of 8 cm/s and 12 cm/s, respectively.

Typical curves showing the variation of DD_0 and DD_1 with object velocity V_o are shown in Fig. 5, where the inverse filter used was particularly designed to handle a velocity value of V_f . From Fig. 5, we see that both DD_0 and DD_1 increase with increasing V_o . This implies that with increasing object motion, the displayed image will be degraded more and more. The use of a restoration filter, however, reduces the value of both DD_0 and DD_1 . With V_f approaching V_o , the value of both DD_0 and DD_1 approaches zero. In the limiting case, the motion degradation of an image can be totally eliminated. With increasing $|V_f - V_o|$, both DD_0 and DD_1 increase. The smaller the difference between V_o and V_f , the smaller the degeneration of the displayed image. It may be noted, however, that the distributions of both DD_0 and DD_1 are not necessarily symmetric about the point of the minimum value.

To extract additional information about the image, one can make use of a histogram. For example, Fig. 6(a) shows the histogram of the original image, while Figs. 6(b) through 6(d) show degraded images when the displayed original moves with a velocity of 6, 12, and 16 cm/s. It can be concluded that the average gray level value decreases with increasing object velocity. As per Eq. (5), f is proportional to a linear combination of m and n . This implies that $D(f)$ decreases with increasing m and n [per Eq. (8)], which in turn indicates that the average gray level value of the restored image decreases with increasing V_o .

From the histograms of Fig. 7, however, one may conclude that with increasing V_f (when V_o is fixed), the average gray level value of the restored image increases. Figure 8 shows the histograms of the restored image (using a filter corresponding to $V_f = 10$ cm/s) obtained from image degraded by object motion. One may conclude from Fig. 8 that with increasing V_o (for a fixed value of V_f), the average gray level value of the restored image decreases.

5. IDENTIFICATION OF THE OPTIMAL RESTORATION FILTER

It is first necessary to determine the extent of the object velocity for the application under consideration. Here, for illustration, we chose an image intensifier tube, such as that used in night-vision goggles. For such applications, it can be estimated⁴ that the maximum spatial speed m can be 16 cm/s. Note that this speed refers to the speed at which the image appears to move

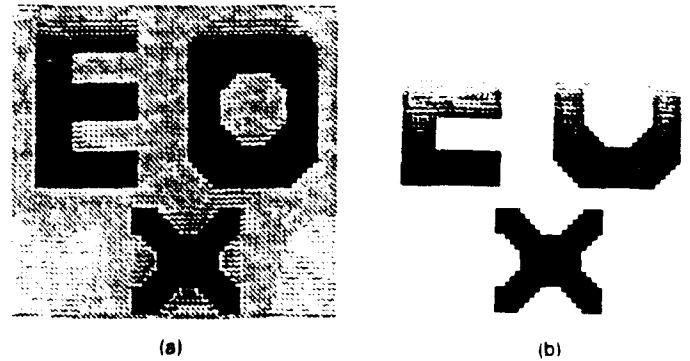


Fig. 4. Restored images of the input of Fig. 3(b) using inverse filter: corresponding to (a) 8 cm/s and (b) 12 cm/s.

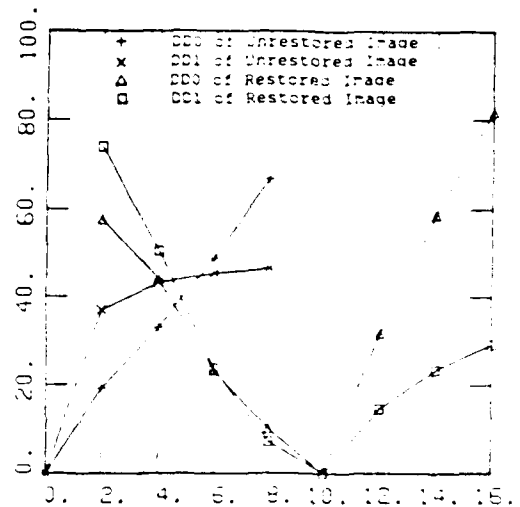


Fig. 5. DD_0 and DD_1 characteristics with and without a restoration filter (corresponding to $V_f = 10$ cm/s).

on the surface of the display. The actual speed of the target, depending on its location, may be far greater.

An inverse filter based on a not-so-accurate estimation of velocity can be used to reasonably restore the motion-degraded images. Accordingly, it may be possible to identify only one or a set of a few optimum inverse filters for the restoration of displayed images of objects. The degree of degradation can be used for identifying the optimum inverse filter.

The algorithm for identifying the optimum inverse filter consists of the following steps: (1) Determine the maximum allowable value of DD_0 . (2) Obtain a family of DD_0 - V_o curves. (3) From the family of curves, select the set(s) of DD_0 - V_o curves that can account for the total extent of V_o and, at the same time, satisfy the constraint of the maximum allowable DD_0 . (4) Comparing the sets of curves obtained in step (3), choose the one that involves the least number of filters and the lowest value of DD_0 .

For example, Fig. 9 shows DD_0 characteristics for two of the restoration filters corresponding to $V_f = 6$ cm/s and 14 cm/s. Provided that 30 (in arbitrary units) has been determined as the maximum tolerable value of DD_0 , these two filters may be used to form a composite inverse filter for real-time restoration of the corresponding motion-degraded displayed images. Alternatively, the user could switch between these filters until the displayed image appears acceptable.

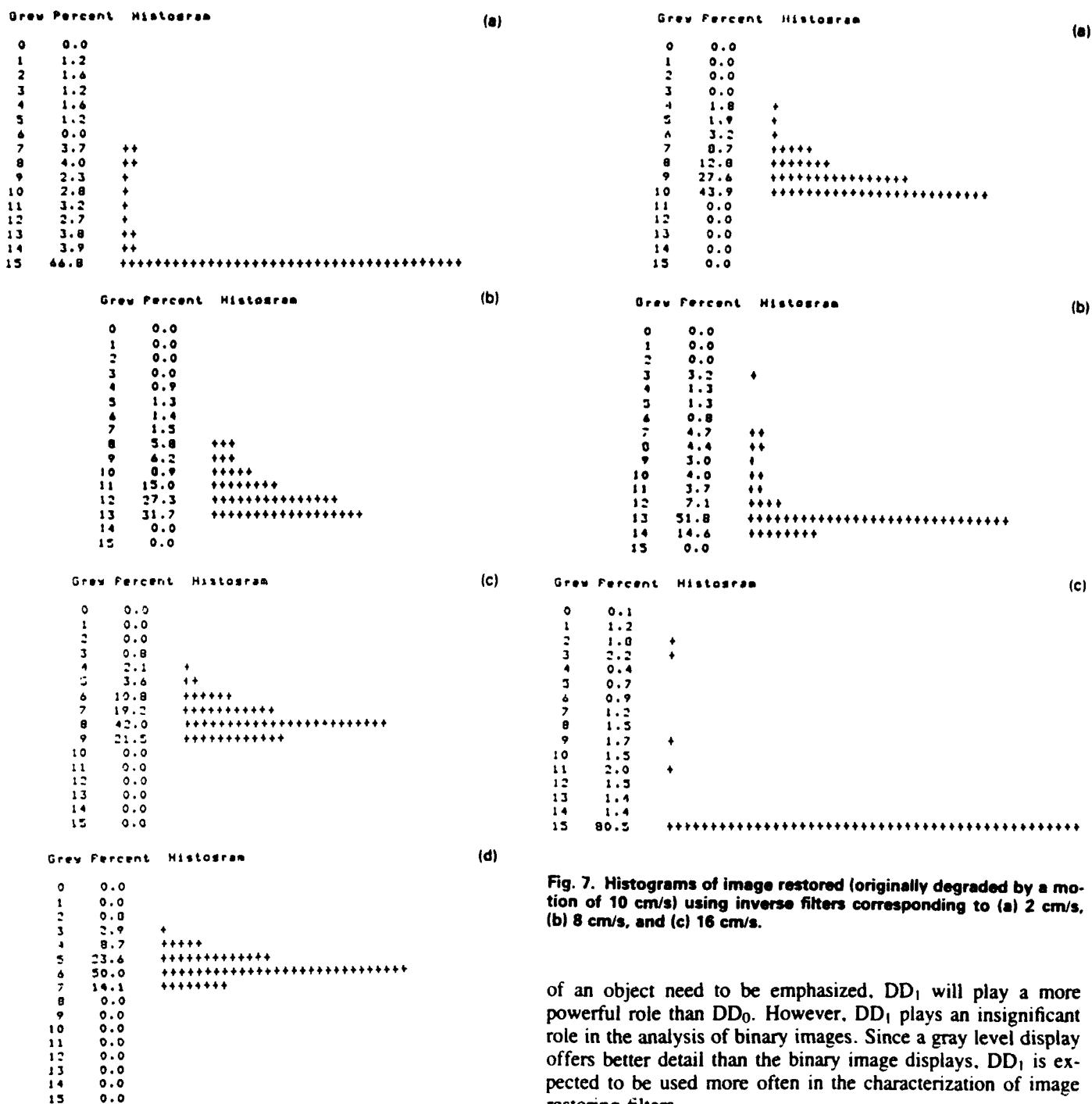


Fig. 6. Histograms of (a) the original image and degraded images caused by a motion of (b) 6 cm/s, (c) 12 cm/s, and (d) 16 cm/s.

It should be noted that DD_1 indicates the extent of degradation in the distribution of the gray gradient. Thus, depending on the application, one can use DD_1 also as a criterion (instead of DD_0) for the determination of the optimum inverse filter. In fact, by taking both DD_0 and DD_1 into consideration, a more optimal inverse filter can be identified.

For example, Fig. 10 shows two motion-degraded images of the object of Fig. 2 with respective DD_1 values of 4.07 and 7.19. Obviously, the latter display has a more degenerated distribution of gray levels. When the high frequency components

Fig. 7. Histograms of image restored (originally degraded by a motion of 10 cm/s) using inverse filters corresponding to (a) 2 cm/s, (b) 8 cm/s, and (c) 16 cm/s.

of an object need to be emphasized, DD_1 will play a more powerful role than DD_0 . However, DD_1 plays an insignificant role in the analysis of binary images. Since a gray level display offers better detail than the binary image displays, DD_1 is expected to be used more often in the characterization of image restoring filters.

6. CONCLUSIONS

The DMTF is a powerful tool for the analysis of a dynamic optical imaging system. The separable type of DMTF, considered herein, is of the simplest form. In general, an imaging system may have a significantly more complex form of the DMTF. The DMTF also serves as a tool in the synthesis of optical systems. The design of systems that can be used for restoring the motion-degraded displayed images, using both the DMTF and the degree of degradation, is just an example of such a system synthesis. In this paper, we have developed a scheme for identifying an optimum set of inverse filters for implementing a real-time image restoration system.

Grew Percent Histogram

0	0.4	
1	2.6	+
2	1.9	+
3	1.1	
4	1.1	
5	1.1	
6	1.7	+
7	1.7	
8	2.3	+
9	2.2	+
10	1.9	+
11	1.6	
12	1.8	+
13	1.8	+
14	1.5	
15	75.5	+++++

Grew Percent Histogram

0	0.0	
1	0.0	
2	0.7	
3	3.1	+
4	1.3	
5	1.2	
6	0.6	
7	5.7	+++
8	3.7	++
9	3.3	+
10	3.7	++
11	3.7	++
12	6.5	+++
13	46.5	+++++
14	0.0	
15	0.0	

Grew Percent Histogram

0	0.0	
1	0.0	
2	0.7	
3	3.6	++
4	1.6	
5	2.5	+
6	7.4	+++
7	4.9	++
8	6.2	+++
9	26.5	+++++
10	46.6	+++++
11	0.0	
12	0.0	
13	0.0	
14	0.0	
15	0.0	

Fig. 8. Histograms of images restored using an inverse filter (corresponding to 10 cm/s) from images degraded by motion of (a) 6 cm/s, (b) 12 cm/s, and (c) 16 cm/s.

7. ACKNOWLEDGMENT

The authors would like to acknowledge the research support provided in part by U.S. Army Research Office contract DAAL03-87-K-0121 with the University of Dayton.

8. REFERENCES

1. E. L. O'Neill, *Introduction to Statistical Optics*, Addison-Wesley, Reading, Mass. (1963).
2. J. L. Horner, *Optical Signal Processing*, Academic, New York (1987).
3. A. A. S. Awwal, A. K. Cheri, M. A. Karim, and D. L. Moon, "Dynamic response of an electro-optical imaging system," in *Helmet-Mounted Displays*, Proc. SPIE 1116, 185 (1989).
4. A. K. Cheri, A. A. S. Awwal, M. A. Karim, and D. L. Moon, "Restoration of motion-degraded images in electro-optical displays," in *Helmet-Mounted Displays*, Proc. SPIE 1116, 198 (1989).
5. F. T. S. Yu, *Optical Information Processing*, Wiley, New York (1983).
6. L. Levi, "On combined spatial and temporal characteristics of optical systems," *Opt. Acta* 17, 869 (1970).
7. J. D. Gaskill, *Linear Systems, Fourier Transforms, and Optics*, Wiley, New York (1978).
8. M. V. Klein and T. E. Furtak, *Optics*, Second Edition, Wiley, New York (1986).
9. B. R. Sandel, D. F. Collins, and A. L. Broadfoot, "Effect of phosphor persistence on photometry with image intensifiers and integrating readout device," *Appl. Opt.* 25, 3697 (1986).

(a)

(b)

(c)

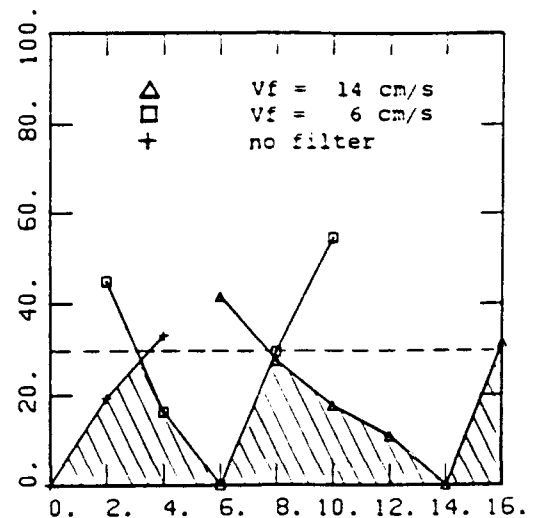


Fig. 9. DD_0 characteristics versus degradation motion for a restoration filter corresponding to 0 cm/s, 6 cm/s, and 14 cm/s.



Fig. 10. Restored images having DD_0 values of (a) 4.07 and (b) 7.19.

Ming L. Gao and Song H. Zheng: Biographies and photographs appear with the paper "Device nonspecific minimum resolvable temperature difference for infrared imaging systems characterization" in this issue.

Mohammad A. Karim: Biography and photograph appear with the special issue guest editorial in this issue.



Donald L. Moon is a professor in and chairman of the Electrical Engineering Department and director of the Center for Electro-Optics at the University of Dayton. Moon received his BSEE degree from the West Virginia Institute of Technology in 1963, an MSEE degree from the University of Toledo in 1966, and the Ph.D. degree in electrical engineering from Ohio State University in 1974. Prior to joining the University of Dayton, he served as acting chief scientist of the U.S. Air Force Avionics Laboratory at Wright Patterson AFB, as an associate professor of electrical engineering at the University of North Carolina at Charlotte, and as a senior design engineer of NCR Corporation. He served as the president for the 1989 National Aerospace and Electronics Conference (NAECON). He is a senior member of the IEEE.

Development of the modulation transfer function and contrast transfer function for discrete systems, particularly charge-coupled devices

John C. Feltz

Systems Research and Applications
Corporation
2000 15th Street North
Arlington, Virginia 22201

Abstract. The modulation transfer function (MTF) and contrast transfer function (CTF) are considered for discrete systems. The MTF and CTF are derived for the charge-coupled device (CCD). The analysis presented considers the full effects of sampling on device response. Experimental tests of the CTF for a line-array CCD are presented. The MTF and CTF are shown to be multivalued functions for discrete systems.

Subject terms: electro-optical displays; modulation transfer function; contrast transfer function; charge-coupled devices; sampling.

Optical Engineering 29(8), 893-904 (August 1990).

CONTENTS

1. Introduction
2. Charge-coupled devices
3. Modulation transfer function (MTF) and contrast transfer function (CTF) derivation
 - 3.1. MTF derivation
 - 3.2. CTF derivation
 - 3.3. Discussion of theoretical results
4. CTF measurements
5. Discussion
6. Conclusion
7. Acknowledgments
8. References

1. INTRODUCTION

The charge-coupled device (CCD) is a very versatile imaging device.¹ CCDs have a number of advantages over other imaging devices and in recent years have been incorporated in a wide range of electro-optic systems.² It is important, therefore, to acquire a detailed understanding of the characteristics and limitations of CCDs as imaging devices, particularly their spatial frequency response.

Characterization methods for continuous optical devices, such as the modulation transfer function (MTF) and contrast transfer function (CTF), have proved to be very useful techniques. It is desirable to have compatible methods for analyzing discrete devices such as CCDs. Previous attempts to apply the MTF and CTF to discrete devices have had mixed success.³ The MTF and CTF assume a linear, space-invariant and time-invariant system. While CCDs are linear within an operating range, they are not space invariant because they have fixed sampling locations. Characterization methods for discrete devices must consistently apply sampling theory, which previously has not been done.

The MTF and CTF are commonly used to analyze the spatial frequency response of optical devices because they can be cascaded in a system: the total MTF or CTF of a system is equal to the product of the MTFs or CTFs, respectively, of the system components. This work concentrates on applying the MTF and CTF to CCD behavior so that overall behavior of systems incorporating CCDs can be analyzed consistently.

Although the MTF is simpler to calculate in theory than the CTF, experimental work is almost always done with the CTF. CTF analysis can be implemented with simpler equipment, and CTF results for continuous systems can be mathematically manipulated to acquire the appropriate MTF values.⁴

This work presents the sampling analysis necessary for a more complete understanding of the behavior of discrete optical devices in general and CCDs in particular, as well as experimental work to verify this behavior. The MTF and CTF will be used to analyze the spatial frequency response of ideal CCDs. The theoretical response of the CCD for the two functions will be derived, and the experimental CTF will be measured. The resultant information will allow more accurate design of systems incorporating discrete devices such as CCDs.

The discussion centers on mathematically describing the behavior of CCDs in detail, particularly the effects of sampling. The MTF and CTF input images will be applied to a mathematical model of ideal linear CCD pixels to predict the MTF and CTF results. The experimental discussion describes the results of illuminating a line-array CCD with the CTF input image at several frequencies.

2. CCDs

The CCD was developed by Boyle and Smith in 1970.¹ CCDs can be used in purely electronic applications such as shift registers but are most commonly used for imaging. This work is concerned exclusively with CCDs as imaging devices.

CCDs are typically fabricated with metal-oxide semiconductor silicon technology on a p-type substrate with an n-type

Invited Paper EO-109 received Nov. 15, 1989; revised manuscript received March 2, 1990; accepted for publication May 22, 1990.
© 1990 Society of Photo-Optical Instrumentation Engineers.

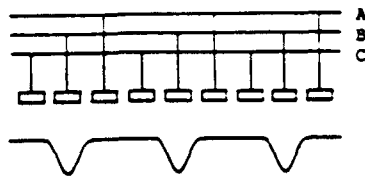


Fig. 1. CCD potential wells formed by a high voltage on line B.

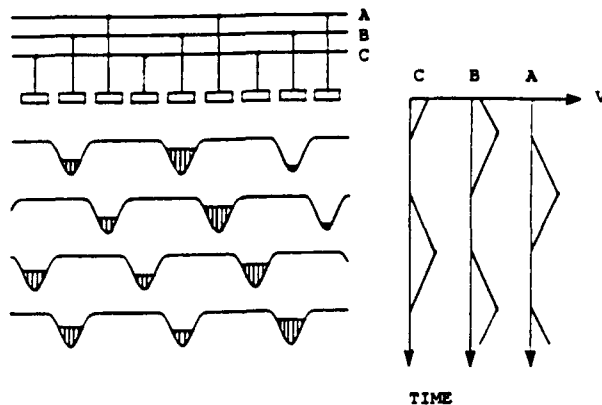


Fig. 2. Charge transfer process.

active layer. Each pixel is connected to several address lines, which create potential wells in the CCD substrate. Figure 1 illustrates this: line B has a higher voltage than lines A and C, forming one potential well in the center of each pixel. Photoelectrons are collected in the potential wells, with the electron content of a well equal to the time and space integral of the incident radiation as modified by the quantum efficiency of the CCD material.⁵

A clocking scheme controls the photoelectron collection. During the charge integration interval, electrons are collected and stored in the potential wells. During the charge transfer interval, the electron packets are transferred to the CCD output. By attaching the address lines to different phases of a high-frequency clock, the potential wells and their charge packets are quickly moved across the CCD, as shown in Fig. 2.

This work examines two of the more common geometries used in CCDs, the frame transfer CCD (FT CCD) and the interline transfer CCD (IT CCD). The significant difference between the two geometries for this discussion is the relationship between pixel width and pixel pitch. Pixel width is the size of the active portion of the pixel capable of creating and collecting photoelectrons in a potential well. Pixel pitch, or pixel spacing, is the distance between the centers of adjacent pixels. FT CCD pixels have approximately equal pixel width and pixel pitch along both array axes. IT CCD pixels have approximately equal pixel width and pixel pitch along one axis and have a pixel width approximately equal to one-half the pixel pitch along the other axis.

A number of CCD noise conditions and nonlinearities have been analyzed previously,² such as incomplete charge transfer, blooming, smearing, thermal noise, and deep-IR electrons. Manufacturers of CCDs have developed a number of fabrication and packaging methods to reduce the effects of these phenomena, and they are not discussed further in this work.

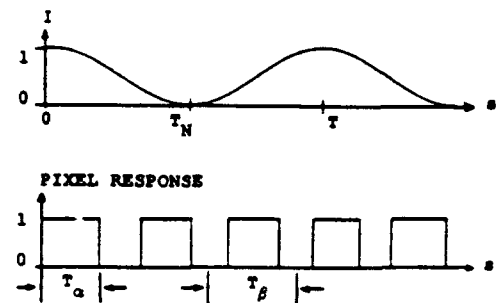


Fig. 3. Line-array static MTF parameters.

3. MTF AND CTF DERIVATION

This section develops the mathematics for the MTF and CTF of discrete systems and discusses the results. CCD pixels are assumed to be ideal, with identical uniform response in time and space and a regular rectangular geometry. In addition, the noise conditions referred to in the previous section are ignored.

3.1. MTF derivation

The MTF is first calculated for the one-dimensional static case i.e., a line-array CCD and a stationary input image. The calculation is then modified to handle image motion with a constant velocity within one scan interval and is further modified to handle oblique images on an area-array CCD. The reader is referred to an earlier work⁶ for a more detailed explanation of the parameters used in the calculations below.

The MTF input function is⁴

$$I = \frac{1}{2}[1 + \cos(s)] \quad (1)$$

Equation (1) gives the CCD photoelectron creation rate. The MTF is defined by the response of the CCD⁴ as

$$\text{MTF} = \frac{B_{\max} - B_{\min}}{B_{\max} + B_{\min}} \quad (2)$$

where B_{\max} and B_{\min} are the values, in any appropriate units, of a neighboring maximum and minimum of the output. For CCDs, B_{\max} and B_{\min} will be the output of two specific pixels, usually in volts.

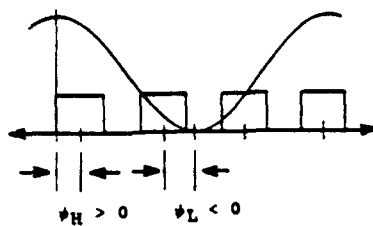
Figure 3 illustrates the following parameters (all of which are measured in millimeters): T —period of the input pattern, T_N —Nyquist period of the input, T_α —CCD pixel active width, and T_β —CCD pixel pitch.

The pixel width and pixel spacing are normalized as

$$\alpha = \frac{\pi T_\alpha}{T_N} \quad (3)$$

$$\beta = \frac{\pi T_\beta}{T_N} \quad (4)$$

The alignment between the CCD pixels and the input pattern is important in calculating the MTF.³ Figure 4 illustrates the following alignment parameters (both of which are measured in radians): ψ_H —offset between a maximum of the input pattern and the center of the nearest pixel, and ψ_L —offset between a minimum of the input pattern and the center of the nearest pixel. These parameters are limited by


 Fig. 4. MTF alignment parameters ψ_H and ψ_L .

$$\frac{-\beta}{2} \leq \psi_H \leq \frac{\beta}{2} \quad (5)$$

$$\frac{-\beta}{2} \leq \psi_L \leq \frac{\beta}{2} \quad (6)$$

If a pixel generates B_{\max} , i.e., is a local maximum, there are in general two pixels that could generate B_{\min} . The critical offset ψ_H^* is defined to be the value of ψ_H such that the minimum of the input pattern lies at the boundary of two pixels. The pixel index n is given by

$$n = \text{Int}\left(\frac{T_N}{T_\beta}\right) + 1 \quad (7)$$

where $\text{Int}(x)$ returns the integer part of x so that

$$\psi_H^* = \pi - (n - 1/2)\beta \quad (8)$$

Using n and ψ_H^* , ψ_L becomes

$$\psi_L = \psi_H + k\beta \quad (9)$$

where

$$k = \begin{cases} n, & \psi_H \leq \psi_H^* \\ n-1, & \psi_H > \psi_H^* \end{cases} \quad (10)$$

Using Eq. (1), B_{\max} and B_{\min} are

$$B_{\max} = \int_{s=\psi_H-(\alpha/2)}^{\psi_H+(\alpha/2)} \frac{1}{2}[1 + \cos(s)]ds \quad (11)$$

$$B_{\min} = \int_{s=\psi_L-(\alpha/2)}^{\psi_L+(\alpha/2)} \frac{1}{2}[1 + \cos(s)]ds \quad (12)$$

Evaluating and substituting into Eq. (2), the MTF is

$$\text{MTF} = \frac{\sin\left(\frac{\alpha}{2}\right) \left[\cos(\psi_H) - \cos(\psi_H + k\beta) \right]}{\alpha + \sin\left(\frac{\alpha}{2}\right) \left[\cos(\psi_H) + \cos(\psi_H + k\beta) \right]} \quad (13)$$

Equation (13) simplifies if $k\beta = \pi$, so $\psi_L - \psi_H = \pi$ from Eq. (9). The MTF of Eq. (13) reduces to

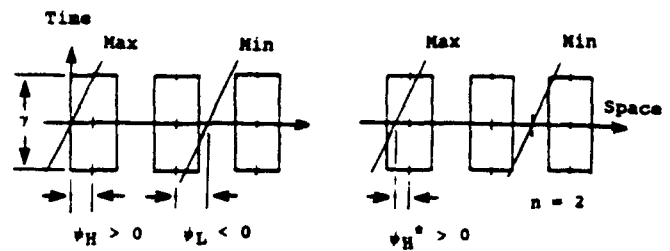


Fig. 5. Offset parameters for the dynamic MTF.

$$\text{MTF} = \frac{2 \sin\left(\frac{\alpha}{2}\right) \cos(\psi_H)}{\alpha} \quad (14)$$

This simplification occurs only when T_N/T_β is an integer.

To incorporate linear motion in the MTF,⁷ the following additional terms are defined:

V —image velocity (millimeters/second), γ —CCD charge integration interval (seconds), and δ —CCD scan interval (seconds). The normalized velocity ν (radians/second) is defined as

$$\nu = \pi \frac{V}{T_N} \quad (15)$$

The input image, Eq. (1), is now

$$I = 1/2[1 + \cos(s - \nu t)] \quad (16)$$

Figure 5 illustrates the new alignment parameters.

Using Eq. (16), the MTF for the dynamic line-array device becomes

$$\text{MTF} = \frac{\sin\left(\frac{\alpha}{2}\right) \sin\left(\frac{\nu\gamma}{2}\right) [\cos(\psi_H) + \cos(\psi_H + k\beta)]}{\frac{\alpha\nu\gamma}{2} + \sin\left(\frac{\alpha}{2}\right) \sin\left(\frac{\nu\gamma}{2}\right) [\cos(\psi_H) + \cos(\psi_H + k\beta)]} \quad (17)$$

When $\nu = 0$, Eq. (17) degenerates to the static expression of Eq. (13).

The spatial and temporal responses of imaging systems cannot be separated under all conditions.⁸ Separation is not valid for discrete devices because of their space/time variance. Equation (17) verifies this since it is not possible to separate out the velocity terms.

Two special cases exist, however, in which separation of a velocity function gives a good approximation to the true MTF value. The first case occurs when $\nu\gamma/2$ is small, and the second occurs when T_N/T_β is an integer. If MTF_{stat} is the MTF evaluated without any velocity effects, as in Eq. (13) or Eq. (14), the MTF for either special case can be given by

$$\text{MTF} = \frac{\sin(\nu\gamma/2)}{\nu\gamma/2} \text{MTF}_{\text{stat}} \quad (18)$$

An area-array CCD with an oblique image is illustrated in Fig. 6. The input image is oriented at an angle θ_p ; with no motion it is given as

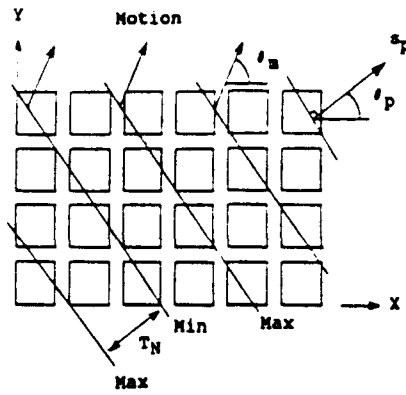


Fig. 6. Area-array MTF parameters.

$$I = 1/2[1 + \cos(s_p)] \quad (19)$$

where s_p is a generalized spatial parameter, oriented at an angle θ_p to the CCD x axis. To evaluate the MTF along either of the two pixel axes, s_p is resolved into two components, s_x and s_y , as

$$s_p = s_x \cos(\theta_p) + s_y \sin(\theta_p) \quad (20)$$

For the case of image motion, the image moves with a velocity V at an angle θ_m . V is normalized as

$$v = \frac{V}{T_N} \quad (21)$$

It is necessary to find the projection of the velocity along the image itself. Accordingly, the projected velocity v_p is defined as

$$v_p = v \cos(\theta_m - \theta_p) \quad (22)$$

The physical dimensions of the CCD are normalized in a manner similar to that of the line-array case:

$$\alpha_x = \cos(\theta_p) \pi \frac{T_{ax}}{T_N} \quad (23)$$

$$\beta_x = \cos(\theta_p) \pi \frac{T_{bx}}{T_N} \quad (24)$$

$$\alpha_y = \sin(\theta_p) \pi \frac{T_{ay}}{T_N} \quad (25)$$

$$\beta_y = \sin(\theta_p) \pi \frac{T_{by}}{T_N} \quad (26)$$

For any rectangular device, the MTF can be calculated in either of two orthogonal directions, corresponding to the x and y pixel axes. MTF_x is the MTF calculated by progressing in the x direction from a maximum to an adjacent minimum; MTF_y is calculated by progressing in the y direction. The MTF derivations are similar.

To determine MTF_x , the alignment variables ψ_H , ψ_L , ψ_H^* , n , and k are defined at the center of the pixel with respect to the y dimension and the time dimension, i.e., at $s_y = 0$ and $t = 0$. For MTF_y , the alignment variables are defined at the center of the pixel with respect to the x dimension and the time dimension. The pixel index n and critical offset ψ_H^* for the MTF_x calculation are

$$n = \text{Int} \left[\frac{T_N}{T_{bx} \cos(\theta_p)} \right] \quad (27)$$

$$\psi_H^* = \pi - (n - 1/2)\beta_x \quad (28)$$

and for the MTF_y calculation are

$$n = \text{Int} \left[\frac{T_N}{T_{by} \sin(\theta_p)} \right] \quad (29)$$

$$\psi_H^* = \pi - (n - 1/2)\beta_y \quad (30)$$

B_{\max} and B_{\min} are triple integrals. When evaluated and substituted into Eq. (2), MTF_x is

$$MTF_x = \frac{\sin\left(\frac{\alpha_x}{2}\right) \sin\left(\frac{\alpha_y}{2}\right) \sin\left(\frac{v\gamma}{2}\right) \left[\cos(\psi_H) - \cos(\psi_H + k\beta_x) \right]}{\frac{\alpha_x \alpha_y v\gamma}{2} + \sin\left(\frac{\alpha_x}{2}\right) \sin\left(\frac{\alpha_y}{2}\right) \sin\left(\frac{v\gamma}{2}\right) \left[\cos(\psi_H) + \cos(\psi_H + k\beta_x) \right]} \quad (31)$$

MTF_y is calculated similarly:

$$MTF_y = \frac{\sin\left(\frac{\alpha_x}{2}\right) \sin\left(\frac{\alpha_y}{2}\right) \sin\left(\frac{v\gamma}{2}\right) \left[\cos(\psi_H) - \cos(\psi_H + k\beta_y) \right]}{\frac{\alpha_x \alpha_y v\gamma}{2} + \sin\left(\frac{\alpha_x}{2}\right) \sin\left(\frac{\alpha_y}{2}\right) \sin\left(\frac{v\gamma}{2}\right) \left[\cos(\psi_H) + \cos(\psi_H + k\beta_y) \right]} \quad (32)$$

Equations (31) and (32), the expressions for the MTF along either axis of a two-dimensional array of pixels, are the most general form of the work in this section. Equations (31) and (32) degenerate to all simpler forms of the MTF discussed earlier.

3.2. CTF derivation

The CTF is more difficult to calculate analytically than is the MTF because it involves integrals exclusively of square waves. The limits of integration are determined by the positions of the image edges and pixel edges, and they completely determine the integration results. For this reason, the results below are not so much an equation for the CTF as they are an algorithm for applying several equations to the CTF calculation.

The derivation below is for the case of a line-array CCD with image motion. Derivation of CTF results for an area-array CCD proved to be too lengthy for the scope of this work but will be a logical extension of the methods presented here.

The input image for the CTF is a raised square wave. The CTF is calculated as

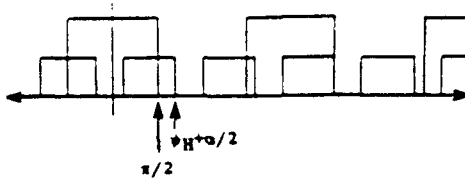


Fig. 7. Static CTF calculations.

$$CTF = \frac{B_{\max} - B_{\min}}{B_{\max} + B_{\min}} \quad (33)$$

where B_{\max} and B_{\min} are the values, in any appropriate units, of a neighboring maximum and minimum of the output. For CCDs, B_{\max} and B_{\min} will be the output of two specific pixels, usually in volts.

The parameter definitions for the CTF are the same as those for the MTF. The normalized variables are

$$\alpha = \frac{\pi T_a}{T_N} \quad (34)$$

$$\beta = \frac{\pi T_B}{T_N} \quad (35)$$

The offset parameters ψ_H , ψ_L , ψ_H^* , n , and k apply to the CTF as they do for the MTF.

Figure 7 shows the simplest case, which occurs when there is no image motion. B_{\max} and B_{\min} can be calculated from the arrangement of pixel edges and image edges as

$$B_{\max} = \text{Min} \left[\psi_H + \frac{\alpha}{2}, \frac{\pi}{2} \right] - \text{Max} \left[\psi_H - \frac{\alpha}{2}, -\frac{\pi}{2} \right] \quad (36)$$

$$B_{\min} = \alpha - \text{Min} \left[\psi_L + \frac{\alpha}{2}, \frac{3}{2}\pi \right] + \text{Max} \left[\psi_L - \frac{\alpha}{2}, \frac{\pi}{2} \right] \quad (37)$$

where $\text{Max}[x, y]$ returns the greater of x and y and $\text{Min}[x, y]$ returns the lesser of x and y . Equation (33) can be evaluated with Eqs. (36) and (37) to determine the CTF for the static case.

B_{\max} and B_{\min} become much more complicated if the image has velocity. Figure 8 shows the possible pixel conditions for finding B_{\max} , where the image velocity is restricted to a positive sign for convenience. The expression for B_{\max} in this case is

$$B_{\max} = \alpha\gamma - (UL_{\max}) - (LR_{\max}) \quad (38)$$

where UL_{\max} and LR_{\max} are the cross-hatched corner portions of a pixel, identified in Fig. 8 as the upper left and lower right. These portions are not covered by the input image maximum. It is cautioned that "upper left" and "lower right" are not indications of spatial arrangement: upper and lower refer to the time dimension, and left and right refer to space. The terms upper left and lower right are used only for convenience in visualizing the problem and in referring to Fig. 8. The expression for B_{\min} is similar to that for B_{\max} :

$$B_{\min} = (UL_{\min}) + (LR_{\min}) \quad (39)$$

where UL_{\min} and LR_{\min} are the cross-hatched corner portions not covered by the input image minimum.

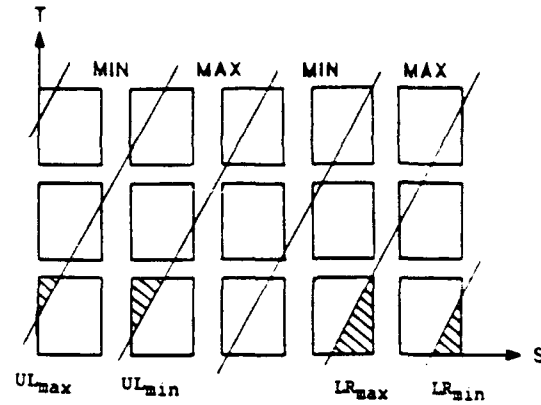


Fig. 8. Dynamic CTF calculations.

UL_{\max} , LR_{\max} , UL_{\min} , and LR_{\min} can each have one of three possible forms: 0—complete coverage of the pixel corner by appropriate part of the input image, $B(H/2)$ —triangle with base B and height H not covered by the appropriate part of the input image, and $(B_1 + B_2)(H/2)$ —trapezoid with bases B_1 and B_2 and height H not covered by the appropriate part of the input image. Finding the corner contributions UL_{\max} , LR_{\max} , UL_{\min} , and LR_{\min} is now the chief problem. The calculation of UL_{\max} will be representative of the others and will be examined in the most detail.

The charge integration interval ends when $t = \gamma/2$. At this time, the low-to-high transition or left edge of the square wave occurs at $s = -\pi/2 + v\gamma/2$, and the left edge of the pixel lies at $s = \psi_H - \alpha/2$. The variable u is defined to be their difference:

$$u = \left(\frac{-\pi}{2} + \frac{v\gamma}{2} \right) - \left(\psi_H - \frac{\alpha}{2} \right) \quad (40)$$

If u is less than or equal to 0, the upper left portion of the pixel is completely covered by the input image, and so UL_{\max} is zero. If u is greater than 0, another criterion must be found to distinguish between the two remaining forms for UL_{\max} , the triangle and the trapezoid. Dividing u by v gives the time interval before the end of the charge integration interval, i.e., the displacement down from the top left corner of the pixel in Fig. 8, when the left edge of the input pattern crosses the left edge of the pixel. If this interval is less than the charge integration interval γ , then UL_{\max} is evaluated using the triangle formulation. Otherwise, the trapezoid is used.

The expression for UL_{\max} for the triangle form is

$$UL_{\max} = \frac{BH}{2} = \frac{(u)(u/v)}{2} = \frac{u^2}{2v} \quad (41)$$

To find the expression for UL_{\max} for the trapezoid form, let w be defined as

$$w = \left(\frac{-\pi}{2} - \frac{v\gamma}{2} \right) - \left(\psi_H - \frac{\alpha}{2} \right) \quad (42)$$

which is similar to the expression for u . The two bases of the trapezoid are now equal to u and w . The expression for UL_{\max} for trapezoid form is thus

$$UL_{\max} = (B_1 + B_2)\frac{H}{2} = (u + w)\frac{\gamma}{2} \quad (43)$$

The algorithm for determining UL_{\max} can be stated succinctly as follows:

UL_{max}:

$$u = \left(\frac{-\pi}{2} + \frac{\nu\gamma}{2} \right) - \left(\psi_H - \frac{\alpha}{2} \right) \quad (44)$$

IF ($u \leq 0$) THEN

$$UL_{\max} = 0$$

ELSE IF ($u/v \leq \gamma$) THEN

$$UL_{\max} = \frac{u^2}{2v} \quad (45)$$

ELSE

$$w = \left(\frac{-\pi}{2} - \frac{\nu\gamma}{2} \right) - \left(\psi_H - \frac{\alpha}{2} \right) \quad (46)$$

$$UL_{\max} = (u + w) \frac{\gamma}{2} \quad (47)$$

END

Similar algorithms for LR_{\max} , UL_{\min} , and LR_{\min} are as follows:

LR_{max}:

$$u = \left(\psi_H + \frac{\alpha}{2} \right) - \left(\frac{\pi}{2} - \frac{\nu\gamma}{2} \right) \quad (48)$$

IF ($u \leq 0$) THEN

$$LR_{\max} = 0$$

ELSE IF ($u/v \leq \gamma$) THEN

$$LR_{\max} = \frac{u^2}{2v} \quad (49)$$

ELSE

$$w = \left(\psi_H + \frac{\alpha}{2} \right) - \left(\frac{\pi}{2} + \frac{\nu\gamma}{2} \right) \quad (50)$$

$$LR_{\max} = (u + w) \frac{\gamma}{2} \quad (51)$$

END

UL_{min}:

$$u = \left(\frac{\pi}{2} + \frac{\nu\gamma}{2} \right) - \left(\psi_H + k\beta - \frac{\alpha}{2} \right) \quad (52)$$

IF ($u \leq 0$) THEN

$$UL_{\min} = 0$$

ELSE IF ($u/v \leq \gamma$) THEN

$$UL_{\min} = \frac{u^2}{2v} \quad (53)$$

ELSE

$$w = \left(\frac{\pi}{2} - \frac{\nu\gamma}{2} \right) - \left(\psi_H + k\beta - \frac{\alpha}{2} \right) \quad (54)$$

$$UL_{\min} = (u + w) \frac{\gamma}{2} \quad (55)$$

END

LR_{min}:

$$u = \left(\psi_H + k\beta + \frac{\alpha}{2} \right) - \left(\frac{3\pi}{2} - \frac{\nu\gamma}{2} \right) \quad (56)$$

IF ($u \leq 0$) THEN

$$LR_{\min} = 0$$

ELSE IF ($u/v \leq \gamma$) THEN

$$LR_{\min} = \frac{u^2}{2v} \quad (57)$$

ELSE

$$w = \left(\psi_H + k\beta + \frac{\alpha}{2} \right) - \left(\frac{3\pi}{2} + \frac{\nu\gamma}{2} \right) \quad (58)$$

$$LR_{\min} = (u + w) \frac{\gamma}{2} \quad (59)$$

END

These algorithms give the necessary information for calculating the dynamic CTF by using Eqs. (33), (38), and (39).

3.3. Discussion of theoretical results

Figures 9 and 10 show typical MTF curves as a function of ψ_H . Figure 9 shows the MTF of a line-array device with $T_\alpha = T_\beta = 0.7T_N$ and no image motion, while Fig. 10 shows MTF_x for an area-array device with $2T_{\alpha x} = T_{\beta x} = 0.8T_N$, $T_{\alpha y} = T_{\beta y} = 0.6T_N$, $\theta_p = 45^\circ$, and $\nu_p\gamma = 0.5\pi$. These results are calculated by allowing ψ_H to vary from $-\beta/2$ to $\beta/2$ with a step size of $\beta/100$. Note that the minimum of each curve occurs where $\psi_H = \psi_H^*$, where the slope of the curve is discontinuous.

Figures 11 and 12 show the MTF of a line-array device as a function of spatial frequency for the cases $T_\alpha = T_\beta$ and $2T_\alpha = T_\beta$, respectively, with no image velocity. Any MTF value between the two extreme curves on the graphs is possible, with the mean values represented by the central curves. The data points for the maximum curve are obtained by searching the MTF values generated at each spatial frequency. The data points for the minimum MTF curve are obtained by evaluating the MTF at $\psi_H = \psi_H^*$ for each spatial frequency. The data points for the mean MTF curve are obtained by performing an arithmetic mean of the data generated at each spatial frequency. This mean calculation is

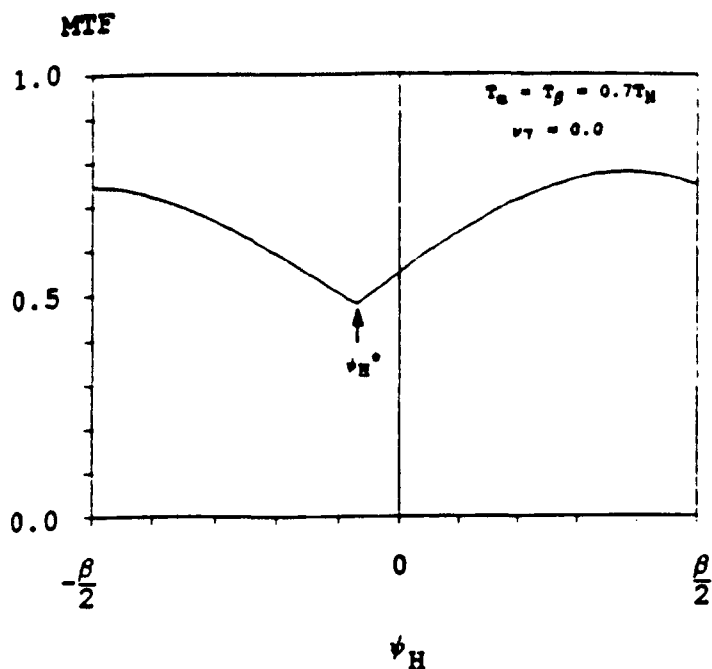


Fig. 9. Variation in MTF due to offset ψ_H for the static line-array case.

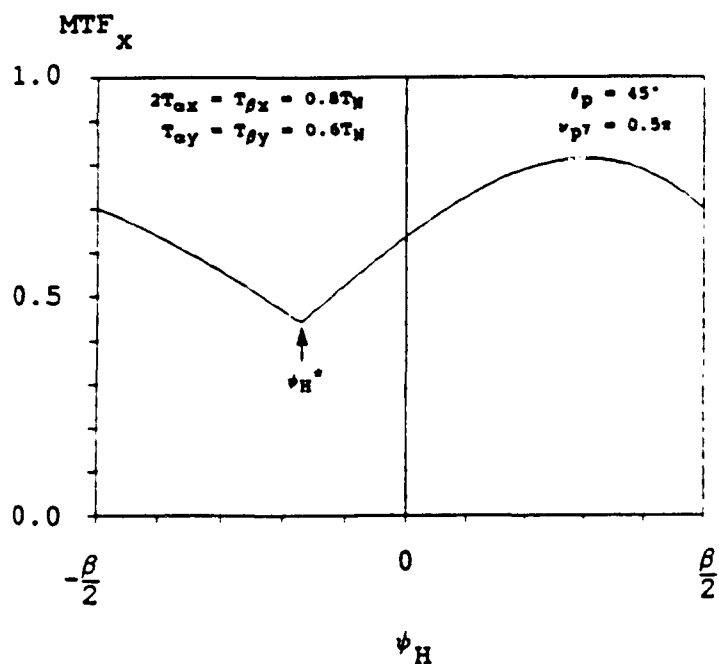


Fig. 10. Variation in MTF due to offset ψ_H for the dynamic area-array case.

justified because any offset ψ_H in the range $-\beta/2$ to $\beta/2$ is equally likely for an input image in actual use. The upper limit on normalized spatial frequency is π , which corresponds to the Nyquist sampling limit of the CCD.

Figures 11 and 12 are important results because they are the ideal static MTF responses for the two geometries discussed in Sec. 2. Figure 11 shows the static MTF calculated for either dimension of an FT CCD or for the dimension parallel to the charge transfer paths of an IT CCD. Figure 12 shows the static

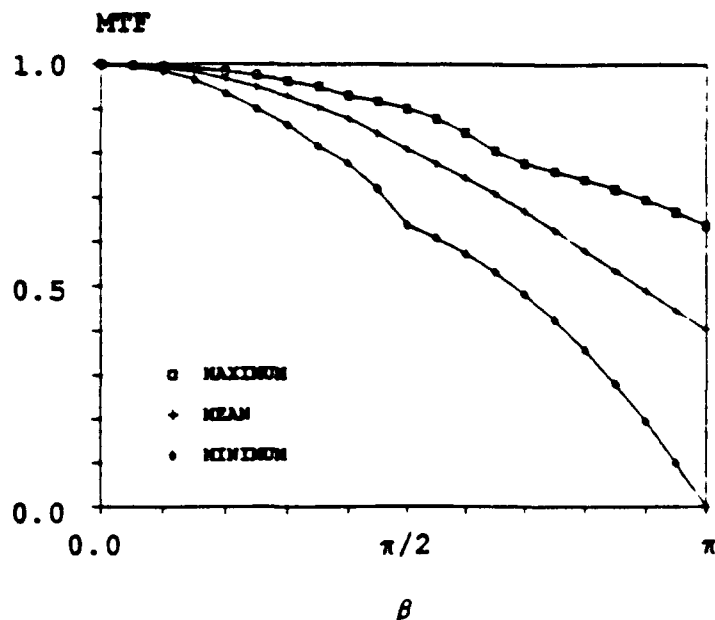


Fig. 11. Static line-array MTF, $T_\alpha = T_\beta$.

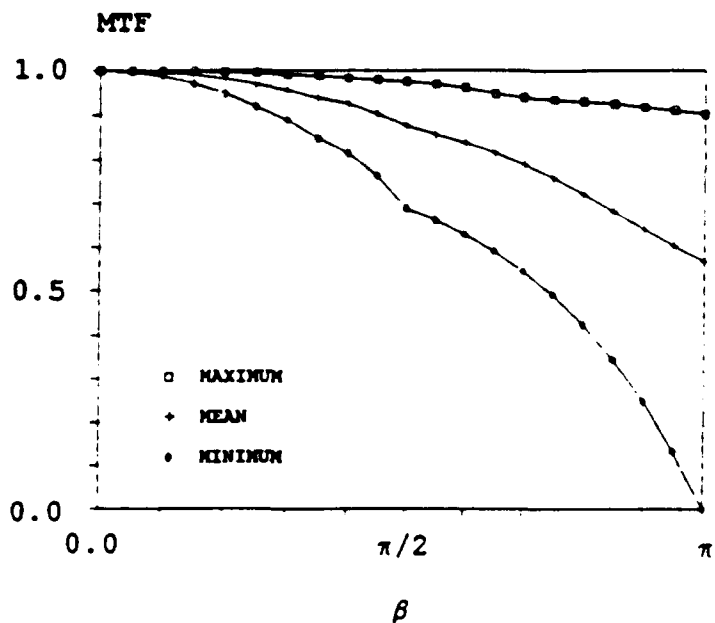


Fig. 12. Static line-array MTF, $2T_\alpha = T_\beta$.

MTF calculated for the dimension orthogonal to the charge transfer paths of an IT CCD.

Figure 13 shows the mean MTF of a line-array device as a function of frequency for $T_\alpha = T_\beta$ for several velocities. Notice that even at low frequencies, the MTF is seriously degraded by a moving image. Figure 14 shows the MTF of a line-array device as a function of velocity for $T_\alpha = T_\beta = 0.7T_N$. The curves in this figure show a roll-off near a velocity of $\nu\gamma = \pi/2$. This can also be seen in the spacing between the curves of Fig. 13.

Figure 15 shows a comparison between the actual maximum MTF curve of Fig. 14 and the result of using the velocity separation approximation given by Eq. (18). The numeric data for

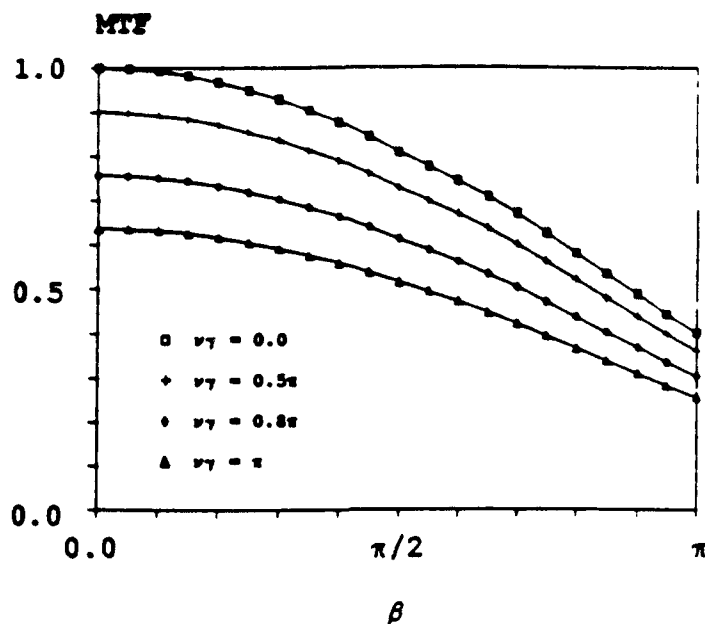
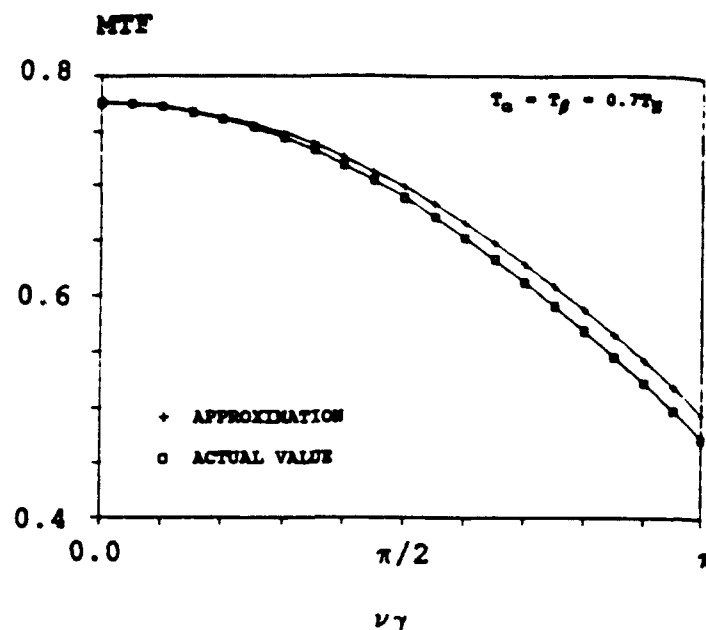
Fig. 13. Dynamic line-array MTF, $T_\alpha = T_\beta$.

Fig. 15. MTF velocity separation.

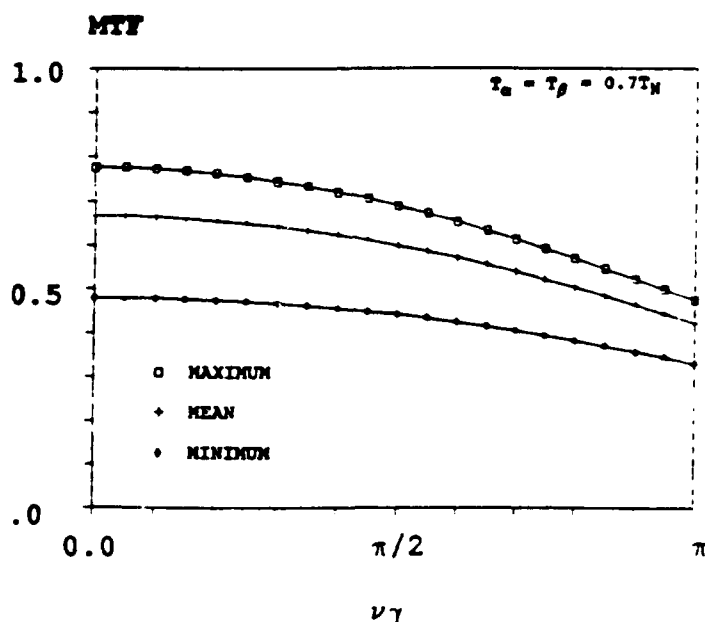
Fig. 14. Dynamic line-array MTF, $T_\alpha = T_\beta = 0.7T_N$.

TABLE I. MTF velocity separation data.

$\nu\gamma/\pi$	Actual MTF	Approximated MTF	Percent Error
0	0.7764	0.7764	0.00
0.05	0.7755	0.7756	0.02
0.10	0.7727	0.7732	0.07
0.15	0.7682	0.7693	0.14
0.20	0.7618	0.7637	0.25
0.25	0.7537	0.7566	0.39
0.30	0.7439	0.7480	0.56
0.35	0.7324	0.7379	0.75
0.40	0.7193	0.7263	0.97
0.45	0.7049	0.7134	1.21
0.50	0.6889	0.6990	1.47
0.55	0.6716	0.6834	1.75
0.60	0.6532	0.6665	2.03
0.65	0.6336	0.6484	2.34
0.70	0.6129	0.6292	2.65
0.75	0.5913	0.6089	2.97
0.80	0.5689	0.5876	3.29
0.85	0.5458	0.5654	3.61
0.90	0.5220	0.5424	3.92
0.95	0.4976	0.5187	4.24
1.00	0.4728	0.4943	4.55

Fig. 15, along with percent error information, are presented in Table I. The error values support the conclusion reached earlier that velocity effects are not separable from the overall dynamic MTF expression.

Figure 16 shows the mean MTF of an FT CCD as a function of θ_p for several input frequencies, with no image velocity and $T_{\beta x} = T_{\beta y}$. A graph of MTF_y for the conditions of Fig. 16 would be identical to that shown but would be flipped horizontally to have the maxima at $\theta_p = 90^\circ$. Figure 17 shows the effects of image velocity on the MTF_x for an area-array CCD.

Figures 18 and 19 show typical CTF curves as a function of ψ_H . The shape of the curves is quite different from the corresponding MTF graphs in Figs. 9 and 10. Figures 20 and 21

show the static CTF as a function of spatial frequency for $T_\alpha = T_\beta$ and $2T_\alpha = T_\beta$, respectively. Notice that the CTF is always 1 for frequencies below half the Nyquist frequency. Notice also that the maximum CTF is 1 for all frequencies out to the Nyquist limit.

Figure 22 displays the mean CTF as a function of frequency for several velocities, with $T_\alpha = T_\beta$. Notice that a moving image causes the CTF to degrade below a value of 1 at frequencies lower than half the Nyquist frequency, which does not occur on the static graphs, Figs. 20 and 21. Figure 23 shows the CTF as a function of velocity for $T_\alpha = T_\beta = 0.5T_N$. This graph suggests that velocity separation is not possible for the CTF calculations, because the three curves have dissimilar shapes.

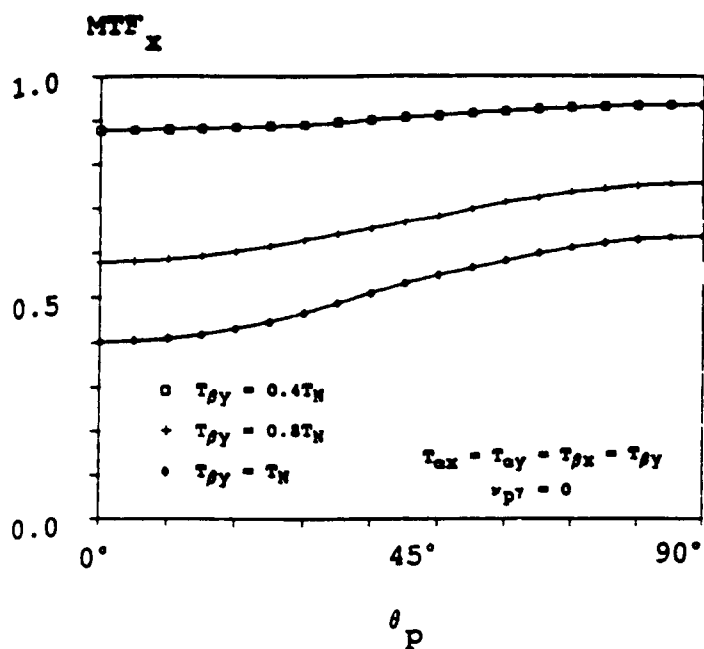


Fig. 16. Static area-array FT CCD MTF_x vs θ_p .

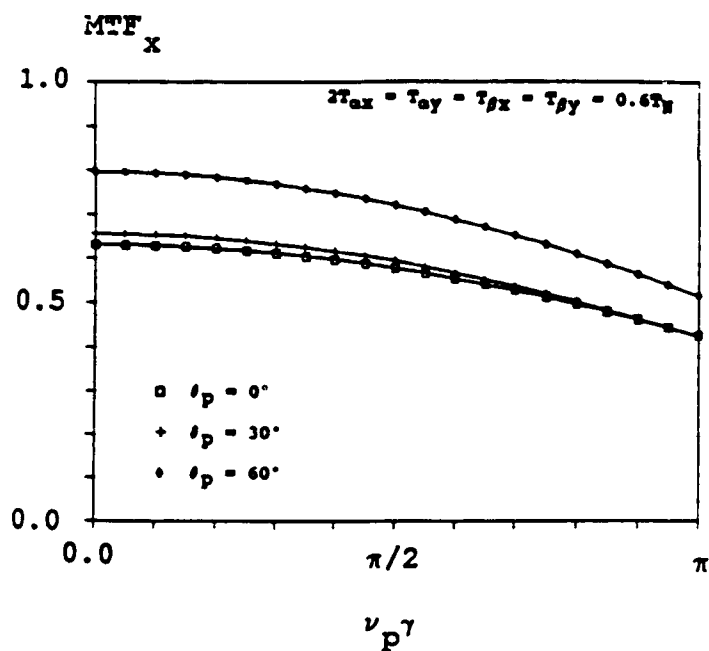


Fig. 17. Dynamic area-array MTF_y vs $\nu_p \gamma$.

Figures 9 through 12 demonstrate conclusively that application of the MTF to discrete devices gives a multivalued result over a wide range. This wide variation in the calculated MTF depends only on the alignment between the image and the device pixels. Similar results for the CTF are shown in Figs. 18 through 21. Any experimental procedure for measuring the performance of CCDs or other discrete devices must recognize these variations. The MTF and CTF curves shown in Figs. 11, 12, 20, and 21 are the most important results for system designers, since they indicate the extremes and the expected value of the CCD

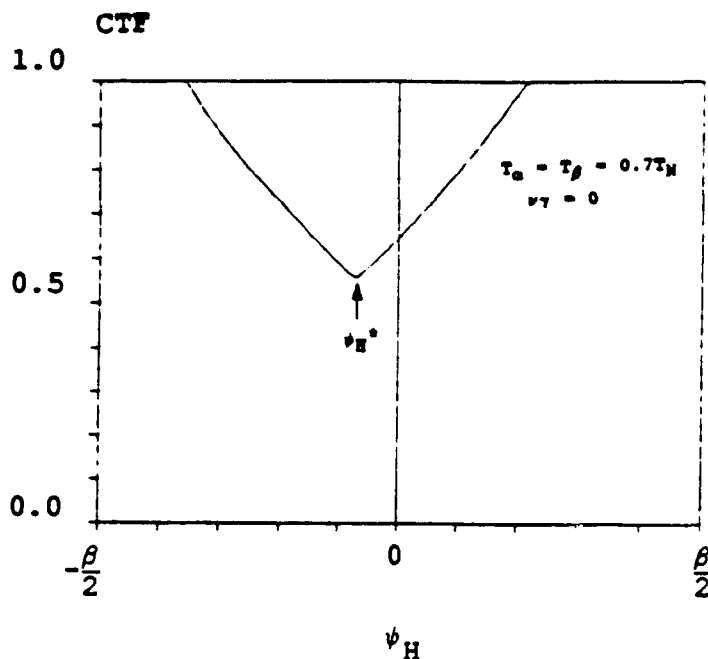


Fig. 18. Variation in CTF due to offset ψ_H for the static line-array case.

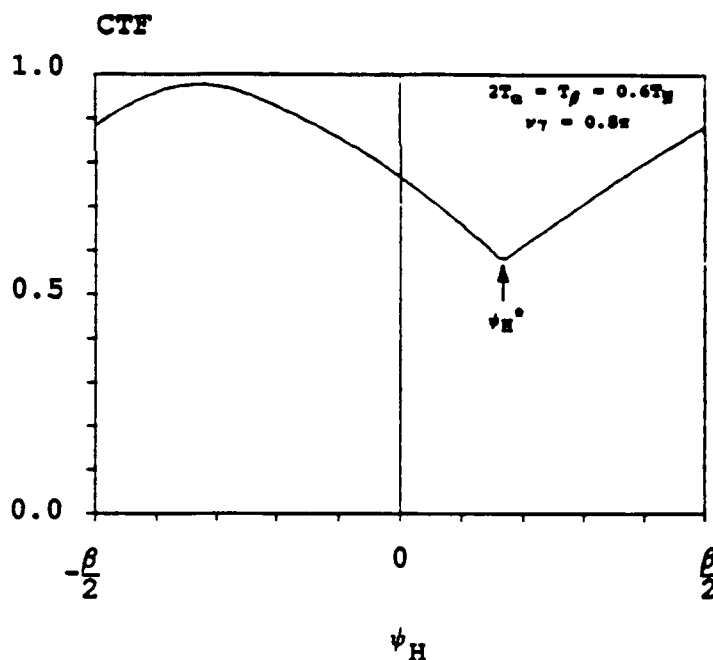
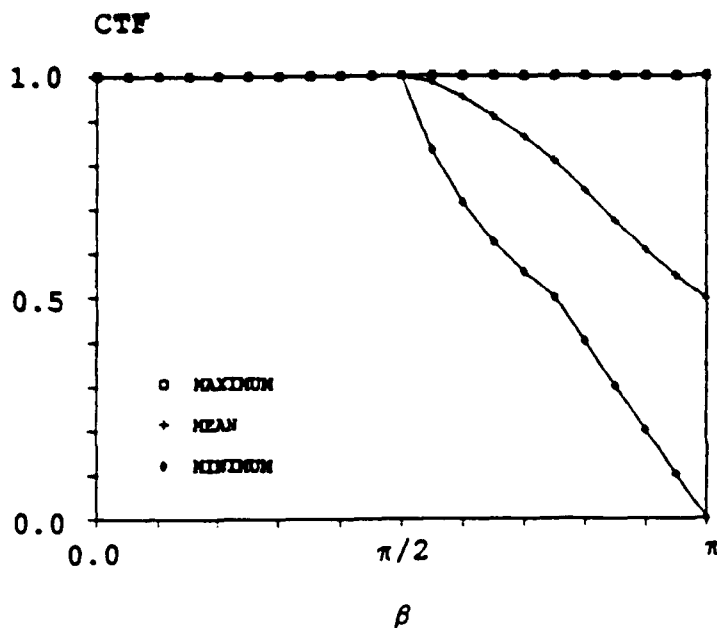
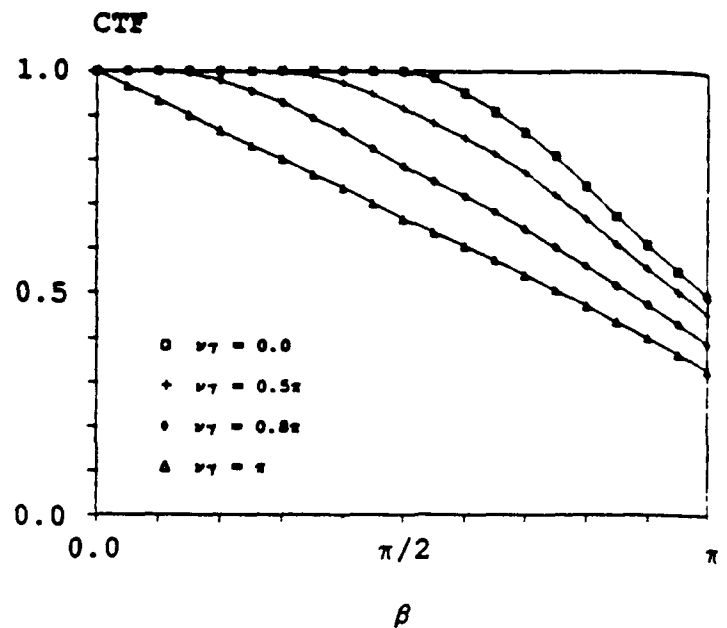
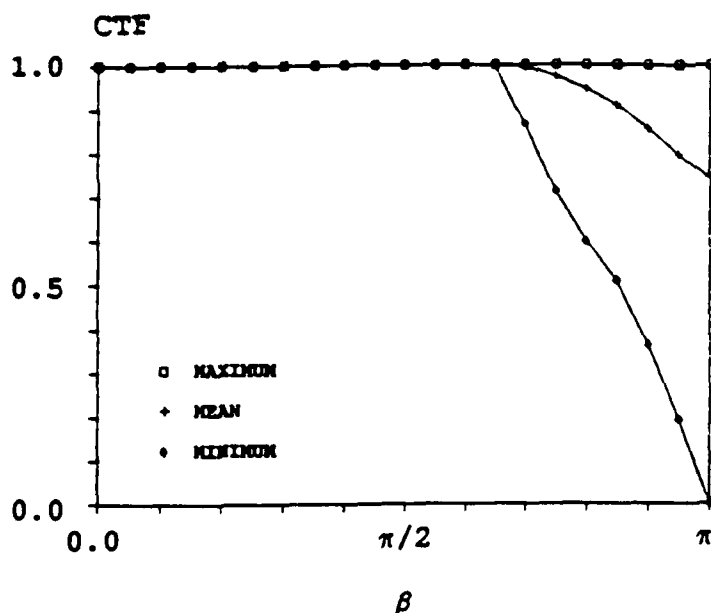
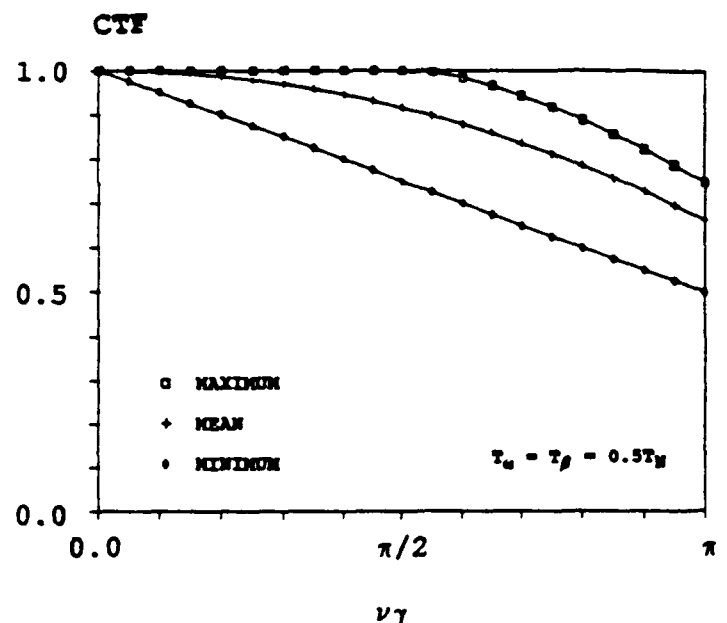


Fig. 19. Variation in CTF due to offset ψ_H for the dynamic line-array case.

response. Systems incorporating CCDs can better meet specifications when designers have this more complete information about device response.

The dynamic MTF graphs, Figs. 13 through 15, and dynamic CTF graphs, Figs. 22 and 23, display the effect of velocity on CCD performance. In all cases, the MTF is reduced significantly for all spatial frequencies. Figure 15 and Table I show conclusively that the velocity effect is not in general separable from the overall MTF calculation. At low velocities, however, the errors introduced by using the separation approximation of Eq. 18

Fig. 20. Static line-array CTF, $T_\alpha = T_\beta$.Fig. 22. Dynamic line-array CTF, $T_\alpha = T_\beta$.Fig. 21. Static line-array CTF, $2T_\alpha = T_\beta$.Fig. 23. Dynamic line-array CTF, $T_\alpha = T_\beta = 0.5T_N$.

are low. In addition, the other case for separability mentioned in the theoretical development also holds, with no errors introduced. No attempt was made to develop velocity separation for the CTF because of the complicated algorithms involved.

The area-array MTF graphs, Figs. 16 and 17, display the effects of oblique images on CCD performance. The important conclusions to be drawn from these graphs is that the line-array calculations apply only along the two axes of an area-array device and that oblique images significantly change the MTF as calculated along either axis. Since the orientation of images is generally unknown, for practical imaging systems, designers should not consider one-dimensional calculations as the typical response of a CCD.

4. CTF MEASUREMENTS

This section describes the CCD system used for experimental tests and the test apparatus. It also describes the test methods and discusses the data obtained from the experiments.

The Texas Instruments TCK103 Evaluation Kit was chosen for experimental analysis. This kit contains the TC103 CCD and support circuitry on one circuit board, requiring only power supplies for operation. The TC103 CCD chip is a 2048 pixel line-array device with pixel width and pixel pitch of 12.7 μm , giving an active region approximately 26 mm in length.

The TCK103 kit was chosen for evaluation primarily because it requires no external circuitry. An optional external circuit was attached to control the scan interval. This external control op-

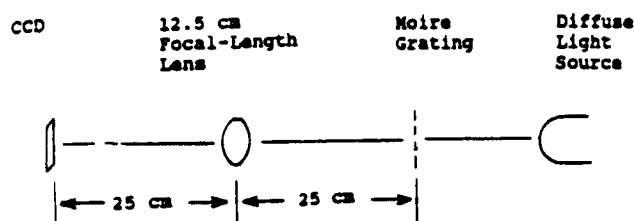


Fig. 24. Diagram of experimental apparatus.

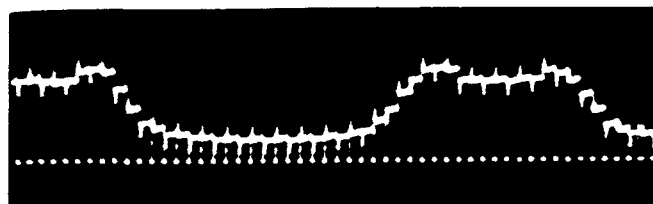


Fig. 25. Photograph of 2 lp/mm output.

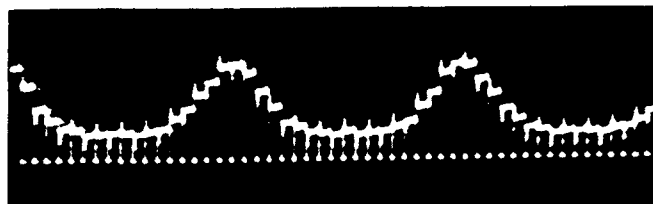


Fig. 26. Photograph of 4 lp/mm output.

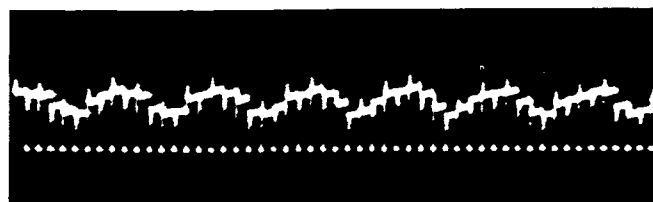


Fig. 27. Photograph of 10 lp/mm output.

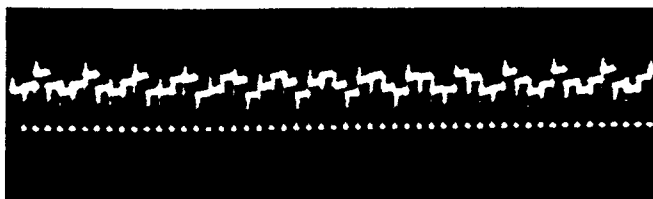


Fig. 28. Photograph of 20 lp/mm output.

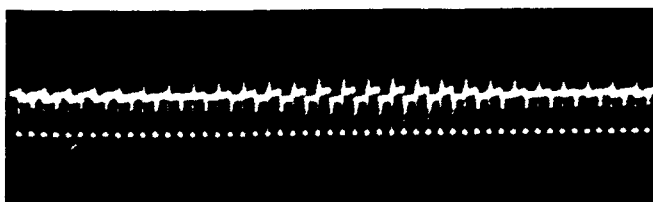


Fig. 29. Photograph of 40 lp/mm output.

TABLE II. Experimental CTF measurements.

Input Pattern Frequency lp/mm	Maximum CTF	Minimum CTF	Mean CTF
2	1.0	1.0	1.0
4	1.0	0.944	0.978
10	1.0	0.922	0.977
20	0.75	0.5	0.616
40	0.45	0.0	0.233

erated the CCD on one clock to stabilize the output display on an oscilloscope. Operating conditions for the CCD were chosen for stable operation of the CCD and minimal distortion in the internal waveforms. The kit proved to be very stable, with no noticeable drift in operating parameters after several hours of continuous operation.

Figure 24 shows the experimental apparatus, which projects a square-wave image from a Newport MGP-series moire grating onto the CCD. CTF measurements can be made directly from an oscilloscope. Five gratings were used, with spatial frequencies of 2, 4, 10, 20, and 40 line pairs per millimeter (lp/mm). The 40 lp/mm image, while just beyond the Nyquist limit of the CCD, was used to establish a limit on the CCD behavior for high input frequencies.

The apparatus was designed to obtain a clean square wave pattern with a zero minimum and low diffraction. This was obtained for the low-frequency inputs. However, diffraction and aberrations could not be completely eliminated and were very noticeable for the 20 and 40 lp/mm gratings. For these gratings, it was not possible to obtain a zero minimum input to the CCD.

Figures 25 through 29 are oscilloscope photographs of the typical output waveforms for the five inputs. Each short horizontal line segment is the output from one pixel. The experimental CTF is calculated by using the measured values of adjacent maxima and minima. Results from these calculations are shown in Table II and are plotted in Fig. 30. The data points for 20 and 40 lp/mm have a high uncertainty, owing to the conditions described earlier.

Figure 30 shows the theoretical and experimental data. The three theoretical curves, maximum, mean, and minimum, do not have labeled data points. Experimental measurements were not taken at enough frequencies to make conclusive remarks about the overall graph. However, the variations in the CTF at each frequency are notable. Although it is not feasible to compare directly the measured and calculated values because of diffraction and other experimental problems, the most significant feature of the theoretical work can be observed: the multivalued nature of the MTF and CTF when used to describe discrete devices.

The multivalued nature shows on the oscilloscope photographs as a beat frequency phenomenon. As ψ_H changes from one line pair to the next, the CTF increases and decreases. The derivations in Sec. 2 predict this variation, as shown in Figs. 18 and 19.

5. DISCUSSION

The theoretical work presented in Sec. 3 provides a detailed examination of the behavior of ideal CCD pixels, as measured by the MTF and CTF. This information is useful not only to the designers of systems incorporating discrete devices such as CCDs but also to the designers of test equipment.

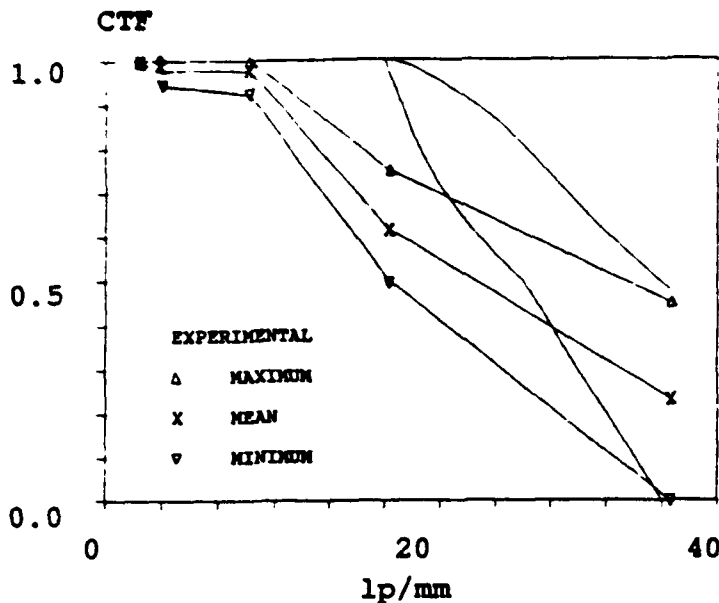


Fig. 30. Comparison between experimental and theoretical CTF.

Figures 11, 12, 18, and 19 are the most significant results of the theoretical work. They provide the ideal MTF and CTF for the frame transfer and interline transfer CCDs. The behavior of CCDs in real systems should be close to that shown in the figures. Designers of CCD-based optical systems should specify CCD requirements by the maximum, mean, and minimum spatial frequency response to achieve desired system performance.

Figure 16 is also significant since it displays the effects of oblique images on area-array CCDs. This result is important because most applications are not limited to images that are aligned with the CCD axes. In general, an image can occur at any orientation, and the angle between the image and the CCD axes will affect the MTF and CTF.

The experimental data presented in Sec. 4 support the theoretical work by demonstrating that the CTF varies over a significant range. Although the results shown in Fig. 30 are not as close to theory as desired, the experimental data and the theoretical curve do exhibit similar features, most noticeably the knee near the frequency of 20 lp/mm.

The variations in the MTF and CTF at a given spatial frequency can be very large and will have a significant effect on system performance. The measured variations presented in Sec. 4 show the effects of sampling. A multivalued MTF or CTF is an unavoidable result of applying a linear space- and time-invariant characterization technique to a discrete device.

All discrete devices, whether used for imaging or display, will exhibit the MTF and CTF characteristics developed herein. Significantly, the combination of discrete imaging and display devices in one system can result in much wider variations in the MTF and CTF than one such device alone. When presented to a human user, the display may fluctuate severely, in both time and space, even with a static source image. Assuming best-case response for all discrete components will probably result in an unusable system.

6. CONCLUSION

This work has presented a detailed mathematical examination of the modulation transfer function and contrast transfer function as applied to discrete devices, particularly charge-coupled de-

vices. The theoretical MTF and CTF have been calculated for a number of widely used CCD configurations. This work has also analyzed the experimental CTF response of a CCD. Because CCDs are time and space variant and the MTF and CTF assume time and space invariance, no unique CCD response can be determined.

A number of extensions to this work are possible. Nonideal pixels, nonuniform pixels, and noise conditions were not considered in the model and could be included in an expanded theoretical effort. In addition, the CTF theory can be expanded to the same level as the MTF theory by accounting for oblique images on an area-array CCD. The experiments can be greatly improved on by using better apparatus, recording more data at more frequencies, incorporating dynamic images, analyzing area-array CCDs, and attempting to measure the MTF as well as the CTF.

The multivalued nature of the MTF and CTF also points out a possible extension: the definition of one or more new characterization methods. Such new methods may include features of the MTF and CTF or be based on different characterization images. New methods that could analyze both continuous and discrete devices without the multivalued problem posed by the MTF and CTF would be very useful for design of optical and electro-optical devices and systems.

7. ACKNOWLEDGMENTS

This work was supported by the University of Dayton Department of Electrical Engineering and by the U.S. Army Center for Night Vision and Electro-Optics, Ft. Belvoir, Va. The author would like to thank T. Williamson for his advice with the experimental setup and D. Moon, J. Westerkamp, and M. Karim for their suggestions and recommendations.

8. REFERENCES

1. W. S. Boyle and G. E. Smith, "Charge coupled semiconductor devices," *Bell Syst. Tech. J.* 49, 587-593 (1970).
2. J. R. Janesick, T. Elliott, S. Collins, M. M. Blouke, and J. Freeman, "Scientific charge-coupled devices," *Opt. Eng.* 26(8), 692-715 (1987).
3. S. B. Campana, "Techniques for evaluating charge-coupled imagers," *Opt. Eng.* 16(3), 267-274 (1977).
4. J. W. Coltman, "The specification of imaging properties by response to a sine wave input," *JOSA* 44, 468-471 (1954).
5. L. W. Schumann and T. S. Lomheim, "Modulation transfer function and quantum efficiency correlation at long wavelengths (greater than 800 nm) in linear charge coupled imagers," *Appl. Opt.* 28(9), 1701-1709 (1989).
6. J. C. Feltz and M. A. Karim, "The modulation transfer function of charge-coupled devices," *Appl. Opt.* 29(5), 717-722 (1990).
7. A. A. S. Awwal, A. K. Cherm, M. A. Karim, and D. L. Moon, "Dynamic response of an electro-optical imaging system," in *Helmet-Mounted Displays*, J. T. Carollo, ed., *Proc. SPIE* 1116, 185-197 (1989).
8. L. Levi, "Spatiotemporal transfer function: recent developments," *Appl. Opt.* 22, 4038-4041 (1983).



John C. Feltz received the BEE and MSEE degrees from the University of Dayton in 1988 and 1989, respectively. He is currently employed by Systems Research and Applications Corporation, Arlington, Va., where he is a software design and test engineer working with communications, imaging, and optical storage systems. Mr. Feltz is a member of the IEEE and the National Society of Professional Engineers.

Device nonspecific minimum resolvable temperature difference for infrared imaging systems characterization

M. L. Gao
M. A. Karim, MEMBER SPIE
S. H. Zheng
University of Dayton
Electrical Engineering Department
300 College Park Avenue
Dayton, Ohio 45469-0226

Abstract. A generalized minimum resolvable temperature difference (MRTD) formulation is identified for the characterization of infrared detection systems. The generalized MRTD equation can be adapted to suit the needs of any IR system to be tested. As an illustration, the MRTD of a staring IR detection system is derived from the generalized MRTD formulation.

Subject terms: electro-optical displays; minimum resolvable temperature difference; infrared systems; signal-to-noise ratio; modulation transfer function; scanning detectors; staring detectors; noise equivalent temperature difference.

Optical Engineering 29(8), 905-910 (August 1990).

CONTENTS

1. Introduction
2. MRTD concept
3. Generalized MRTD formulation
4. Ratches MRTD
5. Staring MRTD
6. Discussion
7. Acknowledgment
8. Appendixes
 - 8.1. Derivation of Eq. (17)
 - 8.2. Derivation of Eq. (20)
9. References

1. INTRODUCTION

The infrared community almost universally accepts as axiomatic that the minimum resolvable temperature difference (MRTD) is the parameter that is indicative of the performance of thermal imaging systems, which may consist of individual components such as an IR detector, a cooling system, an IR-to-visual converter, and a display. The present form of the MRTD equation,¹⁻³ though limited in scope, has been used successfully for many years. This MRTD model, commonly referred to as the Ratches model, is valid only for particular IR imaging systems. Since the publication of the Ratches model in 1975, however, much progress has been made both in the measurement and design of IR imaging systems. Accordingly, the Ratches model now needs to be improved or modified to adapt to the changing IR devices and IR imaging concepts.

A recent work has already pointed out several important aspects that have to be incorporated to suit the needs of newer IR systems.⁴ However, just as the Ratches model is for a special IR imaging system, namely, the series scan system along horizontal direction, all of the improved MRTD models^{5,6} are also for special systems or devices. None of these MRTD formula-

tions is general enough and, therefore, cannot be adapted to an arbitrarily new IR system. For example, there exists no reliable MRTD formulation that can be used for the testing of staring IR systems.⁷ Staring IR systems are the most recent addition to the already existing IR systems and are expected to perform better than the scanning systems in terms of temporal frequency response, spatial frequency response, quality of imaging, and sensitivity.

In this work, we formulate a universal MRTD equation that is then used, as an example, in the derivation of the MRTD suitable for the staring IR systems.

2. MRTD CONCEPT

The MRTD is defined with a standard experiment,⁸ shown in Fig. 1. The test system can be considered as a nonfeedback linear system. The test configuration consists of a target (involving a blackbody source, an ambient plate, a standard test pattern, and collimating optics), the to-be-tested IR equipment, and the eye-brain system. In general, the test pattern shown in Fig. 2 is standard.

In the MRTD test, the test pattern is placed at the focal plane. Initially, the temperature difference ΔT between the test pattern and the ambient plane is set equal to zero. The ΔT is then adjusted until three out of four observers agree that the pattern is discernible as a four-bar pattern. This ΔT is the MRTD value for the system under consideration at that spatial frequency. The procedure is then repeated with different test patterns, each having a different spatial frequency. Finally, the MRTD curve is obtained by plotting ΔT as a function of spatial frequency.

3. GENERALIZED MRTD FORMULATION

The MRTD model is based on two essential hypotheses. As in the Ratches model, it is assumed that the only fact that can affect the recognition of a scene is the signal-to-noise ratio of the scene. When the SNR exceeds a particular threshold value SNR_{th} , the test pattern becomes recognizable. Another hypothesis underlying the current work is the concept of "matched filter." The

Invited Paper EO-110 received Jan. 4, 1990; revised manuscript received March 1, 1990; accepted for publication May 22, 1990.
© 1990 Society of Photo-Optical Instrumentation Engineers.

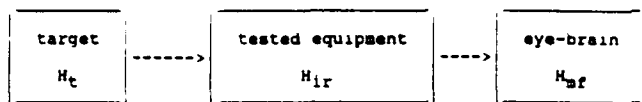


Fig. 1. Standard test system for measuring MRTD.

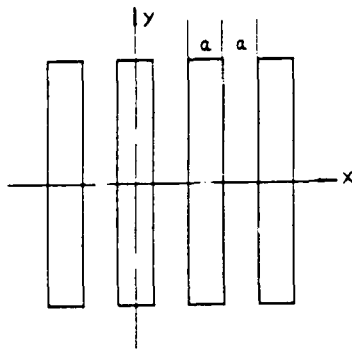


Fig. 2. Standard MRTD target pattern.

eye-brain system is considered as a matched filter. This filter is not real, signal and noise are not really filtered through it. The filter functions by maximizing the SNR only. Its characteristics depend on the spectral distributions of both signal and noise. Generally speaking, this matched filter consists of two parts: eye and brain.

In this paper, we use H_{mf} , H_e , and H_b to represent the transfer functions of the matched filter, eye, and brain, respectively. In the Laplace domain,⁹ also referred to as the s-domain,

$$H_{mf}(s) = H_e(s)H_b(s). \quad (1)$$

Note that the signal is defined in terms of its peak-to-peak value and the noise is measured by its rms value. The basic MRTD equation now can be formulated as follows. The two-dimensional image distribution on the display screen is given by

$$e_d(x,y) = \Delta T i_d(x,y), \quad (2)$$

where ΔT is the temperature difference between the bars and background and $i_d(x,y)$ is the normalized image distribution incident on the display screen.

Considering the relationship between the normalized image distribution $i_d(x,y)$ on the display screen and the normalized target distribution $i_t(x,y)$ on the object plane, $i_d(x,y)$ is obtained as:

$$i_d(x,y) = \iint_{-\infty}^{+\infty} I_t(f_x, f_y) H_{ir}(f_x, f_y) \exp[j2\pi(f_x x + f_y y)] df_x df_y, \quad (3)$$

where $H_{ir}(f_x, f_y)$ is the transfer function of the to-be-tested equipment and $I_t(f_x, f_y)$ is the Fourier transform of the normalized target distribution. In other words, $I_t(f_x, f_y)$ is just $H_t(f_x, f_y)$, the transfer function of the target. Combining Eqs. (2) and (3), the image distribution on the display screen can be expressed as

$$e_d(x,y) = \Delta T \iint_{-\infty}^{+\infty} H_t(f_x, f_y) H_{ir}(f_x, f_y) \exp[j2\pi(f_x x + f_y y)] df_x df_y. \quad (4)$$

By definition, the signal is the peak-to-peak value of the image. Thus, corresponding to Fig. 2, the signal on the display screen s_d , can be determined from the difference of $e_d(0,0)$ and $e_d(a,0)$. Note also that the input signal is ΔT , a difference value. Thus by arbitrarily setting $e_d(a,0)$ as zero, s_d is given by

$$s_d = e_d(0,0) = \Delta T \iint_{-\infty}^{+\infty} H_t H_{ir} df_x df_y. \quad (5)$$

Finally, the perceived signal may be obtained as

$$s_p = \Delta T \iint_{-\infty}^{+\infty} H_t H_{ir} H_{mf} df_x df_y. \quad (6)$$

This signal will be used for formulating the SNR.

Noise is contributed dominantly by the fluctuation of the incoming photon flux striking the IR equipment to be tested.⁵ Other subsystems in the test system, of course, contribute some noise. However, for simplicity, we assume that there is no built-in noise source in the IR device to be tested. Let the noise power spectral density¹⁰ (caused by the fluctuation of photon flux) incident at the to-be-tested device be $W(f_x, f_y)$. According to the theory of random process,¹¹ the output noise power spectral density of a linear system is equal to WH^2 , where H is the transfer function of the system. The perceived noise power spectral density is thus given by $W(f_x, f_y) H_{ir}^2(f_x, f_y) H_{mf}^2(f_x, f_y)$.

An extremely important relationship between the noise power spectral density and the variance σ (at a point) of a random process is given by

$$\sigma^2 = \iint_{-\infty}^{+\infty} W(f_x, f_y) df_x df_y. \quad (7)$$

If we consider σ as the corresponding rms noise value,¹ then the total perceived rms noise value of the test system becomes

$$n_p = \left[\iint_{-\infty}^{+\infty} WH_{ir}^2 H_{mf}^2 df_x df_y \right]^{1/2}. \quad (8)$$

Now we may obtain the SNR as

$$\text{SNR} = \frac{s_p}{n_p} = \frac{\Delta T \iint_{-\infty}^{+\infty} H_t H_{ir} H_{mf} df_x df_y}{\left[\iint_{-\infty}^{+\infty} WH_{ir}^2 H_{mf}^2 df_x df_y \right]^{1/2}}. \quad (9)$$

Equation (9) has a straightforward implication. The SNR associated with any generic IR system is evaluated by specifying only ΔT and W as inputs. By setting a specific SNR as the threshold value for a human, the relevant expression of MRTD is found to be

$$\text{MRTD} = \frac{\text{SNR}_{th} \left[\iint_{-\infty}^{+\infty} WH_{ir}^2 H_{mf}^2 df_x df_y \right]^{1/2}}{\iint_{-\infty}^{+\infty} H_t H_{ir} H_{mf} df_x df_y}. \quad (10)$$

where SNR_{th} is the threshold value of the SNR for the human eye. The universal MRTD expression as given by Eq. (10) has been derived from the three most basic system blocks shown in Fig. 1. For understanding and use of the formula, the five parameters of the equation are elaborated next.

H_t is the transfer function of the four-bar standard test target, which in turn is a function of spatial frequency. This is why MRTD is the function of spatial frequency of the test target. There have been many works^{1,3,5} that provide many different forms for H_t with different approximations. The systems designer who plans to use the universal MRTD expression can select the one that is most suitable to his or her design. H_{ir} is the transfer function of the IR device to be tested, which is just what the designers have to design. W represents the input noise that, in general, can be a white noise. Finally, H_{mf} and SNR_{th} are quantities that depend on the human visual psychophysics. All of the terms of the MRTD expression are nothing but system parameters that can be certainly calculated or estimated.

For convenience, the test pattern h_t can be taken to be

$$h_t(x,y) = \text{rect}\left(\frac{x}{a}\right) * \text{comb}\left(\frac{x}{a}\right), \quad (11)$$

for which the corresponding transfer function is

$$H_t(f_x, f_y) = \text{sinc}(af_x) \text{comb}(af_x). \quad (12)$$

In this expression of H_t , two assumptions are made: the four-bar pattern is assumed to be infinitely extensive along the y-direction and periodic and infinitely extensive along the x-direction.

The H_{mf} is given by Eq. (1), while H_e can be approximated as $\exp(-Df/M)$, where D is a light-level-dependent parameter and M is the system magnification.⁶ Again, H_b is given by $H_c(f_x, f_y)H_{ir}(f_x, f_y)H_d(f_x, f_y)$, where H_c is the normalized Fourier transform of a single bar selected by the eye from the four-bar target such that $H_c(0,0) = 1$.⁵ In the derivation of H_b the input noise is assumed to be white. The system designer may determine H_{mf} for other types of noise, too.

Equation (10) can be considered the most basic formula of MRTD. Most of the other MRTD formulations are device specific expressions. In practice, both the test system and the IR equipment to be tested may have different configurations. For example, an MRTD formula may involve the transfer function of an optical subsystem, provided the designer could identify and characterize an optical subsystem of the test system. However, another formula may not involve such a term when the system designer is not able to individually characterize the optical subsystem. Thus, it often becomes confusing for the MRTD users to apply the MRTD formula with certainty. The modular form of Eq. (10) makes it very easy for every systems designer to derive an MRTD formula suitable for his or her own system. In the next section, as an example, the basic formula of Eq. (10) is used to derive the Ratches MRTD.

4. RATCHES MRTD

In the Ratches model,¹

$$H_{mf} = H_w(f_x)H_l(f_y)H_{ir}(f_x), \quad (13)$$

$$H_{ir} = H_{ir}(f_x)H_{ir}(f_y) = H_{elect}(f_x)H_d(f_x, f_y), \quad (14)$$

$$H_t = H_w(f_x)H_l(f_y) \quad (15)$$

where $H_w(f_x)$ is the transfer function of the width of the four-bar target, $H_l(f_y)$ is the transfer function of the length of the four-bar target, $H_{elect}(f_x)$ is the transfer function of the electronic part of the IR device to be tested, and $H_d(f_x, f_y)$ is the transfer function of the display screen. Using Eq. (6), the perceived signal for the scanning IR device is found to be

$$\begin{aligned} s_p &= \Delta T \iint_{-\infty}^{+\infty} H_t H_{ir} H_{mf} df_x df_y \\ &= \Delta T \iint_{-\infty}^{+\infty} [H_w(f_x)H_l(f_y)] [H_{ir}(f_x)H_{ir}(f_y)] \\ &\quad \times [H_w(f_x)H_l(f_y)H_{ir}(f_x)] df_x df_y \\ &= \Delta T \int_{-\infty}^{+\infty} [H_w(f_x)]^2 H_{ir}(f_x) df_x \int_{-\infty}^{+\infty} [H_l(f_y)]^2 [H_{ir}(f_y)]^2 df_y. \end{aligned} \quad (16)$$

The first integral of Eq. (16) involves pertinent scanning characteristics. It can be evaluated (as shown in Sec. 8.1) to give

$$\int_{-\infty}^{+\infty} H_w(f_x)^2 H_{ir}(f_x) df_x = \frac{k}{\Delta y_i v} \text{MTF}(f_0) \frac{8}{\pi^2}, \quad (17)$$

where Δy_i is the distance between scan lines, v is the scan velocity of the display element, k is a constant for adjusting units, and $\text{MTF}(f_0)$ is the modulation transfer function¹⁰ of the to-be-tested device. Therefore, the perceived Ratches signal becomes

$$s_p = \frac{k}{\Delta y_i v} \text{MTF}(f_0) \frac{8}{\pi^2} TL \int_{-\infty}^{+\infty} H_t^2 H_{ir}^2 df_x, \quad (18)$$

where L accounts for the normalization of H_t . Equation (8) can be used to determine the perceived Ratches noise:

$$\begin{aligned} n_p &= \left[\iint_{-\infty}^{+\infty} W H_{ir}^2 H_{mf}^2 df_x df_y \right]^{1/2} \\ &= \left[\iint_{-\infty}^{+\infty} W (H_{elect}^2 H_d^2) [H_w^2 H_l^2] [H_{ir}(f_y)]^2 df_x df_y \right]^{1/2}. \end{aligned} \quad (19)$$

The noise spectral density W can be found (as shown in Sec. 8.2) to be

$$W(f) = \frac{k^2 \text{NETD}^2}{v \Delta f_n^2} \frac{W(f_x)}{W(f_{0x})}, \quad (20)$$

where NETD is the noise equivalent temperature difference, Δf_n is the noise bandwidth of the test system, and f_{0x} is the frequency

of the test bar pattern along the x-direction. Thus, the perceived Ratches noise becomes

$$n_p = \left[\frac{k^2 \text{NETD}^2}{v \Delta f_n^2} \frac{W(f_x)}{W(f_{0x})} \int_{-\infty}^{+\infty} H_{\text{elect}}^2 H_d^2 H_w^2 H_i^2 H_r^2 df_x df_y \right]^{1/2} \quad (21)$$

Using Eqs. (18) and (21), the SNR is thus obtained as

$$\text{SNR} = \frac{\frac{k}{\Delta v, v} \text{MTF}(f_0) \frac{8}{\pi^2} TL \int_{-\infty}^{+\infty} H_i^2 H_r^2 df_y}{\left[\frac{k^2 \text{NETD}^2}{v \Delta f_n^2} \frac{W(f_x)}{W(f_{0x})} \int_{-\infty}^{+\infty} H_{\text{elect}}^2 H_d^2 H_w^2 H_i^2 H_r^2 df_x df_y \right]^{1/2}} \quad (22)$$

It must be noted that the calculated SNR is valid for a single frame only. The MRTD, however, should account for all frames during an eye integration time. Therefore, the MRTD is found to be

$$\begin{aligned} \text{MRTD} &= \frac{\pi^2}{8} \frac{\text{SNR}_{th}}{\text{MTF}(f_0)} \frac{\text{NETD}}{L \int_{-\infty}^{+\infty} H_i^2 H_r^2 df_y} \\ &\times \left[\frac{\Delta v, v}{F_R t_E \Delta f_n} \int_{-\infty}^{+\infty} \frac{W(f_x)}{W(f_{0x})} H_{\text{elect}}^2 H_d^2 H_w^2 H_i^2 H_r^2 df_x df_y \right]^{1/2} \end{aligned} \quad (23)$$

where F_R is the frame rate of the IR system to be tested and t_E is the integration time of the human eye. Using the following definitions and relations,¹

$$q_y = L \int_{-\infty}^{+\infty} H_i^2 H_r^2 df_y \cong 1 \quad (24)$$

$$Q_x = \frac{1}{f_0} \int_{-\infty}^{+\infty} \frac{W(f_x)}{W(f_{0x})} H_{\text{elect}}^2 [H_d(f_x)]^2 H_w^2 df_x \quad (25)$$

$$Q_v = L \int_{-\infty}^{+\infty} H_i^2 H_r^2 [H_d(f_v)]^2 df_v \quad (26)$$

$$L = \frac{7}{2f_0} \quad (27)$$

the scanning MRTD reduces to

$$\text{MRTD} = \frac{\pi^2 \text{SNR}_{th}}{4(14)^{1/2}} \frac{\text{NETD} f_0}{\text{MTF}(f_0)} \left(\frac{\Delta v, v}{F_R t_E \Delta f_n Q_x} \right)^{1/2} \quad (28)$$

which is just the Ratches MRTD formula. In the next section, as another example of the use of the generalized formula, the MRTD for a mosaic staring IR system is derived.

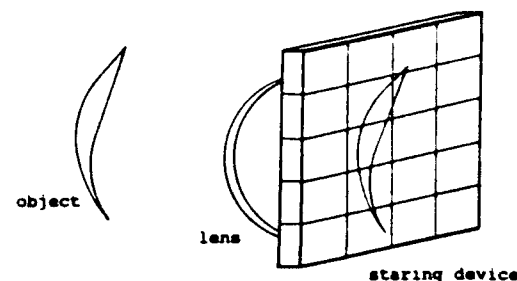


Fig. 3. Staring IR device.

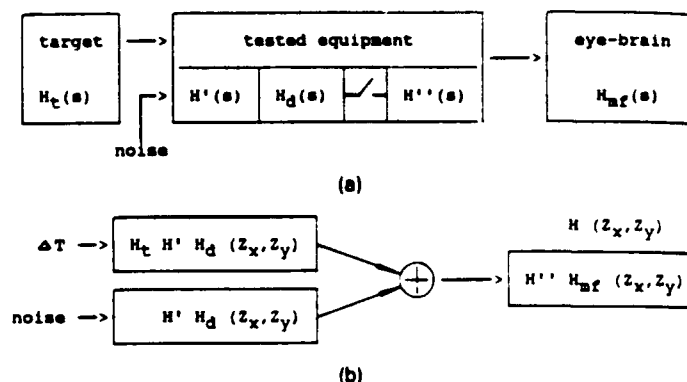


Fig. 4. MRTD model: (a) s-domain and (b) Z-domain.

5. STARING MRTD

The mosaic staring IR device (Fig. 3), as implied by its name is a discrete-data system. One of the mathematical tools devised for the analysis and design of a discrete-data system is the Z-transform.⁹ In our work, we use Z-transforms to establish the transfer function for the mosaic staring device, although a more powerful method, the state variable method, has gained greater significance in the studies of discrete-data systems.

Usually, the Z-transform expression of a system is not obtained directly from the time domain or spatial domain but from the Laplace (s-) domain. In this case, the transform is quite straightforward. Considering the system shown in Fig. 4(a), we notice that there is only one sampling switch that follows H (actually an array of switches in two dimensions, as implied by the term "staring"). According to the basic operation of transform from s-domain to Z-domain,⁹ the MRTD expression for the mosaic staring system can be directly obtained from Eq. (10) to give

$$\text{MRTD} = \frac{\text{SNR}_{th} \left\{ \int_{-\infty}^{+\infty} \int_{-\infty}^{+\infty} W(Z_x, Z_y) [H' H_d](Z_x, Z_y)^2 H(Z_x, Z_y)^2 dZ_x dZ_y \right\}^{1/2}}{\int_{-\infty}^{+\infty} \int_{-\infty}^{+\infty} [H H' H_d](Z_x, Z_y) H(Z_x, Z_y) dZ_x dZ_y} \quad (29)$$

where $H(Z_x, Z_y)$ accounts for all of the subsystems of the test system that follow the detector and H' accounts for all subsystems of the to-be-tested equipment that precede the detector. It should be noted that the notation $[H' H_d](Z_x, Z_y)$ does not mean

$H'(Z_s, Z_v)H_d(Z_s, Z_v)$.⁹ Figure 4(a) shows the block diagram of the system in the s -domain. According to the transform rules, all blocks present in between a pair of switches or a switch and the input/output terminal are combined together as a single block with argument s . The expression pertaining to the new block given by $H'H_d(s)$ has been transformed into the corresponding Z -domain term, $H'H_d(Z)$. Figure 4(b) shows the corresponding systems block diagram in the Z -domain.

6. DISCUSSION

We have developed a device nonspecific MRTD formula that is significantly different from the traditional MRTD formulations. Most of its modular terms refer to subsystem transfer functions. Furthermore, unlike the traditional MRTD, the generalized MRTD formulation is not tied with the NETD.

Equation (10) may appear to be inconvenient for the designers of IR imaging systems because of the lack of detailed systems parameters. However, because of this, it has more flexibility to adapt to all kinds of IR imaging systems. We showed that the device nonspecific formulation can be used to derive the Ratches MRTD for the scanning IR system. For illustration, we have also used the generalized MRTD formulation for deriving the MRTD of a staring IR system.

7. ACKNOWLEDGMENT

The authors would like to acknowledge the research support provided in part by U.S. Army Research Office contract DAAL03-87-K-0121 with the University of Dayton.

8. APPENDIXES

8.1. Derivation of Eq. (17)

The first integral of Eq. (16) can be also evaluated in the spatial domain as

$$[H_w(f_x)]^2 H_{ir}(f_x) \longleftrightarrow h_w(x) * h_w(x) * h_{ir}(x), \quad (30)$$

where the asterisk represents the convolution operation. For the standard test pattern shown in Fig. 2, $h_w(x)$ corresponds to a square wave that can be approximated by its first harmonic, which is $4/\pi$ times the amplitude of the square wave, as

$$h_w(x) = \frac{4}{\pi} (0.5) \sin(2\pi f_0 x) + 0.5, \quad (31)$$

where f_0 is the horizontal spatial frequency of the standard target pattern. The bias value of (0.5) guarantees that $h_w(x)$ is non-negative. Since

$$h_w(x) * h_{ir}(x) \equiv \text{MTF}(f_0) \frac{4}{\pi} (0.5) \sin(2\pi f_0 x) + C, \quad (32)$$

where $\text{MTF}(f_0)$ is the modulation transfer function¹⁰ of the detector to be tested and C is a constant, Eq. (30) can be evaluated as

$$\begin{aligned} h_w(x) * h_w(x) * h_{ir}(x) &= h_w(x) * \left[\text{MTF}(f_0) \frac{4}{\pi} (0.5) \sin(2\pi f_0 x) + C \right] \\ &= \int_{-1/2f_0}^{+1/2f_0} \left[\text{MTF}(f_0) \frac{4}{\pi} (0.5) \sin(2\pi f_0 x) (2f_0) + C \right] dx. \end{aligned} \quad (33)$$

where the rect function under consideration is taken to have a width $1/2f_0$ and an amplitude of $2f_0$ such that $H(f_x) = 1$ when $f_x = 0$. Considering the fact that we are interested only in the peak value of Eq. (33) (since the minimum value was assumed to be zero), Eq. (30) reduces to

$$\begin{aligned} [h_w(x) * h_w(x) * h_{ir}(x)] &= \text{MTF}(f_0) \frac{4}{\pi} \int_0^{1/2f_0} \sin(2\pi f_0 x) (2f_0) dx \\ &= \text{MTF}(f_0) \frac{4}{\pi} \frac{2}{\pi} = \frac{8}{\pi^2} \text{MTF}(f_0). \end{aligned} \quad (34)$$

To have identical units for both Eq. (34) and the perceived noise, it is necessary to multiply the result with a coefficient k such that $k\Delta T$ yields the power emitted by a display element. Again, for the purpose of normalization with the area of the display screen, Eq. (34) is divided by $\Delta y_i v$, where Δy_i is the distance between scan lines and v is the scan velocity of the display element. Consequently, Eq. (34) gives

$$\int_{-\infty}^{\infty} [H_w(f_x)]^2 H_{ir}(f_x) dx = \frac{k}{\Delta y_i v} \frac{8}{\pi^2} \text{MTF}(f_0). \quad (35)$$

8.2. Derivation of Eq. (20)

$W(f)$ can be expressed as

$$W(f) = C \frac{W(f)}{W(f_0)}, \quad (36)$$

where $C = W(f_0)$. Note that the NETD equals the temperature difference corresponding to the condition $\text{SNR} = 1$. Therefore, if the signal is simply ΔT , the NETD equals ΔT such that $\Delta T/\sigma = 1$, where σ is the rms noise. Thus, NETD equals σ . However,

$$\sigma^2 = \int_0^{+\infty} C \frac{W(f)}{W(f_0)} df = C \int_0^{+\infty} \frac{W(f)}{W(f_0)} df, \quad (37)$$

and the noise bandwidth of the test system is given by

$$\Delta f_n = \int_0^{+\infty} \frac{W(f)}{W(f_0)} df. \quad (38)$$

By comparing Eqs. (37) and (38), we find

$$C = \frac{\sigma^2}{\Delta f_n} = \frac{\text{NETD}^2}{\Delta f_n}. \quad (39)$$

Equation (36) can now be expressed as

$$W(f) = \frac{\text{NETD}^2}{\Delta f_n^2} \frac{W(f)}{W(f_0)}. \quad (40)$$

As in the first appendix, equivalent radiant energy can be determined by replacing NETD with $\text{NETD}(k/v)$. Again, since $f = vf_x$,

$$\frac{W(f)}{W(f_0)} = v \frac{W(f_x)}{W(f_{0x})}. \quad (41)$$

and therefore Eq. (41) leads to

$$W(f) = \frac{k^2 \text{NETD}^2}{v^2} \frac{1}{\Delta f_n} v \frac{W(f_x)}{W(f_{0x})}$$

$$= \frac{k^2 \text{NETD}^2}{v \Delta f_n^2} \frac{W(f_x)}{W(f_{0x})} \quad (42)$$

9. REFERENCES

1. J. A. Ratches, W. R. Lawson, L. P. Obert, R. J. Bergemann, T. W. Cassidy, and J. M. Swenson, "Night vision laboratory static performance model for thermal viewing systems," U.S. Army Electronics Command Report 7043 (April 1975).
2. J. A. Ratches, "Static performance model for thermal imaging systems," *Opt. Eng.* 15(6), 525-530 (1976).
3. J. M. Lloyd, *Thermal Imaging Systems*, Plenum Press, New York (1973).
4. W. McCracken and L. Wajsfelner, "MRTD as a figure of merit," in *Thermal Imaging*, Proc. SPIE 636, 31-35 (1986).
5. J. G. Vortman and A. Bar-Lev, "Improved MRTD for IR imaging systems," in *Infrared Technology and Applications*, Proc. SPIE 590, 193-204 (1986).
6. G. Kornfeld and W. R. Lawson, "Visual perception model," *JOSA* 61, 811-817 (1971).
7. I. J. Spiro and M. Schlessinger, *Infrared Technology Fundamentals*, Marcel Dekker, New York (1989).
8. J. T. Wood, W. J. Bentz, T. Pohle, and K. Hepfer, "Specification of thermal imagers," *Opt. Eng.* 15(6), 531-536 (1976).
9. B. C. Kuo, *Digital Control System*, Holt, Rinehart, & Winston, New York (1980).
10. M. A. Karim, *Electro-Optical Devices & Systems*, PWS-Kent Publ., Boston (1990).
11. A. Papoulis, *Probability, Random Variables, and Stochastic Processes*, McGraw-Hill, New York (1984).



Ming L. Gao is a Ph.D. student in the Electrical Engineering Department at the University of Dayton. His dissertation research involves the evaluation of display systems and thermal imaging systems. Gao received his BS degree in radioelectronics from Tsinghua University (China) in 1968 and his MS degree in electrical engineering from Hefei Polytechnic University (China) in 1981. Prior to beginning his Ph.D. he worked as an engineer for the Liao-yuan Radio Company in China.

Mohammad A. Karim: Biography and photograph appear with the special issue guest editorial in this issue.



Song H. Zheng is a Ph.D. student in the Electrical Engineering Department at the University of Dayton. Her dissertation research involves the study of optical pattern recognition based on an amplitude-modulated inverse filter. Zheng received her BE degree in mechanical engineering from Shanghai Institute of Mechanical Engineering (China) in 1982 and her MS degree in physics from Eastern Michigan University in 1988. Prior to beginning her MS program Zheng served as an assistant director of the Shanghai Medical Equipment Research Institute in China.

Dynamic modulation transfer function of a display system

A. A. S. Awwal, A. K. Cherri, M. A. Karim, and D. L. Moon

A theoretical model for characterizing the dynamic response of a nonscanning electrooptic display system is developed. The model interrelates the spatial frequency degradations of an image display with both phosphor characteristics and relative velocity of the displayed object. Thereafter, the analysis is extended to compare the performances of types P-20, P-42, and P-1052 phosphor based displays.

I. Introduction

The characteristics of an imaging system are usually provided by either a spatial response known as the point spread function¹ or the magnitude of the spatial frequency response known as the modulation transfer function (MTF).² Both of these measures are static parameters,³ and accordingly neither is sufficient for a complete understanding of the overall image quality. The absence of temporal response considerations in the analysis of an imaging system, in situations such as driving and piloting tasks, results in drastically degraded modulation contrast particularly at higher spatial frequencies.³ This effect may be particularly significant, for example, when night vision goggles (NVGs) designed for use in the static mode are used by the pilots of a helicopter. In such dynamic situations, targets as seen by the NVGs begin to blend with backgrounds, and the user may fail to discriminate targets from their backgrounds.

The MTF, defined as the modulus of the Fourier transform of the line spread function,⁴ is a 1-D quantity which is measured along only one direction. Generally, it is assumed that the same frequency response is exhibited in all directions. Accordingly, the MTF refers to a circularly symmetric frequency response. In practice, however, the MTF is direction dependent.⁵ A frequency response derived from a 2-D point spread function is expected to provide a more accurate picture of the MTF. Furthermore, the discrete nature of

some of the display systems prevents a slant edge from being displayed with the same quality as a horizontal or vertical edge.⁶

In specifying the MTF, its phase part is generally neglected. But it is often the phase that differentiates a function $h(x,y)$ from its reflected version $h(-x,-y)$. A display system responds differently when the displayed object is in relative motion with the sensor than when there is no relative motion. The conventional MTF thus fails to characterize the actual behavior of a dynamic system. In this paper, we develop an analytical tool so that the dynamic parameters can be used to specify the performance of a nonscanning electrooptical display system such as those in NVGs, intensifier tubes,⁷ and cameras. On one hand, this model overcomes the discrepancies of the earlier system specification, and, on the other hand, proper quantification of dynamic response enables one to restore the motion-degraded displays.

II. Impulse Response of Imaging Systems

In electrical system analysis, the impulse response is used for estimating the response due to any time-varying signal. Testing a system with an impulse signal is equivalent to testing the system with every spatial frequency at the same time. In general, the transform of the system output provides a transfer function which is the temporal frequency response of the system. When the response of a system is instantaneous and when a δ -function input produces a δ -function output, the system response is said to be a constant for all frequencies. The advantage of an impulse input specification is that any signal can be expressed as a series of impulse functions separated in time so that the overall output can be found by convolving the sum of the input signals with the impulse response.

The modulus of the Fourier transform of the 2-D point spread function can be used to yield the 2-D

The authors are with University of Dayton, Department of Electrical Engineering, Center for Electro-Optics, 300 College Park Avenue, Dayton, Ohio 45469-0226.

Received 16 October 1989.

0003-6935/91/020201-05\$05.00/0.

© 1991 Optical Society of America.

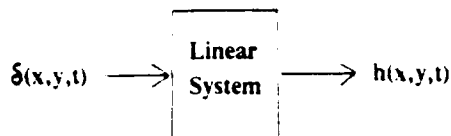


Fig. 1. Linear system showing 3-D impulse response.

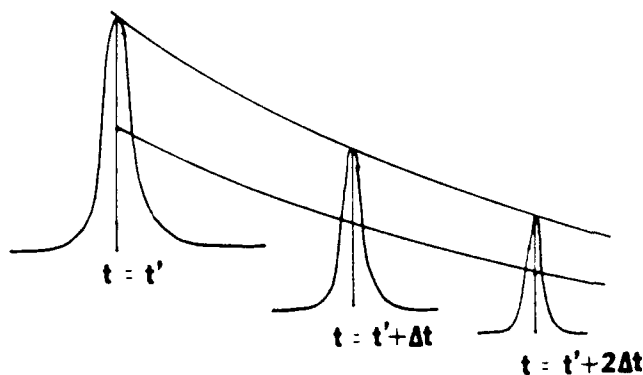


Fig. 2. Three-dimensional impulse response.

MTF.¹ Experimentally, a system can be illuminated with a point source of light (for a certain amount of time), and then its response can be measured.⁸ By incorporating the sense of time and space, one can define a 3-D impulse response⁹ that behaves like an impulse function in both space and time. Accordingly, we define a 3-D impulse response $h(x,y,t)$ as the response to a narrow pinhole of light applied to a system for an infinitesimally short duration of time.¹⁰ Conveniently, the input/output relation can be expressed schematically as in Fig. 1.

fied whenever the function can be expressed as a product of two individual functions—one of which is spatial while the other is temporal.

Since our interest is in nonscanning display devices, temporal parameters due to electron beam sweep time as that in a cathode ray tube based display need not be considered. It is well known that phosphors (used in many of the display devices) are associated with exponential decay characteristics.¹¹ This implies that the luminance can be expressed as a product of an initial luminance value and a time factor. In phosphor based display devices, therefore, the effect of a 3-D impulse input can be expressed as an initial point spread function multiplied by an exponential decay factor¹²:

$$h(x,y,t) = s(x,y)\Delta(t), \quad (3)$$

where $\Delta(t) = \exp(-t/\tau)$ is the dynamic part of the point impulse response. Figure 2 illustrates the time history of a 2-D point spread function. Provided the decay is exponential, it can be shown (by normalizing the function with respect to space and time) that the spatial and temporal parts of the impulse response are separable.¹⁰ In other words, when the intensity can be expressed as a product of initial intensity I_0 multiplied by a time function, the 3-D impulse response is separable. Note, however, that the temporal part is not necessarily separable from the spatial part when the decay rate is constant and follows a second-order kinetics.¹⁰

III. Output Spectrum of Input Images

First, consider the case when the object is static, i.e., with no relative motion between the object and sensor. Using Eq. (3), the output spectrum of the static image, where $i(x,y,t) = i(x,y)$, can be expressed as

$$\begin{aligned} G(u,v) &= \int_6 i(x',y')h(x-x',y-y',t-t')dx'dy'dt' \exp[-j2\pi(ux+vy+ft)]dx'dy'dt' \\ &= \int_6 i(x',y')h(x-x',y-y',t-t') \exp[-j2\pi(ux+vy+ft)]dx'dy'dt' \\ &= \int_6 i(x',y')s(x-x',y-y')\Delta(t-t') \exp[-j2\pi(ux+vy+ft)]dx'dy'dt' \\ &= S(u,v)D(f) \int_3 i(x',y') \exp[-j2\pi(ux'+vy'+ft')]dx'dy'dt' \\ &= I(u,v)S(u,v)D(f) \int_1 \exp[-j2\pi(ft')]dt' \\ &= I(u,v)S(u,v)D(f)\delta(f), \end{aligned} \quad (4)$$

For a linear imaging system, the system output is given by the convolution integral

$$g(x,y,t) = \iiint i(x',y',t')h(x-x',y-y',t-t')dx'dy'dt', \quad (1)$$

where $i(x,y,t)$ is an input to the system. The transfer function of the system is, however, given by

$$H(u,v,f) = \iiint h(x,y,t) \exp[-j2\pi(ux+vy+ft)]dx'dy'dt', \quad (2)$$

where u and v are the spatial frequency components, respectively, along the horizontal and vertical directions and f is the temporal frequency. Note that calculation of the overall transfer function is greatly simplified

where the integral sign \int_n denotes an integral of order n , and $I(u,v)$, $S(u,v)$, $D(f)$, and $\delta(f)$ are, respectively, the input spatial spectrum, 2-D static transfer function, dynamic transfer function, and dirac δ -function. Therefore, the output spectrum becomes nonzero only for a dc temporal frequency. In the absence of motion the output spectrum is characterized simply by the static MTF $S(u,v)$ of the imaging system.

When the object is in motion, the input function is given by

$$i(x,y,t) = i(x+mt,y+nt), \quad (5)$$

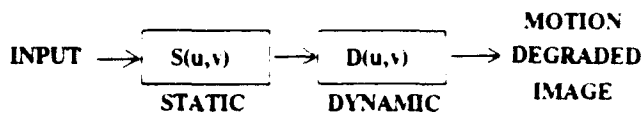


Fig. 3. Overall transfer function.

where for simplicity we have assumed that the velocity is a constant where x - and y -components are m and n , respectively. In case of a nonuniform velocity, the terms mt and nt are replaced by the integrals of velocity components with time. Furthermore, we assume that the energy incident from the moving object is invariant with time. Accordingly, the light emanating from the object (which is a function of both space and time) reduces to a function of space alone.

Using Eqs. (1) and (5), Eq. (4) yields

$$\begin{aligned}
 G(u,v,f) &= \int_{\delta} i(x',y')h(x-x',y-y',t-t')dx'dy'dt' \\
 &\quad \times \exp[-j2\pi(ux+vy+ft)]dx'dy'dt' \\
 &= \int_{\delta} i(x',y')s(x-x',y-y')\Delta(t-t') \\
 &\quad \times \exp[-j2\pi(ux+vy+ft)]dx'dy'dt' \\
 &= I(u,v)S(u,v)D(f)\delta(f-um-vn) \\
 &= I(u,v)S(u,v)D(u,v).
 \end{aligned} \quad (6)$$

The overall transfer function, as shown in Fig. 3, is thus given by

$$H(u,v) = S(u,v)D(u,v), \quad (7)$$

where $D(u,v)$ is the dynamic component of the total MTF $H(u,v)$, referred to as the DMTF. Equation (7) can be used to predict the effect of both velocity and the static transfer function on the quality of the displayed image.

IV. Case Studies of the DMTF

Due to the finite shutter opening time and the relative velocity of the object, for example, the corresponding camera image undergoes a displacement on the film. The effect of such an image motion on the film can be modeled by the dynamic response of the camera. For a camera, the total exposure at any point of the film is obtained simply by integrating the instantaneous exposure over the total exposure time.¹³ Accordingly,

$$g(x,y) = \int_0^T i(x-mt,y-nt)dt, \quad (9)$$

where T is the total duration of the exposure. By taking the Fourier transform of the total response, one obtains

$$\begin{aligned}
 G(u,v) &= \int_{\delta} i(x-mt,y-nt)dt \exp[-j2\pi(ux+vy)]dx'dy' \\
 &= I(u,v) \int_0^T \exp[-j2\pi(umt+vn)t]dt \\
 &= I(u,v) \text{sinc}\{(um+vn)\}.
 \end{aligned} \quad (10)$$

In the case of a camera, therefore, the dynamic part of the DMTF is characterized by a simple 2-D sinc function.

The DMTF can also be calculated from the Fourier transform of the dynamic part of the 3-D impulse response. For the image tube, for example, the point-impulse response is given by Eq. (3). Phosphor decay in the image tube is exponential in nature, and it may even decay with several time constants.¹⁴ Consider a phosphor screen being illuminated with an input for a certain duration, and say at $t = 0$ the illumination is withdrawn. This scenario is analogous to applying a negative step input. By differentiating the negative step response, i.e., the phosphor decay curve, the impulse response of the screen can be obtained as

$$\Delta(t) = -(d/dt)[I_0 \exp(-t/\tau)] = (I_0/\tau) \exp(-t/\tau), \quad (11)$$

where τ is the associated time constant. The dynamic part of the DMTF is obtained as

$$D(f) = (1 + j2\pi f\tau)^{-1}. \quad (12)$$

By replacing the temporal frequency f with $mu + vn$, therefore, the corresponding spatial frequency equivalent can be obtained. The dynamic part of the DMTF can be approximated by an exponential function.

Comparing the DMTFs of the camera and image tube, one notices that the former has several zeros. Due to motion, therefore, some of the frequencies of the information will be totally lost. In the case of the image tube, however, the dynamic part of the DMTF becomes zero only at the highest frequency. Since most of the information is localized within a narrow bandwidth, not much information is lost due to motion. In both cases, however, the modulation loss increases with velocity and duration of exposure. Note that for the case of image tubes, the motion-degraded images are recoverable by means of inverse filters.¹⁵

V. Determination of the DMTF

Studies^{16,17} have successfully shown that the time constant increases with increasing temperature. Important experimental work¹⁴ has already provided a quantitative estimate for the phosphor time constants at various states. From their data, we see (with some modification) that for a type P-20 phosphor, 90% of the phosphorescence has a time constant value of <0.3 s, 8% of the phosphorescence has a time constant value of 5.4 s, and the remaining 2% of the phosphorescence has a time constant value of 50 s. It was also determined that the 10% time constant of phosphor is 0.2 ms with 100% of the phosphors in the same state. For our study, therefore, a reasonable approximation can be made so that 90% of the phosphor is assumed to have a 10% time constant of 0.2 ms. Accordingly, we calculate the DMTF of type P-20 phosphor and compare its performance with that of two slower phosphors P-42 (of a time constant of 10 ms) and P-1052 (of a time constant of 20 ms).^{18,19}

For the type P-20 phosphor based display, one can vectorially add the three MTFs using the three time constants and then determine the MTF by taking the

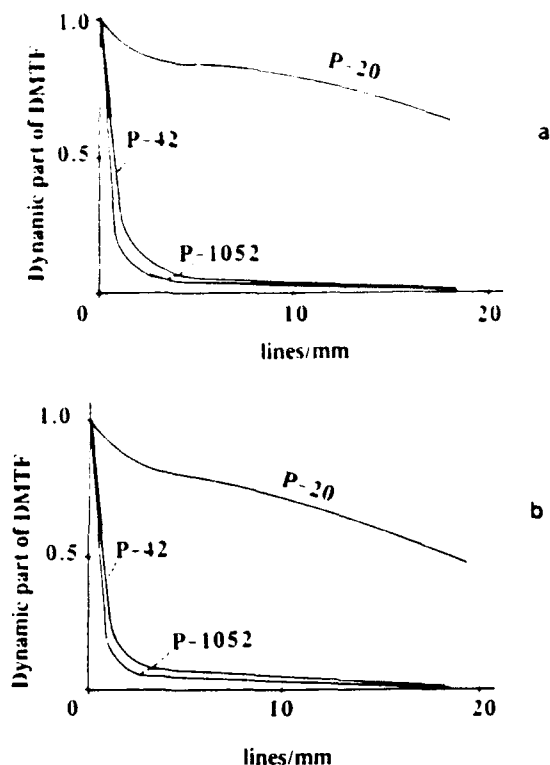


Fig. 4. Dynamic component of the DMTF for a relative motion of (a) 100 and (b) 150 mm/s.

modulus of the resulting function. The dynamic component of the DMTFs for the three phosphors are shown in Figs. 4(a) and (b), respectively, for the relative velocities of 100 and 150 mm/s. It can be seen that the high frequency response corresponding to type P-20 phosphor is significantly more desirable than those corresponding to type P-42 and type P-1052 phosphors. The DMTF degradation is more severe at higher relative velocities. Figure 5, for example,

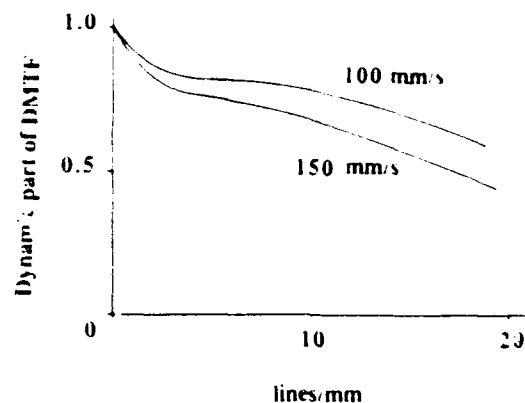


Fig. 5. Dynamic component of the DMTF corresponding to type P-20 phosphor based display for different relative velocities.

shows the dynamic component of the DMTFs for the P-20 phosphor based display for two relative velocities. The attenuation associated with type P-42 and type 1052 phosphors is too high, so the high frequency information content of the corresponding image is totally lost. For the sake of comparison, consider the dynamic component of the DMTF values only at 10 and 15 lines/mm. The bandwidth of the DMTF and 10% cutoff values are tabulated for both P-20 and P-1052 (phosphors with extreme characteristics) in Table I. In displaying dynamic objects, therefore, image tubes based on either types P-42 or P-1052 phosphor will have a poorer performance.

VI. Conclusion

This paper discusses the importance of introducing a dynamic specification for characterizing display systems. We have demonstrated that DMTF can be used to predict correctly the overall image quality. Experimentally obtained data were utilized to calculate and

Table I. Dynamic Components of the DMTFs for P-20 and P-1052 Phosphors

Velocity (cm/sec)	P-20			P-1052		
	10 l/mm	15 l/mm	10% cutoff	10 l/mm	15 l/mm	10% cutoff
10	90%	89%	>20 l/mm	18%	12%	17 l/mm
50	86%	83%	>20 l/mm	4%	2%	4 l/mm
100	79%	75%	>20 l/mm	2%	<1%	2 l/mm
150	70%	58%	>20 l/mm	1%	<1%	1 l/mm

compare dynamic responses of three different types of phosphor coated display screen. The choice of selecting a particular phosphor for a display would directly depend on the relative velocity of the target and sensor. Other types of motion degradation effect, such as those due to vibration,²⁰ can also be incorporated into the DMTF model. After having identified the degradation function quantitatively, it will be possible to generate schemes and/or systems for the restoration of motion-degraded images.^{15,21,22} The DMTF model developed herein may be extended to include the degradation introduced by random noises due to the inhomogeneity of the phosphor distribution.

The authors are grateful for the research support provided in part by the U.S. Army Research Office contract DAAL03-87-K-0121 with the University of Dayton.

A.A.S. Awwal is now with Wright State University, and A. K. Cherri is now with University of Michigan.

References

1. J. D. Gaskill, *Linear Systems, Fourier Transforms, and Optics* (Wiley, New York, 1978).
2. M. V. Klein and T. E. Furtak, *Optics* (Wiley, New York, 1986).
3. C. E. Rash and R. W. Verona, "Temporal Aspects of Electro-Optical Imaging Systems," *Proc. Soc. Photo-Opt. Instrum. Eng.* **765**, 22-24 (1987).
4. R. M. Clodfelter, "Modulation Transfer Function for the Display Engineer," *Proc. Soc. Photo-Opt. Instrum. Eng.* **624**, 113-118 (1986).
5. R. M. Simonds, "Two-Dimensional Modulation Transfer Functions of Image-Scanning Systems," *Appl. Opt.* **20**, 619-622 (1981).
6. D. Hearn and M. P. Baker, *Computer Graphics* (Prentice-Hall, Englewood Cliffs, NJ, 1986).
7. M. A. Karim, *Electro-Optical Devices and Systems* (PWS-Kent, Boston, 1990).
8. T. L. Williams, "Modulation Transfer Function (MTF) System for Image Intensifier Units," *Proc. Soc. Photo-Opt. Instrum. Eng.* **274**, 148-153 (1981).
9. L. Levi, "On Combined Spatial and Temporal Characteristics of Optical Systems," *Opt. Acta* **17**, 869-872 (1970).
10. L. Levi, "Spatiotemporal Transfer Function: Recent Developments," *Appl. Opt.* **22**, 4038-4041 (1983).
11. J. Wilson and J. F. B. Hawkes, *Optoelectronics: an Introduction* (Prentice-Hall, Englewood Cliffs, NJ, 1983).
12. X. Shi-ming, "MTF Deterioration by Image Motion in Electro-Optical Imaging System," in *Proceedings, Electro-Optics/Laser International UK Conference*, Brighton (Mar. 1982), pp. 62-73.
13. A. Rosenfeld and A. C. Kak, *Digital Picture Processing, Vol. 1* (Academic, New York, 1982).
14. B. R. Sandel, D. F. Collins, and A. L. Broadfoot, "Effect of Phosphor Persistence on Photometry with Image Intensifiers and Integrating Readout Devices," *Appl. Opt.* **25**, 3967-3704 (1986).
15. A. K. Cherri, A. A. S. Awwal, M. A. Karim, and D. L. Moon, "Restoration of Motion Degraded Images in Electro-Optical Displays," *Proc. Soc. Photo-Opt. Instrum. Eng.* **1116**, 198-208 (1989).
16. M. R. Torr, "Persistence of Phosphor Glow in Microchannel Plate Image Intensifiers," *Appl. Opt.* **24**, 793-795 (1985).
17. J. E. Horn and M. J. McCutcheon, "Decay Time of Some Image Tube Phosphors as a Function of Excitation Time," *Proc. IEEE* **58**, 592-593 (1970).
18. I. P. Csorba, "Image Intensifiers in Low Light Level and High Speed Imaging," in *Electronic Imaging '86*, Boston, 3-6 Nov. 1986.
19. I. P. Csorba, *Image Tubes* (Howard W. Sams, Indianapolis, 1985).
20. D. Wulich and N. S. Kopeika, "Image Resolution Limits Resulting from Mechanical Vibrations," *Opt. Eng.* **26**, 529-533 (1987).
21. B. Javidi, H. J. Caulfield, and J. L. Horner, "Real-Time Deconvolution by Nonlinear Image Processing," *OSA Annual Meeting, 1988 Technical Digest Series, Vol. 11* (Optical Society of America, Washington, DC, 1988), p. 9.
22. F. Vachss and L. Hesselink, "Synthesis of a Holographic Image Velocity Filter Using the Nonlinear Photorefractive Effect," *Appl. Opt.* **27**, 2887-2894 (1988).

Restoration of moving binary images degraded owing to phosphor persistence

A. K. Cherri, A. A. S. Awwal, M. A. Karim, and D. L. Moon

The degraded images of dynamic objects obtained by using a phosphor-based electro-optical display are analyzed in terms of dynamic modulation transfer function (DMTF) and temporal characteristics of the display system. The direct correspondence between the DMTF and image smear is used in developing real-time techniques for the restoration of degraded images.

I. Introduction

Imaging systems, in general, and displays, in particular, are evaluated in a static mode. For many of the imaging applications, the temporal characteristics of the imaging system may not be critical. In dynamic environments, however, the temporal response of an imaging system plays a more important role than the static response in determining the quality of the display. The absence of temporal response considerations in the analysis of a traditional imaging system, in situations such as driving and pilotage tasks, fails to explain the cause of degradation of the modulation contrast. This degradation becomes more significant at higher spatial frequencies. In such situations, for example, targets begin to blend with the background, and the user loses the ability to discriminate between the two. To characterize fully an electro-optical imaging system, therefore, requires that both static and dynamic aspects be considered.

It has already been shown that phosphor persistence affects the temporal response of a cathode-ray-tube display.^{1,2} In a dynamic environment where there is a relative motion between the target and the sensor, longer persistence value reduces the modulation contrast and eventually causes the loss of gray

levels. Often the loss of one gray level at a high spatial frequency may be significant, for example, where there is only enough modulation contrast to provide one or two gray levels in a static environment. In a more recent work³ we established an analytical formulation of the dynamic modulation transfer function (DMTF) for a nonscanning display system. In particular, for a phosphor-based display system the DMTF has been shown to be a product of the classical modulation transfer function and a dynamic function dependent on phosphor persistence and object motion.

In this paper we demonstrate that the smearing of a displayed image may be properly quantified by considering the temporal response in the imaging system analysis. Also, we show that the phosphor type as well as the value of the relative motion between the target and the sensor plays a significant role in image degradation. Following the identification of proper degradation function, real-time techniques are proposed for the restoration of motion-degraded images. Note that related work on the restoration of images degraded by linear smear such as that in photographic films has already been done.⁴

A. K. Cherri is with the Department of Electrical and Computer Engineering, University of Michigan, Dearborn, Michigan 48128-1491. A. A. S. Awwal is with the Department of Computer Science and Engineering, Wright State University, 3171 Research Boulevard, Kettering, Ohio 45420. M. A. Karim and D. L. Moon are with the Center for Electro-Optics and Department of Electrical Engineering, The University of Dayton, 300 College Park Avenue, Dayton, Ohio 45469-0226.

Received 19 October 1990.

0003-6935/91/263734-06\$05.00/0.

© 1991 Optical Society of America.

II. Dynamic Modulation Transfer Function Review

Figure 1 is a block diagram of an imaging system where an input object $i(x, y, t)$ is operated on by the point-impulse function³ $h(x, y, t)$ to produce an output image $g(x, y, t)$. Provided that the point-impulse response function $h(x, y, t)$ can be expressed as a product of a purely spatial function $s(x, y)$ and a purely temporal function $\Delta(t)$, such as

$$h(x, y, t) = s(x, y)\Delta(t), \quad (1)$$

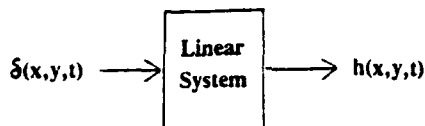


Fig. 1. Block diagram of an electro-optical imaging system.

one may evaluate³ the Fourier transform of $g(x, y, t)$ as

$$G(u, v, f) = D(f)S(u, v)I(u, v)\delta(f - um - vn), \quad (2)$$

where m and n denote velocity components along the x and y directions, respectively; u and v represent the spatial frequencies along the x and y directions, respectively; f is the temporal frequency, and $D(f)$, $S(u, v)$, and $I(u, v)$ are the dynamic transfer function, the static transfer function, and the spectrum of the static image, respectively. The presence of the factor $\delta(f - um - vn)$ implies that, during the evaluation of $G(u, v, f)$, the variable f in $D(f)$ needs to be replaced with $um + vn$. The overall system block diagram of the electro-optical display that is shown in Fig. 2 includes both static and dynamic transfer functions. The product $D(f)S(u, v)\delta(f - um - vn)$ is referred to as the DMTF. This new form for the spatiotemporal transfer function of the imaging system can be used to characterize the motion-degraded images. It is important to understand that Eq. (2) is correct as long as the separability condition of Eq. (1) is valid. Fortunately, this separability condition remains valid³ as long as phosphor-based electro-optical display systems are considered.

III. Decay Constants and Spatial Speed Considerations

A well-known phosphor screen characteristic is provided by its exponential decay behavior, which can be approximated by⁵

$$\Delta(t) = A_1 \exp(-t/\tau_1) + A_2 \exp(-t/\tau_2) + A_3 \exp(-t/\tau_3) + \dots \quad (3)$$

where A_i is a factor representing the proportion of the phosphor in the i th state and τ_i is the corresponding time constant, defined as the duration during which the phosphorescence decays to $1/e$ th of its maximum value A_i . In general, the last two terms of Eq. (3) represent fluorescence modes of a phosphor light output. When compared with the first term, representing the phosphorescence mode of light output, the contributions of the last two terms are insignificant.⁵ Accordingly, Eq. (2) may be approximated by

$$\Delta(t) = \tau^{-1} \exp(-t/\tau), \quad (4)$$

where, for simplicity, A_i is set equal to $1/\tau$. Taking the Fourier transform of Eq. (4), we obtain the dynamic

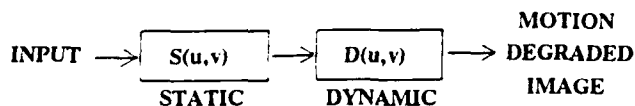


Fig. 2. DMTF of an electro-optical display.

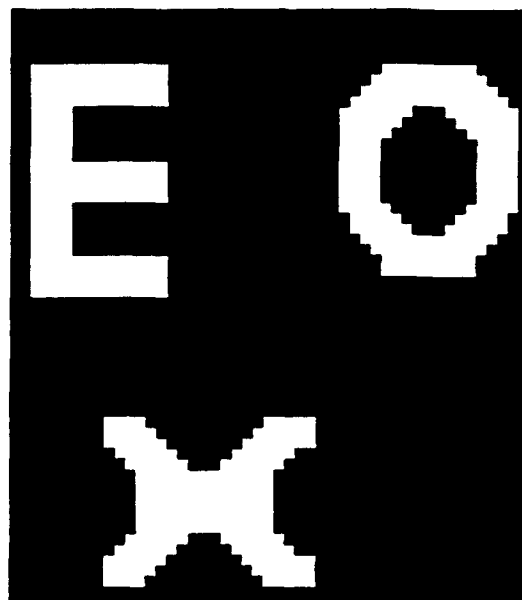


Fig. 3. 64 × 64 input binary image.

component of the DMTF for the phosphor screen as

$$D(f) = (1 + j2\pi f\tau)^{-1}. \quad (5)$$

Equation (5), representing the temporal transfer function of a phosphor screen, can be introduced in Eq. (2) to predict the overall degradation of motion-involved displayed images. However, to use $D(f)$, one must estimate the specific value of the time constant of the phosphor used in the electro-optical display under consideration. One may use the fact that the type P-1052 phosphor, for example, takes 20 ms to decay to 10% of its maximum value.⁶ Accordingly, we may set $\tau = 8.68$ ms for the case of type P-1052 phosphor.

To predict the effect of the temporal response, in accordance with Eq. (5) one must convert the temporal information into a spatial format. This is done by simply replacing f with $um + vn$. However, an object can move in any one of the following ways:

1. Motion in the x direction only when f can be set equal to um .
2. Motion in the y direction only when f can be set equal to vn .
3. Motion in the x - y plane making an arbitrary angle θ with the x axis, in which case f is set equal to $um + vn$, provided that $m = v \cos \theta$ and $n = v \sin \theta$, where v represents the velocity.
4. Motion in the z direction only, in which case f is set equal to wp , where p is speed in the z direction and w is the corresponding radial frequency component.
5. Arbitrary motion in x - y - z space.

IV. Simulation of Image Degradation

To comprehend the extent of image degradation in an electro-optical display, we consider a particular image intensifier tube, such as that used in night vision

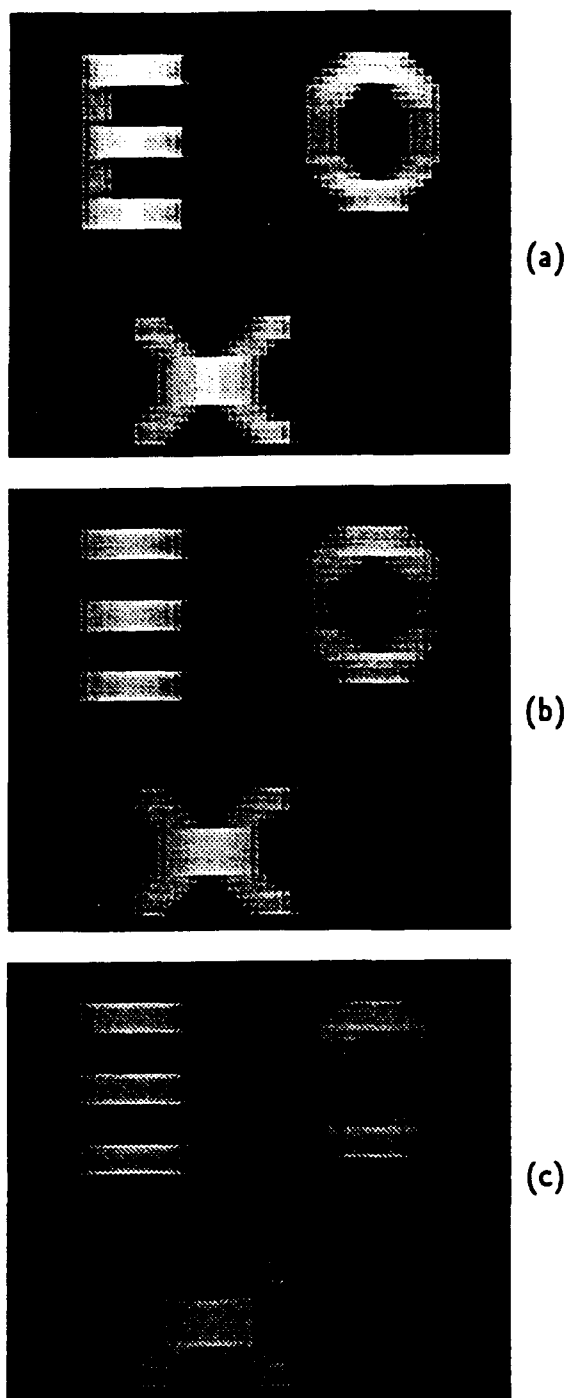


Fig. 4. Images degraded as a result of horizontal speeds of (a) 4 cm/s, (b) 8 cm/s, and (c) 15 cm/s.

goggles. In this application it is estimated that the maximum angular movement of the head (with the goggles) is $120^\circ/\text{s}$.⁷ By assuming that the distance between the phosphor screen and the object lens is 7.62 cm, for example, we calculate the spatial speed m to be $(120^\circ/180^\circ) 7.62 \text{ cm} = 15.958 \text{ cm/s}$.

The calculated value of m and the experimentally determined value for the time constant of type P-1052 phosphor, for example, is used in Eq. (5) to calculate the corresponding modulation transfer function of the dynamic response. A computer program may be

used to simulate the effect of the DMTF on images. The simulation algorithm involves the following steps:

1. Obtain the fast Fourier transform (FFT) of the static image.
2. Obtain the FFT of $\Delta(t)$ for a particular motion.
3. Multiply (point by point) the FFT's obtained in steps 1 and 2.
4. Take the inverse FFT of the product to estimate degradation.

A 64×64 pixel-sized binary image, as shown in Fig. 3, is used as the input image in the simulation. Figures 4(a), 4(b), and 4(c) show the corresponding degraded images when head movement along the x direction approaches speeds of 4, 8, and 15 cm/s, respectively. It is evident that with increasing speed the image degrades more and more. Since motion is

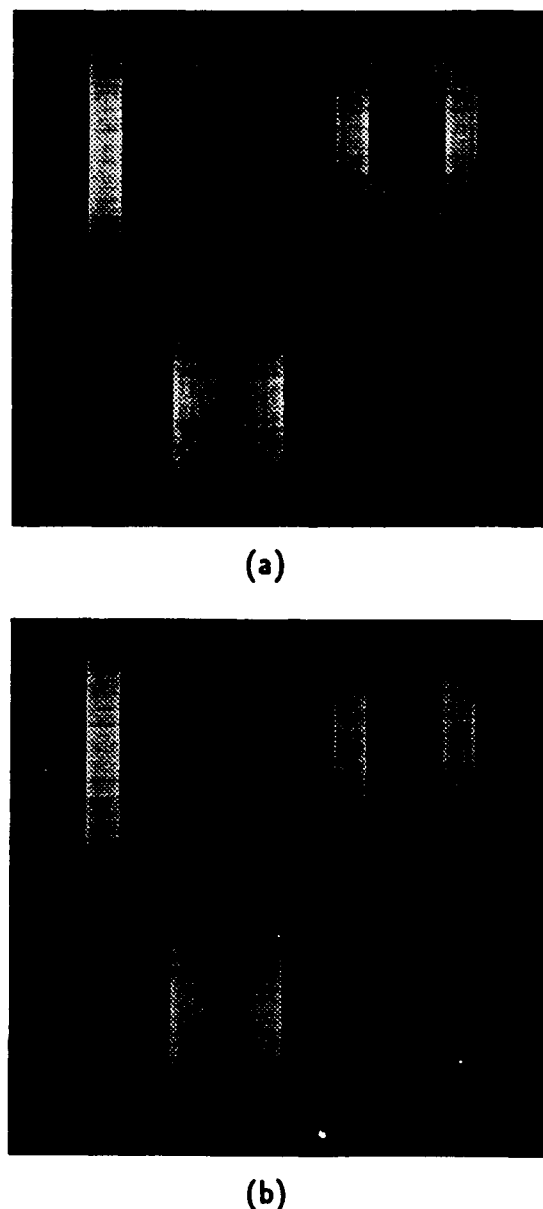
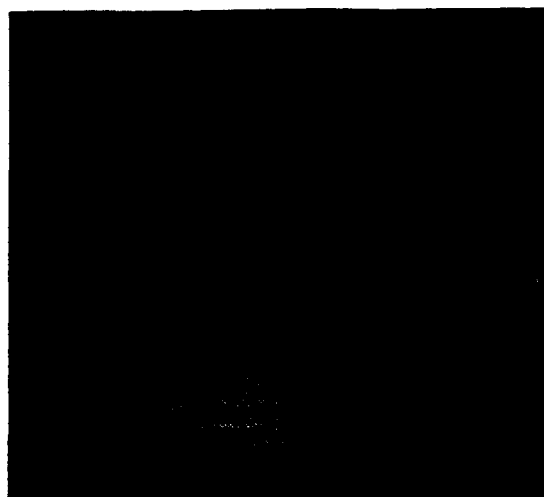
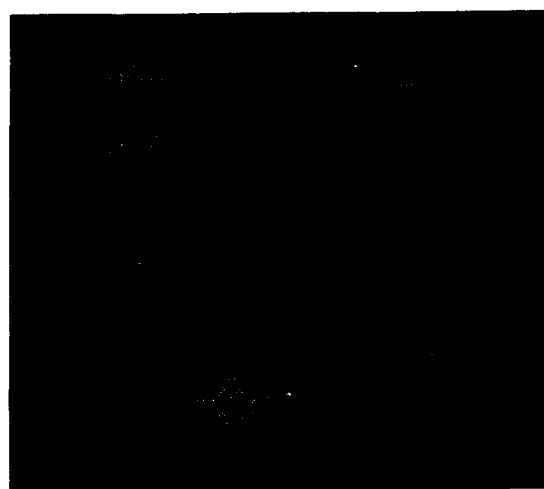


Fig. 5. Images degraded because of vertical speeds of (a) 10 cm/s, (b) 15 cm/s.



(a)



(b)

Fig. 6. Images degraded by motion along (a) 45° with 10 cm/s, and (b) 20° with 15 cm/s.

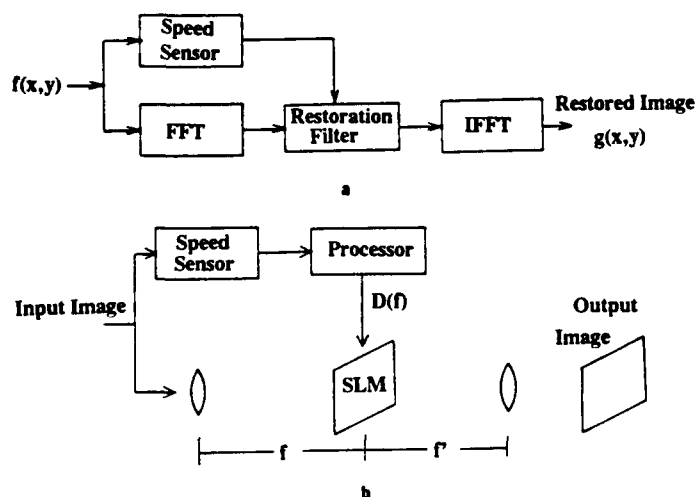


Fig. 7. Adaptive restoration: (a) model; (b) system.

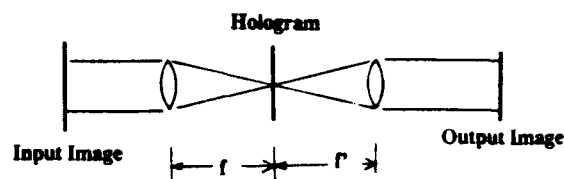
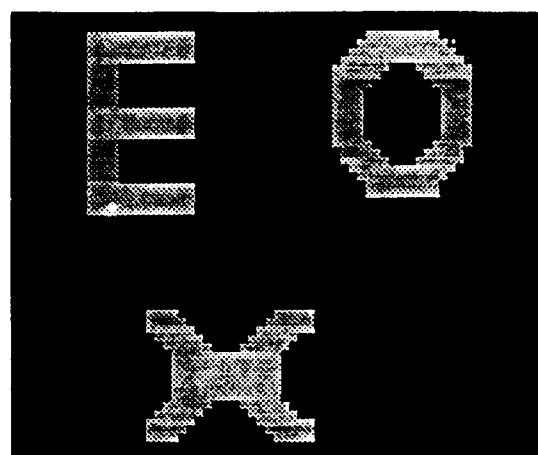


Fig. 8. Nonadaptive restoration with a Fourier hologram used as an inverse filter.

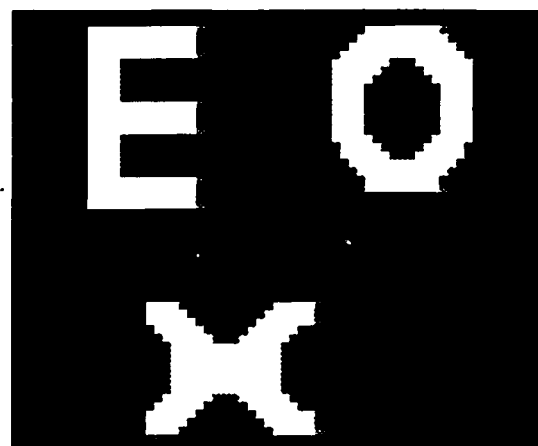
directed only along the x axis, the degradation of vertical edges becomes more significant. For comparison, Figs. 5(a) and 5(b) show motion-degraded images for an object moving in the y axis at spatial speeds of 10 and 15 cm/s, respectively; note that in these cases the horizontal edges are the most effected. Finally, Figs. 6(a) and 6(b) show motion-degraded images for the case of a motion directed at angles of 45° and 20° to the x axis at speeds of 10 and 15 cm/s, respectively. In Figs. 6(a) and 6(b), however, one finds that both horizontal and vertical edges have been degraded.

V. Simulation of Image Restoration

In Section IV we showed that the DMTF can degrade input images (in the absence of noise, for simplicity)



(a)



(b)

Fig. 9. Image of Fig. 4(c) restored by using inverse filters corresponding to (a) 12 cm/s, (b) 7 cm/s.

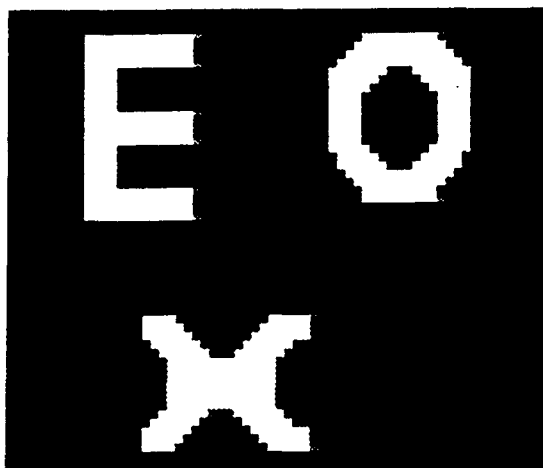
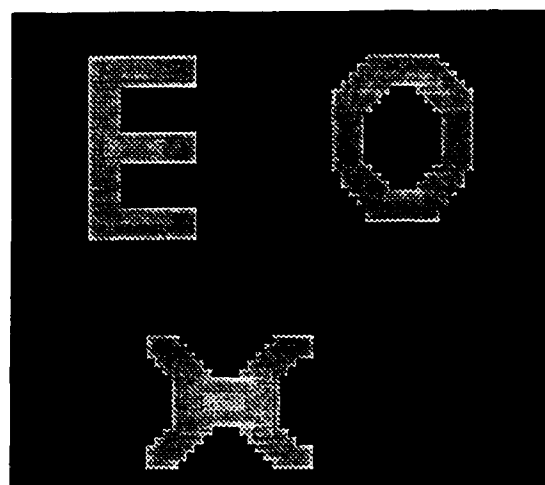
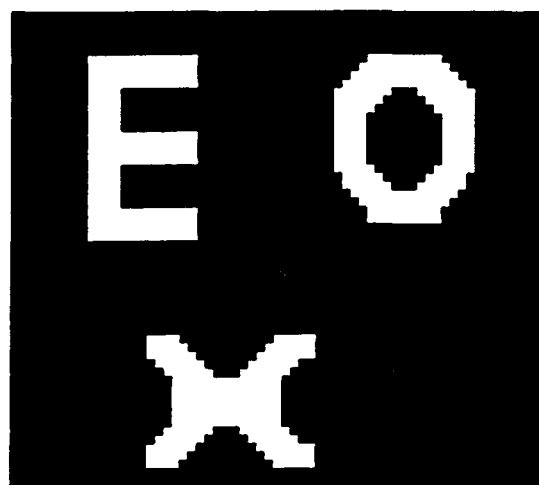


Fig. 10. Image degraded by a horizontal speed of 5 cm/s restored by using an inverse filter corresponding to a horizontal speed of 10 cm/s.

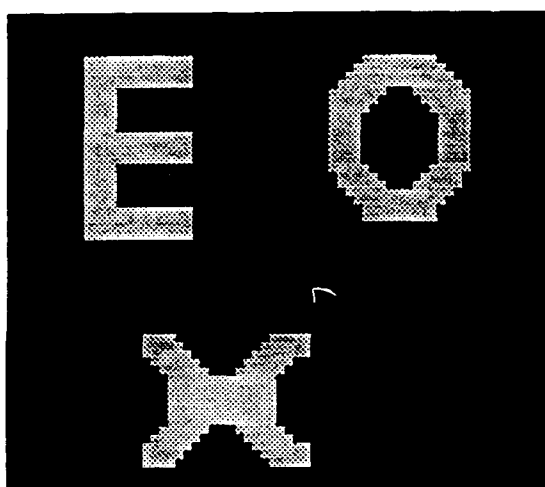
to a degree that the object is hardly recognizable. To restore the degraded images consider the degradation model shown in Fig. 2. In this model, the object image $i(x, y, t)$ is operated on by a degradation function $H(u, v, f)$, which produces a degraded output image $g(x, y, t)$. Our main objective is to obtain an approximation of $i(x, y, t)$ given $g(x, y, t)$ and some knowledge of the degradation function $H(u, v, f)$. However, the degradation function as given by Eq. (2) consists of two separable functions, $S(u, v)$ and $D(f)$, where $S(u, v)$ is a purely static (spatial) function and $D(f)$ is a purely dynamic (temporal) function. Therefore, by eliminating the effects of $D(f)$, one can obtain a reasonably good displayed image. This is accomplished by simply dividing $H(u, v, f)$ by $D(f)$. Such a restoration technique, based on the concept of inverse filtering, can be applied in a straightforward fashion



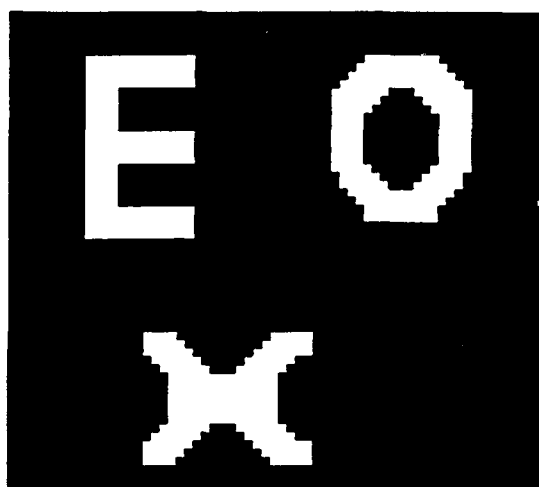
(a)



(c)



(b)



(d)

Fig. 11. Image degraded by a motion of 10 cm/s at an angle of 30° restored by using filters corresponding to (a) 6 cm/s, (b) 8 cm/s, (c) 10 cm/s, (d) 12 cm/s.

since the modulus of $D(f)$ is not zero except at infinity. If this were not true, such a condition would have posed a major restriction on inverse filtering. The stimulation of the restoration process is summarized as follows:

1. A FFT of the degraded image $g(x, y)$ is obtained. This gives $S(u, v)D(f)$.
2. Given the object's velocity and direction, the corresponding inverse filter, i.e., $[D(f)]^{-1}$ is calculated.
3. The results obtained in steps 1 and 2 are multiplied (point by point) in the frequency domain.
4. An inverse FFT of the result of step 3 yields the restored image.

To restore the degraded image one needs to know the type of phosphor and hence the corresponding time constant(s) and the value and the direction of the relative motion between the sensor and the target. One needs this information to realize $[D(f)]^{-1}$, as discussed above. While there is no problem in meeting the first requirement, often it may be difficult to estimate exactly the value of the relative motion.

The real-time restoration model is shown in Fig. 7(a). In this model both the magnitude and the direction of the relative motion are determined first. This information is used in the design of the restoration filter. A simple hybrid setup to perform the restoration process is illustrated in Fig. 7(b), which shows that a spatial light modulator can be used to imprint the inverse filter. Note that this real-time restoration model is suitable for applications in which both the speed and the direction of the relative motion can be reasonably estimated.

For applications for which the relative motion between the target and the sensor is not known exactly, a simpler restoration model like the one shown in Fig. 8 can be used. In this simple system a fixed Fourier hologram may be used to store the inverse filter (for a single specific speed or a range of speeds). The image of Fig. 4(c), for example, may be restored to some degree as in Fig. 9(a), by using an inverse filter designed for a speed value of 12 cm/s, or as in Fig. 9(b) by using an inverse filter designed for a speed of 7 cm/s. Similarly, Fig. 10 shows a restoration of a motion-degraded image that is due to horizontal motion of 5 cm/s when the image is subjected to a restoration filter designed for a speed of 10 cm/s. Figure 11 shows restoration of images moving with a velocity of 10 cm/s at an angle of 30° . Figures 11(a), 11(b), 11(c), and 11(d) show the images restored by using filters corresponding to 6, 8, 10, and 12 cm/s, respectively. The restored images show a great improvement since they are now similar to the original image. Observations suggest that it is not always necessary to know the exact value of the relative velocity. A value close to the relative speed of the

target is more likely to provide a better output image of an electro-optical display than one that uses no restoration filter. It is worth mentioning that a high-frequency filter may also be used as a restoration filter since the degradation function behaves as a low-pass filter.^{8,9}

VI. Summary

In this paper we have used the dynamic transfer function to predict the image quality and the performance of a phosphor-based electro-optical display. By incorporating the concept of temporal response that is otherwise missing from traditional imaging systems analysis, we can quantify degradation of the output image of an electro-optical display. This quantification can be used successfully to propose efficient and real-time techniques for restoration of motion-degraded images. We have also shown that for the restoration of motion-degraded displayed images it is only necessary to have a reasonable knowledge of relative velocity. Work is currently in progress to identify a single optimum inverse filter as well as an optimum composite inverse filter for restoration applications.

The authors acknowledge the partial research support provided by the U.S. Army Research Office under contract DAAL03-87-K-0121 with the University of Dayton.

References

1. R. W. Verona, H. L. Task, V. Arnold, and J. H. Brindle, "A Direct Measure of CRT Image Quality," USAARL Rep. 79-14 (U.S. Army Aeromedical Research Laboratory, Fort Rucker, Ala., 1979).
2. C. E. Rash and J. Becker, "Analysis of Image Smear in CRT Displays Due to Scan Rate and Phosphor Persistence," USAARL Rep. 83-5 (U.S. Army Aeromedical Research Laboratory, Fort Rucker, Ala., 1982).
3. A. A. S. Awwal, A. K. Cherri, M. A. Karim, and D. L. Moon, "Dynamic modulation transfer function of a display system," *Appl. Opt.* **30**, 201-205 (1991).
4. L. Celaya, and S. Mallick, "Incoherent processor for restoring images degraded by a linear smear," *Appl. Opt.* **17**, 2191-2194 (1978).
5. B. R. Sandel, D. F. Collins, and A. L. Broadfoot, "Effect of phosphor persistence on photometry with image intensifiers and integrating readout devices," *Appl. Opt.* **25**, 3697-3704 (1986).
6. I. P. Csorba, "Image intensifiers in low light level and high speed imaging," presented at Electronic Imaging '86 Meeting, Boston, Mass., 3-6 November 1986.
7. R. W. Verona, Night Vision Laboratory, Fort Belvoir, Va. (personal communication).
8. B. Javidi, H. J. Caulfield, and J. L. Horner, "Real-time deconvolution by nonlinear image processing," in *1989 Annual Meeting of Optical Society of America*, Vol. 18 of 1989 OSA Technical Digest Series (Optical Society of America, Washington, D.C., 1989), p. 89.
9. F. Vachss and L. Hesselink, "Synthesis of a holographic image velocity filter using the nonlinear photorefractive effect," *Appl. Opt.* **27**, 2887-2894 (1988).

Device nonspecific dynamic performance model for thermal imaging systems

Ming L. Gao

Mohammad A. Karim, MEMBER SPIE

Song H. Zheng

University of Dayton

Center for Electro-Optics
and

Electrical Engineering Department

300 College Park Avenue

Dayton, Ohio 45469-0227

Abstract. A device nonspecific dynamic minimum resolvable temperature difference performance model is developed for characterizing thermal imaging systems capable of displaying moving targets.

Subject terms: infrared imaging systems; dynamic minimum resolvable temperature difference; impulse responses; phosphors.

Optical Engineering 30(11), 1779-1783 (November 1991).

CONTENTS

1. Introduction
2. DMTF review
3. DMTF test system
4. DMRTD development
5. Simulation results
6. Conclusion
7. Acknowledgment
8. References

1. INTRODUCTION

The available performance models¹ for characterizing thermal imaging systems capable of displaying static targets include modulation transfer function (MTF), minimum resolvable temperature difference (MRTD), noise equivalent temperature difference, and minimum detectable temperature difference. Of these four, MTF and MRTD are used most widely. While MTF indicates the transfer performance of thermal imaging systems without having considered the effect of noise, MRTD is a minimum resolution index measure evaluated in the presence of noise.

Static performances provide a good understanding of the actual system behavior; however, too many imaging systems monitor moving scenes or targets. In such situations, the overall imaging system behavior is often affected by the temporal performances²⁻⁴ of some of the detectors. Thus, to characterize accurately the capabilities of thermal imaging systems, identifying an appropriate dynamic measure is essential. Two recent works^{3,5} have introduced the concepts of dynamic optical transfer function (DOTF) and dynamic MTF (DMTF), respectively, for describing non-scanning imaging systems. More recently, we have developed a device-nonspecific generalized static model for the MRTD measure.⁶ In our current effort, we extend the scope of these earlier works^{5,6} and develop a device-nonspecific dynamic MRTD (DMRTD) measure to serve as a dynamic performance model for thermal imaging systems.

Invited paper IR-010 received March 25, 1991; revised manuscript received July 9, 1991; accepted for publication July 10, 1991.
© 1991 Society of Photo-Optical Instrumentation Engineers.

In general, the parameter DMRTD is expected to be three-dimensional: two dimensions in the space domain and one dimension in the time domain. In this paper, we show that under suitable conditions the three-dimensional DMRTD can be reduced to only spatial dimensions. Reference 3 describes an experimental setup for determining DMTF. The test system requires a light source capable of flashing for an infinitesimal time interval; however, such ideal sources are nonexistent. Therefore, any DMTF obtained using any realistic experimental system is not necessarily accurate. In this paper, an alternate method that does not require a flashing thermal source is introduced for testing DMTF and DMRTD of an electro-optical system.

2. DMTF REVIEW

In the static mode, a spatial impulse response is used for characterizing the spatial performance of any arbitrary optical system. The impulse response, $h_s(x,y)$, is the output of the system when the system input is a spatial Dirac delta function, $\delta(x,y)$. The Fourier transform, $H_s(f_x, f_y)$, of $h_s(x,y)$ is referred to as the optical transfer function of the system. Similarly, the temporal performances of the system under question may be characterized by a temporal impulse response, $h_t(t)$, whose Fourier transform, $H_t(f_t)$, may be referred to as the system's temporal transfer function. Accordingly, the overall output of the system may be given by a spatiotemporal impulse response, $h(x,y,t)$, whose Fourier transform, $H(f_x, f_y, f_t)$, is the DOTF of the system. The modulus of this DOTF is the DMTF.⁵

It can be shown that when the system responses are separable, i.e., when

$$h(x,y,t) = h_s(x,y)h_t(t) \quad (1)$$

the DMTF of the system is given by⁵

$$H(f_x, f_y, f_t) = H_s(f_x, f_y)H_t(f_t) \quad (2)$$

Consider now a moving input object described by $g_1(x,y,t) = \delta(x + v_0 t, y)$, such that its spatial and temporal responses are separable. This input function g_1 corresponds to a

point light source moving along the x -direction with a velocity of v_0 . The corresponding output image $g_2(x, y, t)$ is obtained as

$$g_2(x, y, t) = g_1(x, y, t) * h(x, y, t) \\ = \delta(x + v_0 t, y) * [h_s(x, y)h_t(t)] \quad (3)$$

where $*$ is the convolution operation. The Fourier spectrum $G_2(f_x, f_y, f_t)$ of $g_2(x, y, t)$ is found to yield

$$G_2(f_x, f_y, f_t) \\ = \int_3 \delta(x + v_0 t, y) * [h_s(x, y)h_t(t)] \\ \times \exp[-2\pi j(f_x x + f_y y + f_t t)] dx dy dt \\ = \int_6 \delta(x' + v_0 t', y') h_s(x - x', y - y') h_t(t - t') \\ \times \exp[-2\pi j(f_x x + f_y y + f_t t)] dx' dy' dt' dx dy dt \\ = \int_3 [\int_3 h_s(x - x') h_t(t - t') \exp[-2\pi j(f_x x + f_y y + f_t t)] dx dy dt] \\ \times \delta(x' + v_0 t', y') dx' dy' dt' \\ = H_s(f_x, f_y) H_t(f_t) \int_3 \delta(x' + v_0 t', y') \\ \times \exp[-2\pi j(f_x x' + f_y y' + f_t t')] dx' dy' dt' \\ = H_s(f_x, f_y) H_t(f_t) \int \exp[-2\pi j(f_x v_0 t')] \\ \times \exp[-2\pi j f_t t'] dt' \\ = H_s(f_x, f_y) H_t(f_t) \delta(f_t - v_0 f_x) \quad (4)$$

where \int_n is an integral of order n . But since it can be shown that⁷

$$f(t)\delta(t - t_1) = f(t_1)\delta(t - t_1) \quad (5)$$

therefore,

$$G_2(f_x, f_y, f_t) = H_s(f_x, f_y) H_t(v_0 f_x) \delta(f_t - v_0 f_x) \quad (6)$$

Correspondingly, however, the Fourier transform of $g_1(x, y, t)$ is given by

$$G_1(f_x, f_y, f_t) = \int_3 \delta(x + v_0 t, y) \exp[-2\pi j(f_x x + f_y y + f_t t)] \\ \times dx dy dt \\ = \int \exp(2\pi j f_x v_0 t) \exp(-2\pi j f_t t) dt \\ = \delta(f_t - v_0 f_x) \quad (7)$$

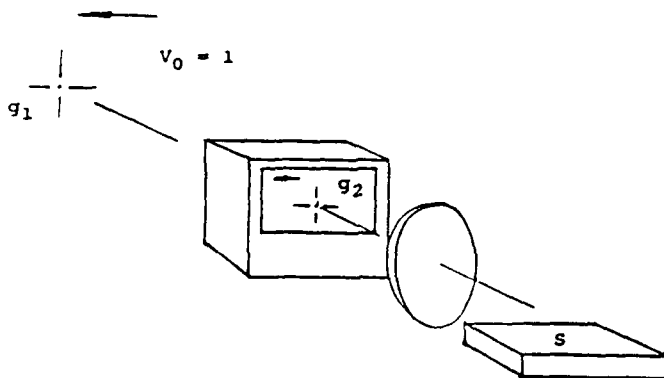


Fig. 1. The experimental setup for evaluating DMRTD.

Therefore, the overall transfer function for the system is given by

$$H(f_x, f_y, f_t) = G_2(f_x, f_y, f_t) / G_1(f_x, f_y, f_t) \\ = H_s(f_x, f_y) H_t(v_0 f_x) \quad (8)$$

When v_0 is unity, for simplicity, Eq. (8) reduces to

$$H(f_x, f_y, f_t) = H_s(f_x, f_y) H_t(f_x) \quad (9)$$

which readily corresponds to the DOTF or DMTF of the system under question and is a function of only spatial variables.

3. DMTF TEST SYSTEM

Identifying the temporal delta thermal source for the testing of thermal imaging systems is difficult. This often implies that we need to secure a heating source with zero heating capacity that may give out energy in an infinitesimal time interval. Instead, we consider a test system, shown in Fig. 1, where g_1 is a point source moving with unit velocity v_0 along the x -direction and g_2 is the corresponding image on the display screen of the system. The sensor array, S , measures the intensity distribution on the screen. When the point image picks up velocity, say, along the x -axis, the image will appear blurred because of the effect of phosphor decay.⁸ An example of the x -dependent intensity profile of the display as detected by the sensor array is shown in Fig. 2(a). This intensity distribution is moving along the x -direction. By having chosen the proper moving coordinate axis, the intensity distribution may appear stationary like that shown in Fig. 2(b). Thus, Fig. 2(b) may be considered as the temporal impulse response of the system, provided the x -axis has been changed to a time axis.

4. DMRTD DEVELOPMENT

The quality of a thermal imaging system depends not only on spatial performances, but also on temporal performance. For

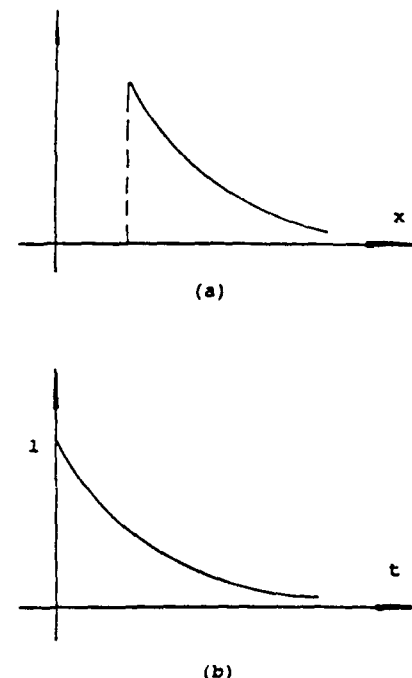


Fig. 2. (a) The intensity distribution on the display and (b) the temporal impulse response of the system.

example, when a four-bar pattern,⁶ which is used for testing MRTD, is stationary, we may recognize the pattern on the screen; however, if the same pattern were to move, the corresponding image on the phosphor-based screen may appear blurred and we might need a higher target temperature for preserving the same level of recognition. Reference 6 already summarizes a device-nonspecific static MRTD formulation based on the linear system theory. Following an identical line of argument, we now combine both space and time parameters to develop the DMRTD.

For uniformity with the traditional MRTD test, a flashing four-bar pattern may be used for testing the temporal impulse response of the to-be-tested IR system. However, we prefer to choose a spatial method for determining the DMRTD similar to that used in the evaluation of DMTF. Assume that the four-bar pattern given by $h_0(x + v_0 t, y)$ is moving with a velocity of v_0 along the x -direction. Assume further that the to-be-tested IR system's spatiotemporal response, $h_{ir}(x, y, t)$, is separable as $h_{ir,s}(x, y)h_{ir,t}(t)$ while at the same time the human eye-brain spatiotemporal response, $h_{mf}(x, y, t)$, is also assumed separable, such that $h_{mf}(x, y, t) = h_{mf,s}(x, y)h_{mf,t}(t)$, where the additional subscripts s and t , respectively, refer to spatial and temporal components. Accordingly, the Fourier transform of the perceived pattern is given by

$$\begin{aligned} G_2(f_x, f_y, f_t) &= \int_3 g_1(x, y, t) * [h_{ir}(x, y, t)h_{mf}(x, y, t)] \\ &\quad \times \exp[-j2\pi(f_x x + f_y y + f_t t)] dx dy dt \\ &= \int_3 \Delta T h_0(x + v_0 t, y) * [h_{ir}(x, y, t)h_{mf}(x, y, t)] \\ &\quad \times \exp[-j2\pi(f_x x + f_y y + f_t t)] dx dy dt \\ &= \Delta T H_0(f_x, f_y) H_{ir,s}(f_x, f_y) H_{mf,s}(f_x, f_y) \\ &\quad \times H_{ir,t}(f_t) H_{mf,t}(f_t) \delta(f_t - v_0 f_x) \end{aligned} \quad (10)$$

The perceived signal is now found to be

$$\begin{aligned} s_p &= \iiint G_2(f_x, f_y, f_t) df_x df_y df_t \\ &= \Delta T \iiint H_0(f_x, f_y) H_{ir,s}(f_x, f_y) H_{mf,s}(f_x, f_y) \\ &\quad \times H_{ir,t}(f_t) H_{mf,t}(f_t) \delta(f_t - v_0 f_x) df_x df_y df_t \\ &= \Delta T \iint H_0(f_x, f_y) H_{ir,s}(f_x, f_y) H_{mf,s}(f_x, f_y) H_{ir,t}(v_0 f_x) \\ &\quad \times H_{mf,t}(v_0 f_x) df_x df_y \\ &= \Delta T \iint H_0(f_x, f_y) H_{ir,s}(f_x, f_y) H_{mf,s}(f_x, f_y) H_{ir,t}(f_x) \\ &\quad \times H_{mf,t}(f_x) df_x df_y \end{aligned} \quad (11)$$

when v_0 is unity. Further, for simplicity, we may assume that the input noise distribution is given by $w(x + v_0 t, y)$. By following identical steps as those used in the derivation of s_p , the perceived noise is found to be

$$\begin{aligned} n_p &= [\iint W(f_x, f_y) H_{ir,s}(f_x, f_y)^2 H_{mf,s}(f_x, f_y)^2 H_{ir,t}(f_x)^2 \\ &\quad \times H_{mf,t}(f_x)^2 df_x df_y]^{1/2} \end{aligned} \quad (12)$$

Using Eqs. (11) and (12), SNR may be obtained as

$$\text{SNR} = \frac{s_p}{n_p} = \frac{\Delta T \iint H_0 H_{ir,s} H_{mf,s} H_{ir,t}(f_x) H_{mf,t}(f_x) df_x df_y}{[\iint W H_{ir,s}^2 H_{mf,s}^2 H_{ir,t}(f_x) H_{mf,t}(f_x) df_x df_y]^{1/2}} \quad (13)$$

Finally, the DMRTD is given by

$$\text{DMRTD} = \frac{\text{SNR}_{th} [\iint W H_{ir,s}^2 H_{mf,s}^2 H_{ir,t}(f_x)^2 H_{mf,t}(f_x)^2 df_x df_y]^{1/2}}{\iint H_0 H_{ir,s} H_{mf,s} H_{ir,t}(f_x) H_{mf,t}(f_x) df_x df_y} \quad (14)$$

where SNR_{th} is the threshold value of SNR for the human eye-brain.

Note that SNR_{th} in Eq. (14) is not necessarily a constant, but a function of spatial frequency. We have also shown that the background temperature is intimately tied to the MRTD formula,⁹ according to which, Eq. (14) should be rewritten to give improved DMRTD as

$$\text{DMRTD}' = \frac{1}{CT_0^3} (\text{DMRTD}) \quad (15)$$

where T_0 represents the background temperature of the target and $C = 7.224 \times 10^{-8} \text{ W/m}^2 \text{ K}^4$ (Ref. 10). The discrepancy, η , between the DMRTD and the improved DMRTD (DMRTD') is given by

$$\begin{aligned} \eta &= \frac{\text{DMRTD}}{\text{DMRTD}'} - 1 \\ &= CT_0^3 - 1 \end{aligned} \quad (16)$$

Figure 3 shows the values of η as a function of T_0 . When T_0 is equal to $C^{1/3}$, i.e., 240.1576 K, the value of η goes to zero.

Equations (14) and (15) combine both the spatial point spread and temporal impulse responses. Equation (14) is a two-dimensional expression; however, the equation describes a problem of three dimensions: two dimensions of space and one of time. Instead of the point light source as shown in Fig. 1, a four-bar target pattern shown in Fig. 4 can be used in the MRTD test. By following the standard MRTD test procedure,¹¹ the DMRTD

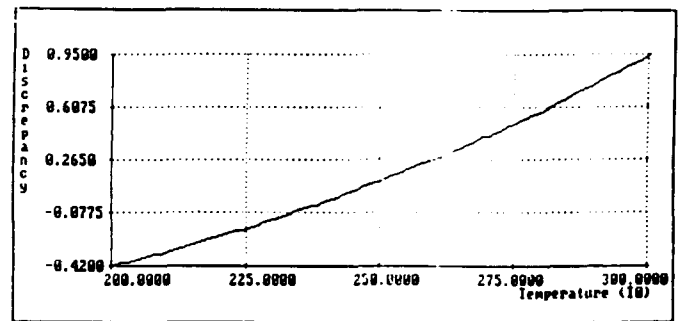


Fig. 3. Discrepancy, η , between DMRTD and DMRTD' as a function of background temperature.

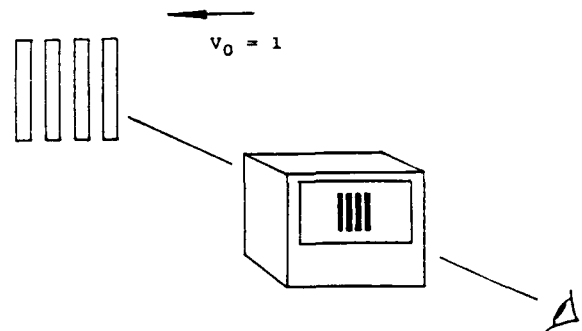


Fig. 4. The experiment setup for evaluating DMRTD.

can be obtained by setting the moving four-bar target to unit velocity along the x -direction.

5. SIMULATION RESULTS

Both Eqs. (14) and (15) are simulated using a computer program, where $\text{SNR}_{\text{th}} = 0.215(f_x)^{0.5509}$ (Ref. 12), $T_0 = 275.5$ K (Ref. 11), and $W = 1$ (for white noise),

$$H_{\text{mf},s} = \begin{cases} 1.75(f/M)^{0.6}, & 0.01 < (f/M) < 0.4 \\ 2.4 \exp[-1.25(f/M) - 0.4]^{1/3}, & 0.4 < (f/M) < 3.0 \end{cases} \quad (17)$$

and

$$H_{\text{ir},t} = (1 + j2\pi f_x \tau)^{-1}, \quad (18)$$

where $\tau = 0.08\text{s}^{5.8}$ and $H_{\text{mf},t}$ is taken from the values of Fig. 5. The DMRTD response using the aforementioned parameters is

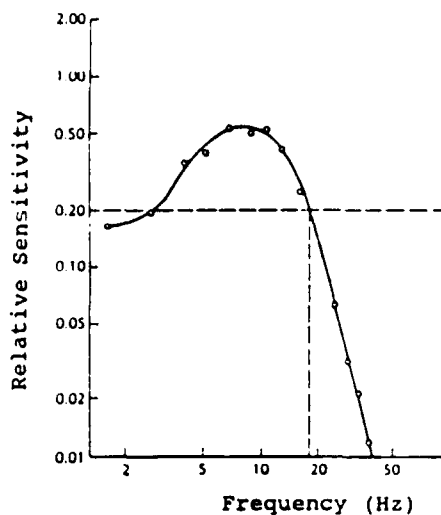


Fig. 5. A typical temporal transfer response of the human eye (after Ref. 13).

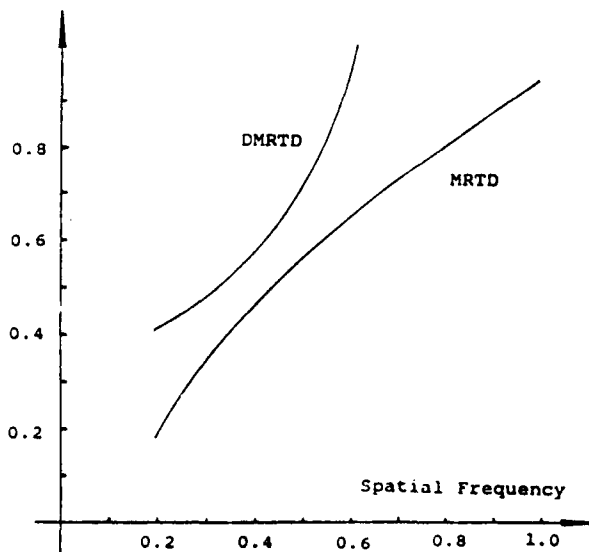


Fig. 6. MRTD and DMRTD characteristics.

plotted in Fig. 6. By comparing the corresponding DMRTD and MRTD curves, we see that the DMRTD values are generally larger than the corresponding MRTD values. This is expected since a larger temperature difference is necessary for discriminating a moving target. Figure 7 shows the plot of DMRTD for different values of τ . With higher values of τ , DMRTD increases. Finally, Fig. 8 shows the DMRTD' response when the background temperature T_0 is changed. The higher T_0 value corresponds to lower DMRTD' values.

6. CONCLUSION

We have developed a device-nonspecific DMRTD formula. Most of its modular terms refer to general subsystem transfer functions without any specific device index. The formula, however, is flexible enough to adapt to almost any IR system although use of the formula may appear inconvenient at first sight because of its lack of system indices.

Equations (14) and (15) represent important measures for characterizing thermal imaging systems capable of displaying dynamic targets. The formulation does not involve any temporal argument. If computer work is necessary, use of the formula means a huge savings in required computing time and memory space.

7. ACKNOWLEDGMENT

The authors would like to acknowledge the research support provided in part by the U.S. Army Research Office contract DAAL03-87-K-0121 with the University of Dayton.

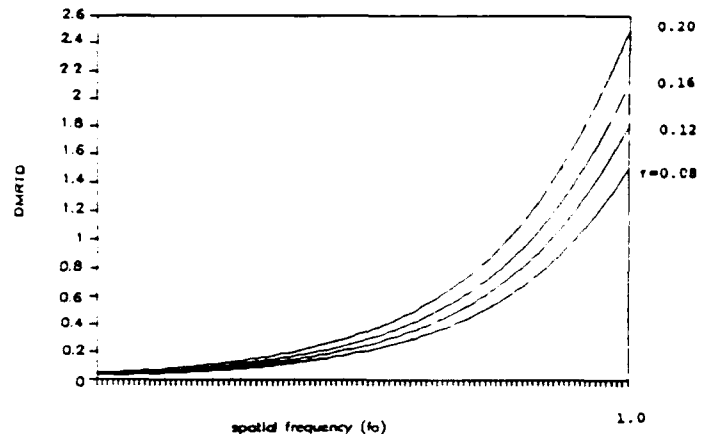


Fig. 7. DMRTD as a function of τ .

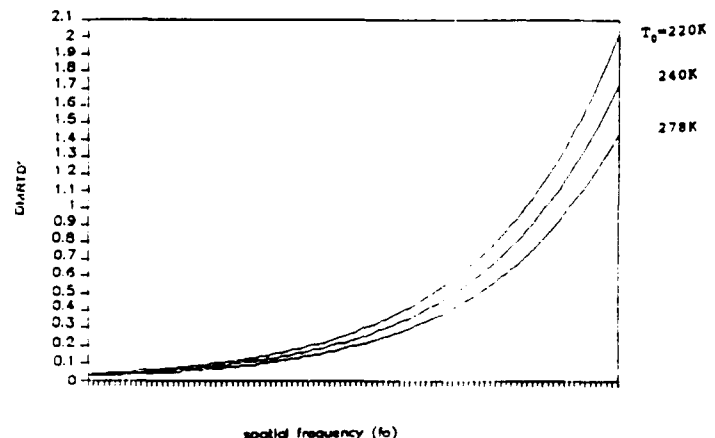


Fig. 8. DMRTD' as a function of T_0 .

8. REFERENCES

1. J. A. Ratches, "Static performance model for thermal imaging system," *Opt. Eng.* 15(6), 525-530 (1976).
2. L. Levi, "On combined spatial and temporal characteristics of optical systems," *Opt. Acta* 17, 869-872 (1970).
3. L. Levi, "Spatiotemporal transfer function: recent developments," *Appl. Opt.* 22, 4038-4041 (1983).
4. X. Shi-ming, "MTF deterioration by image motion in electro-optical imaging system," in *Proc. of Electro-Optics/Laser International UK Conference*, Brighton, England (1982).
5. A. A. S. Awwal, A. K. Cherm, M. A. Karim, and D. L. Moon, "Dynamic modulation transfer function of the display system," *Appl. Opt.* 30, 201-205 (1991).
6. M. L. Gao, M. A. Karim, and S. H. Zheng, "Device nonspecific minimum resolvable temperature difference for infrared imaging systems characterization," *Opt. Eng.* 29(8), 905-910 (1990).
7. A. Papoulis, *The Fourier Integral and Its Applications*, McGraw-Hill Book Company, Inc., New York (1962).
8. A. K. Cherm, A. A. S. Awwal, M. A. Karim, and D. L. Moon, "Restoration of motion-degraded images in electro-optical displays," in *Helmet Mounted Displays*, J. T. Carolla, Ed., Proc. SPIE 1116, 198-207 (1989).
9. M. A. Karim, M. L. Gao, and S. H. Zheng, "Minimum resolvable temperature difference model: a critical evaluation," *Opt. Eng.* 30(11), 1788-1796 (1991).
10. M. A. Karim, *Electro-Optical Devices & Systems*, PWS-Kent Publishing Co., New York (1990).
11. J. T. Wood, W. J. Bentz, T. Pohle, and K. Hepfer, "Specification of thermal imagers," *Opt. Eng.* 15(6), 531-536 (1976).
12. G. C. Holst and A. R. Taylor, "What eye model should we use for MRT testing," in *Infrared Imaging Systems: Design, Analysis, Modeling, and Testing*, G. C. Holst, Ed., Proc. SPIE 1309, 67-75 (1990).
13. T. N. Cornsweet, *Visual Perception*, Academic Press, Inc., New York (1970).



Mohammad A. Karim: Biography and photograph appear with the guest editorial in this issue.



Song H. Zheng is a Ph.D. student in the Electrical Engineering Department at the University of Dayton. Her dissertation research involves the study of optical pattern recognition based on an amplitude-modulated inverse filter. Zheng received her BS degree in mechanical engineering from Shanghai Institute of Mechanical Engineering (China) in 1982 and her MS degree in physics from Eastern Michigan University in 1988. Prior to beginning her MS program, Zheng served as an assistant director of the Shanghai Medical Equipment Research Institute in China.

Ming L. Gao recently completed his Ph.D. in electrical engineering at the University of Dayton. His dissertation research involved the evaluation of display systems and thermal imaging systems. Gao received his BS degree in electronics from Tsinghua University (China) in 1968 and his MS degree in electrical engineering from Hefei Polytechnic University (China) in 1981. Prior to beginning his Ph.D. work, he worked as an engineer for the Liao-yuan Radio Company in China.

Minimum resolvable temperature difference model: a critical evaluation

Mohammad A. Karim, MEMBER SPIE

Ming L. Gao

Song H. Zheng

University of Dayton
Center for Electro-Optics
300 College Park
Dayton, Ohio 45469-0227

Abstract. Discrepancies between the predicted minimum resolvable temperature difference (MRTD) and field performances are indicative of the fact that the modeling of MRTD has certain inherent problems. Several sources for MRTD error are identified. MRTD is also shown to be a special case of a more general minimum resolvable luminance difference (MRLD) measure. The MRLD measure involves absolute temperature and can be used to describe more generic targets.

Subject terms: infrared imaging systems; minimum resolvable temperature difference; luminance; eye-brain; thermal imaging systems.

Optical Engineering 30(11), 1788-1796 (November 1991).

CONTENTS

1. Introduction
2. MRTD formulation consideration
 - 2.1. Eye-brain nonlinearities
 - 2.2. Eye-brain spatial characteristics
 - 2.3. SNR variation
 - 2.4. Temperature effects
3. MRTD evaluation considerations
 - 3.1. Eye-brain randomness
 - 3.2. Nonstandardization errors
4. MRLD formulation
5. Simulations for MRLD
6. Discussion
7. Conclusions
8. References

1. INTRODUCTION

Since Genoud and Sendall's¹ introduction of the minimum resolvable temperature difference (MRTD) concept, many models have been generated for the characterization of thermal imaging systems. The most famous of these is the Night Vision Laboratory (NVL) model,^{2,3} which is the current standard of the U.S. Army. However, experimental MRTD data often differ from that predicted by the NVL model.⁴ Accordingly, many efforts⁵⁻⁹ have been made to update or modify the NVL model. But these efforts haven't been able to account for all of the discrepancies. In this paper, we discuss both the theoretical as well as experimental problems pertaining to the MRTD measure.

MRTD model development involved assumptions that are too ideal. Several important facts such as the background temperature effect, the nonlinearities and spatial characteristics of the human eye-brain system, and the spatial frequency dependent signal-to noise ratio (SNR) were neglected in the development of the MRTD model. In our current work, the impacts of these simplifications are accounted for by adding up their effects on MRTD formulation.

The very basic starting point in the derivation of MRTD is that the IR imaging system signal is merely the temperature difference between target and background. Strictly speaking, this is not correct because an IR imaging system does not test temperature directly. What is detected by an IR imaging system is neither the temperature difference nor temperature itself but the energy radiated from the target and background. Furthermore, the same temperature difference may cause quite a different MRTD value when the absolute temperature of the target (or background) is different.

To overcome the problems stated, a new measure referred to as the minimum resolvable luminance difference (MRLD) may be identified from the point of view of radiated energy. While the MRLD measure is more realistic than the corresponding MRTD measure, it also incorporates the contribution of absolute temperature. MRTD can be used for blackbodies, but not for graybodies or spectrally selected targets. Accordingly, the use of MRTD is somewhat limited because all of the field scenes are of either the gray or spectrally selective type. While most of the laboratory MRTD tests involve blackbody sources, the field test results often correspond to a different set of targets. The discrepancy between the theory and actual data is thus obvious.

2. MRTD FORMULATION CONSIDERATION

2.1. Eye-brain nonlinearities

Every one of the MRTD models developed was based on the concept of linear systems. Accordingly, all components of the MRTD test system, such as the thermal source, the collimating optics, the to-be-tested system, the observer's eye-brain system, and so on, are assumed to be linear subsystems. This assumption is more or less reasonable for all subsystems except the human eye-brain. A popular way of analyzing nonlinear systems, however, is to consider the said nonlinear system as approximately linear and then provide both limitation and errors caused by this approximation.

Human eye-brain response is not linear. In fact, at least two nonlinear visual phenomena exist that may contribute to nonlin-

Invited paper IR-009 received March 25, 1991; revised manuscript received July 8, 1991; accepted for publication July 8, 1991.
© 1991 Society of Photo-Optical Instrumentation Engineers.

ear errors. First, the relationship between the perceived brightness I_p and incident intensity I_{in} is approximately logarithmic.¹⁰ Figure 1 shows the corresponding relationship as well as the linear approximation I'_p of the response where I_b represents the background intensity present on the retina. The linearly approximated perceived brightness can be expressed in terms of the incident intensity by

$$I'_p = \frac{\log(I_b)}{I_b} I_{in} \\ = \log(I_{in}) \left[1 + \frac{I_{in} \log(I_b) - I_b \log(I_{in})}{I_b \log(I_{in})} \right] \quad (1)$$

The second term of Eq. (1), which is a function of both I_b and I_{in} , corresponds to the relative error caused by the linear approximation.

The second nonlinear error encountered in eye-brain modeling is caused by the lateral inhibitory interaction of the human visual system.¹⁰ The inhibitory phenomenon that occurs in the receptor generally inhibits its neighborhood. The strength of inhibition at a point due to an excited receptor is inversely proportional to the distance between the studied point and the receptor, but it is directly proportional to the strength of the excited receptor. Figure 2 shows a typical retinal input and the corresponding retinal output¹⁰ from which it can be inferred that lateral inhi-

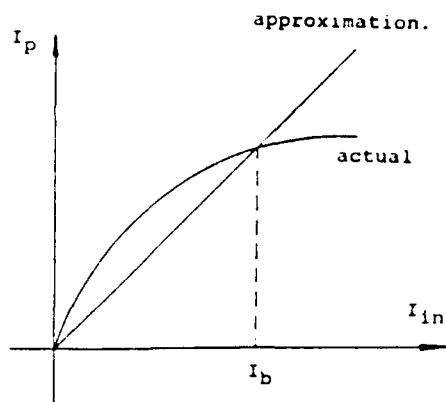


Fig. 1. The incident light intensity versus perceived brightness.

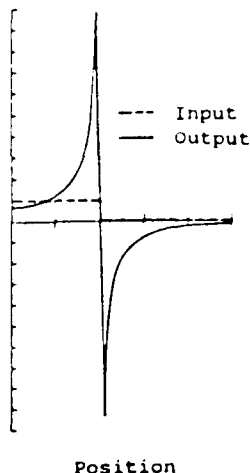


Fig. 2. Retinal light distributions and the corresponding brightness response (after Ref. 10).

bition produces output that peaks at or near regions where the input intensity changes most rapidly. Furthermore, the height of the output is proportional to the spatial rate of change of intensity at the input. The sharper the intensity change, the larger the output.

The sharpness of the input may be described by the derivative of the input light distribution on the retina. The peak-to-peak variation in the output response can be quantified by the product of distance and the derivative of input distribution. Note that the peak-to-peak value, by definition, is the signal used in MRTD formulation. This signal is essentially nonlinear. The top branch of Fig. 3 shows a typical MRTD test system, which includes the transfer function of the eye, H_{mf1} . This particular transfer function, however, is determined by testing a spatial frequency-adjustable sine-wave target in which the effect of inhibition is much less than that on the standard MRTD target. Note that a rectangular-wave target is associated with sharper edges. In other words, a human eye perceives a rectangular-wave target to have a much stronger output (at the edges) than a sine-wave target. In principle, therefore, the to-be-considered H_{mf1} should be derived using the standard four-bar pattern instead of the sine-wave one. Since this is not the case, an auxiliary module is added in parallel to the eye transfer model of Fig. 3 to account for the additional inhibition effect, which is given by $H_{mf2} = C f_x f_y H_t H_r$, where C corresponds to a distance factor that depends on the shape of the input and H_t and H_r , respectively, represent the transfer functions of the target and IR system, and f_x and f_y , respectively, represent spatial frequencies along horizontal and vertical directions. The perceived signal is thus given by

$$s_p = \iint H_t H_r H_{mf1} \left(1 + \frac{4\pi^2 C f_x f_y}{H_{mf1}} \right) df_x df_y \quad (2)$$

The second term of Eq. (2) describes the relative error for the inhibitory effect that is otherwise introduced by the sine-wave target.

The human eye can be empirically modeled as⁷:

$$H_{mf} = \begin{cases} 1.75(f/M)^{0.6}, & 0.01 < (f/M) < 0.4 \\ 2.4 \exp[-1.25(f/M) - 0.4]^{1/3}, & 0.4 \leq (f/M) < 3.0 \end{cases} \quad (3)$$

where f is the spatial frequency of the four-bar target and M is the magnification of the system. The curve for Eq. (3) is shown for comparison along with the Ratches eye model and the response of a lens¹⁰ in Fig. 4. The values pertaining to Campbell's model decrease at lower spatial frequencies because of the built-in inhibitory effect, which is characteristic of an ac amplifier. The ordinary lens does not involve any inhibitory effect and that is why its response is rather similar to that of a dc amplifier. Ratches model, on the other hand, is approximately similar to that of an ordinary lens but with an exponential trend. It is this

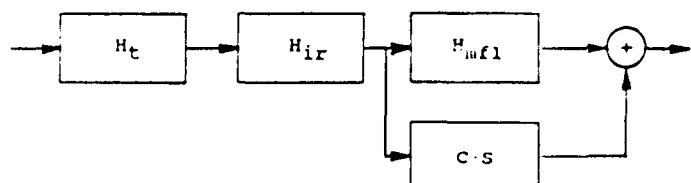


Fig. 3. Block diagram for the MRTD test system.

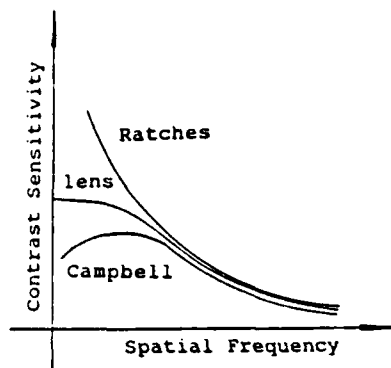


Fig. 4. Contrast sensitivity of different eye-brain models.

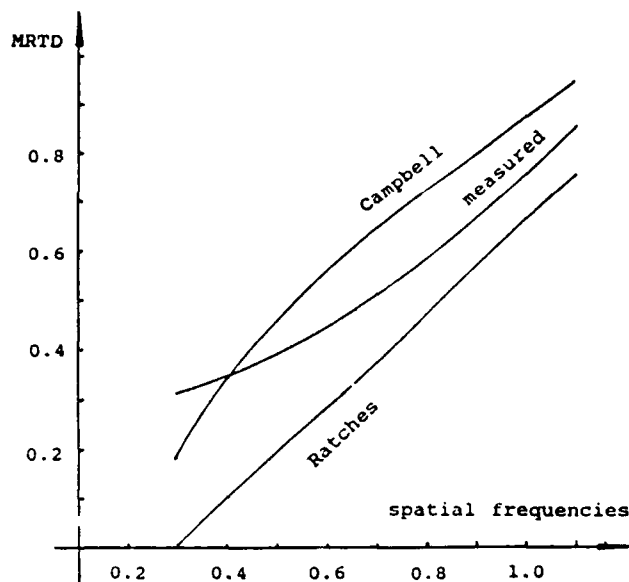


Fig. 5. MRTDs corresponding to different eye-brain models.

latter eye model that results in significant error at lower spatial frequencies. A computer simulation may be used to compute and compare the corresponding MRTDs. Figure 5 shows the measured MRTD characteristics⁷ as well as that corresponding to both Ratches and Campbell eye models.

2.2. Eye-brain spatial characteristics

The two types of light receptors of a human eye retina are cones and rods. The cones respond most effectively in bright environment while the rods respond in the dark. The density distributions of both cones and rods on the retina are not linear. In general, only cones are considered in MRTD evaluation. If the density distribution of human cones were to indicate the sensitivity distribution of the retina, we would notice that the sizes of images on the retina, in general, are significant within a range between near-zero degrees through about 10 deg with retinal sensitivity changing by a factor of 20. In general, therefore, the linear systems theory may not be enough to describe the human eye-brain response.

2.3. SNR variation

Most of the MRTD models use the SNR threshold of the human eye-brain system as a constant, e.g., 2.25, for the complete spatial frequency range.² However, a recent study⁹ has shown that the SNR and spatial frequency f are related by:

$$\text{SNR} = 0.215 (f)^{0.5509} \quad (4)$$

Figure 6 shows the corresponding SNR response. Incorporation of Eq. (4) in the MRTD modeling is expected to improve the overall MRTD measure.

2.4. Temperature effects

As mentioned, in the MRTD test system, what is received by the detector from the to-be-tested device is not the temperature of the target, but the energy radiated by the target. Furthermore, the traditional definition of MRTD is independent of the absolute value of the background temperature; it depends only on the temperature difference between the target and the background. This assumption pertaining to MRTD is expected to affect the corresponding outcome considerably.

According to the Stefan-Boltzmann law, the radiant exitance of a blackbody source¹¹ is:

$$M = \sigma T^4 \quad (5)$$

where T is its temperature and $\sigma = 5.67023 \times 10^{-8} \text{ W/m}^2 \text{ K}^4$. Furthermore, if the source is Lambertian, the radiance L is found to be

$$L = M/\pi = C'T^4 \quad (6)$$

where $C' = \sigma/\pi$. Consider T_0 to be the background temperature and ΔT the temperature difference between the target and the background; then the radiance difference ΔL between the target and the background is given by

$$\begin{aligned} \Delta L &= C'(T_0 + \Delta T)^4 - C'T_0^4 \\ &= C'[(T_0^4 + 4T_0^3\Delta T + 6T_0^2\Delta T^2 + 4T_0\Delta T^3 + \Delta T^4) - T_0^4] \\ &= C'[4T_0^3\Delta T + 6T_0^2\Delta T^2 + 4T_0\Delta T^3 + \Delta T^4] \end{aligned} \quad (7)$$

Equation (7) can be simplified by ignoring the higher order ΔT terms to give

$$\begin{aligned} \Delta L &= 4C'T_0^3\Delta T \\ &= CT_0^3\Delta T \end{aligned} \quad (8)$$

where $C = 4C'$.

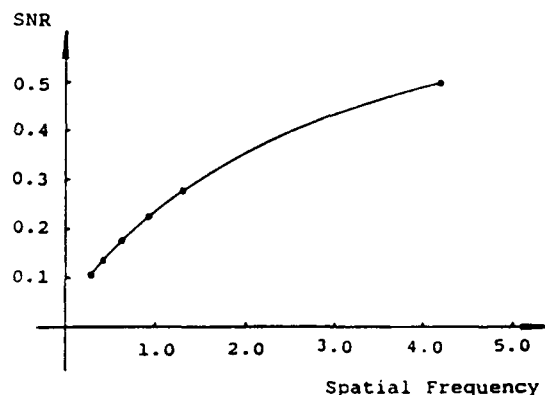


Fig. 6. Experimentally derived SNR as a function of spatial frequency (after Ref. 9).

Considering now that what is received by the to-be-tested device is not temperature, but the energy irradiated by both the target and the background, the perceived signal⁵ is given by

$$s_p = \Delta L \iint H_t H_{ir} H_{mf} df_x df_y \quad (9)$$

Since the signal is defined in terms of its peak-to-peak value, the corresponding two-dimensional image distribution on the display screen is:

$$e_d(x,y) = \Delta L i_d(x,y) \quad (10)$$

where ΔL is the luminance difference between the target and background and $i_d(x,y)$ is the normalized distribution of the target picture incident on the display screen.

Since the perceived noise⁵ is given by

$$n_p = \left(\iint WH_{ir}^2 H_{mf}^2 df_x df_y \right)^{1/2} \quad (11)$$

where W is the input noise power spectral density, the SNR is given by

$$\text{SNR} = \frac{\Delta L \iint H_t H_{ir} H_{mf} df_x df_y}{\left(\iint WH_{ir}^2 H_{mf}^2 df_x df_y \right)^{1/2}} \quad (12)$$

and, therefore,

$$\Delta L = \frac{\text{SNR}_{th} \left(\iint WH_{ir}^2 H_{mf}^2 df_x df_y \right)^{1/2}}{\iint H_t H_{ir} H_{mf} df_x df_y} \quad (13)$$

Equation (13) defines an energy measure that may be referred to as the blackbody MRLD. By means of Eqs. (8) and (13), ΔT can be derived to give

$$\Delta T = \left(\frac{1}{CT_0^3} \right) \left[\frac{\text{SNR}_{th} \left(\iint WH_{ir}^2 H_{mf}^2 df_x df_y \right)^{1/2}}{\iint H_t H_{ir} H_{mf} df_x df_y} \right] \quad (14)$$

The second factor on the right side of Eq. (14) is the classical MRTD.⁵ The improved MRTD, denoted by MRTD', is thus given by

$$\text{MRTD}' = \frac{1}{CT_0^3} (\text{MRTD}) \quad (15)$$

which shows that the true MRTD value is indeed influenced by the background temperature. Reference 12 specifies the range of 273 to 278 K for T_0 . A simple computation shows that T_0 changes within this range may contribute to an error of 6%.

3. MRTD EVALUATION CONSIDERATIONS

3.1. Eye-brain randomness

To a great extent, the observers involved in the recognition of the standard MRTD test pattern during the characterization of infrared imaging systems respond randomly. Accordingly, the measured values should be interpreted in a probabilistic manner. In the study of random events, it is not enough to discuss only the mean of the sample space. Consider, for example, that in the opinion of ten observers, the mean MRTD value is, say, 1.5 K at a spatial frequency of 0.69 cycles/mrad. Correspondingly, the true MRTD value for a 90% confidence level lies within the range 1.5 ± 0.73 . The ΔT range between 0.77 and 2.23 K is referred to as the confidence interval. For the given confidence level, all of the values that lie within this range are possible MRTD values. We can reasonably assume that the MRTD measurements obey a Gaussian distribution. The confidence interval is $\bar{x} \pm z_{\alpha/2}(\sigma/n)$, where \bar{x} is an approximation of the true value (in our case, it is the average value obtained from all observers), z represents the normalized Gaussian distribution parameter, α is the value of the confidence level, n is the sample size, and σ is the standard deviation.¹³ Based on data from Ref. 14, we may obtain the standard deviation as a function of spatial frequency as shown in Fig. 7.

For a constant value of \bar{x} , α , and σ , the confidence interval is a function of n only. Figure 8 shows the relationship between the confidence interval CI and n for two particular spatial frequencies. The smaller values of n correspond to larger values of CIs. Therefore, if more accurate MRTD data are to be expected, n must be made larger. For example, a total of 550 observers will be required in the MRTD test to achieve a 90% confidence interval of $\bar{x} \pm 0.1$ at a spatial frequency of 0.69 cycles/mrad. Also, if the data were to be collected at a higher spatial frequency, say, 1.15 cycles/mrad, the variance requirement would be so large that a few thousand observers might be needed for the MRTD test. Unfortunately, in most of the MRTD tests, the number of observers is usually between two and five while the accuracy discussed is often better than 0.1.

3.2. Nonstandardization errors

Although Ref. 13 specifies the MRTD test procedure, the detailed test processes are quite different for each of the test groups. Typical nonstandardization problems associated with MRTD measurements include aspects related to distance between the

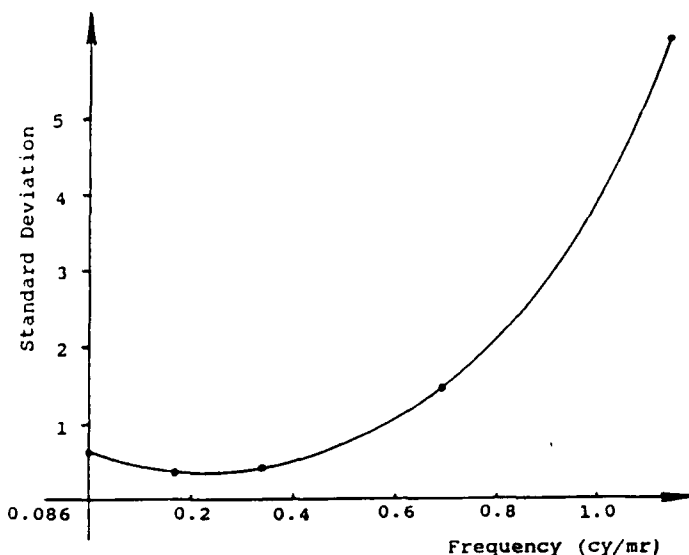


Fig. 7. The deviation of contrast threshold versus spatial frequency.

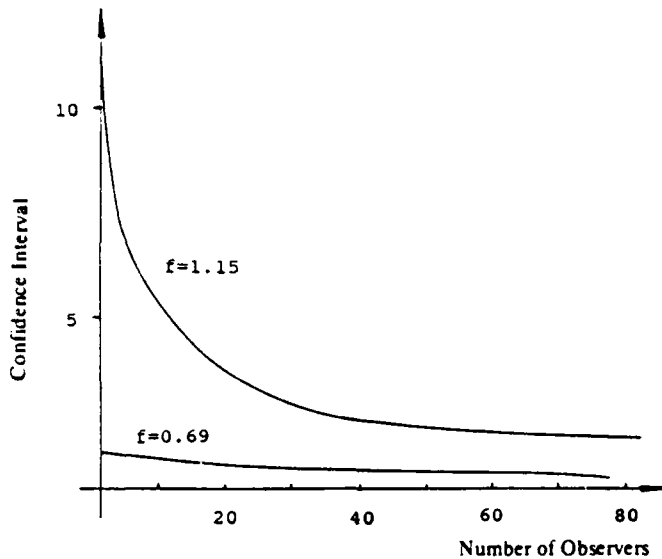


Fig. 8. Confidence interval versus the number of observers.

display screen and the observer, background brightness, binocular issues, and strain. The experimental data shown in Fig. 9 reveal that for a constant viewing angle the contrast sensitivity is relatively independent of the viewing distance.¹⁵ This indicates that if the observer were to adjust the viewing distance while keeping the viewing angle invariant for every test situation, both the spatial frequency of image and the perceived spatial frequency remain unchanged. In other words, it is quite misleading to refer to the test result as being caused by the eye-brain's transfer function when the distance is allowed to be adjusted during the test. In practice, many of the MRTD tests do not take this fact into consideration.

Figure 10 shows two sets of test data for different background brightnesses. In general, the contrast sensitivity increases with background luminance. However, during the MRTD test, the display screen brightness is often adjusted by the observer. This is expected to cause considerable additional inconsistencies between results obtained by different observers. Again, the MRTD formulations are based on a monocular eye model while MRTD

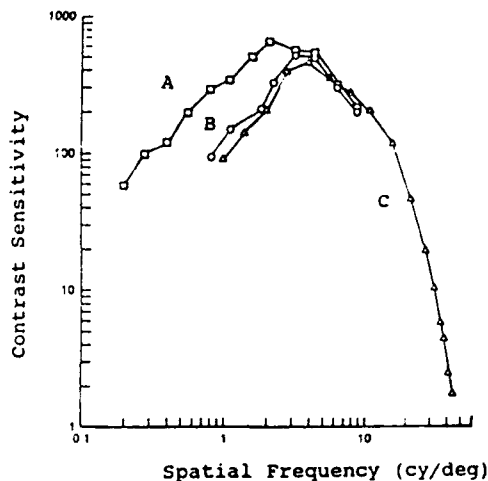


Fig. 9. Contrast sensitivity for sine-wave gratings at a luminance value of 500 cd/m²: (A) viewing distance 57 cm, aperture 10 × 10; (B) viewing distance 57 cm, aperture 2 × 2; and (C) viewing distance 285 cm, aperture 2 × 2 (after Ref. 15).

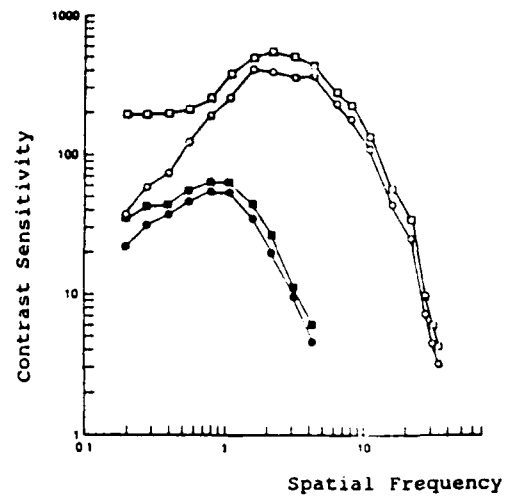


Fig. 10. Contrast sensitivity for two different luminances. The circles are for sine-wave gratings and the squares are for square-wave gratings. The upper pair is for 500 cd/m², while the lower pair is for 0.05 cd/m² (after Ref. 9).

measurements are conducted using both eyes. This is perhaps because the binocular eye model is not too well understood. Last, each of the observers expends great effort during an MRTD test. Since, over a prolong period, human eye-brain sensitivity decreases, the human eye-brain system may not be treated as time-invariant.

4. MRLD FORMULATION

The MRLD corresponding to the blackbody scene was derived in Eq. (13) and is related to MRTD by

$$\text{MRLD}_B = CT_0^3(\text{MRTD}) \quad (16)$$

where MRLD_B reduces to the classical MRTD when T_0 is equal to $(1/C)^{1/3}$. Again, since MRLD and MRTD are linearly related, the new measure is also a function of spatial frequency. In this section, we extend the MRLD definition to include graybody and spectrally selective scenes.

In practice, the scene is referred to as a graybody if an extra radiation source exists, such as the moon in the background. If the target and background are both Lambertian, the total luminances of target and background are respectively given by

$$L_t = 1/\pi[e_t M_t + r_t(E_b + E_s)] \quad (17)$$

$$L_b = 1/\pi(e_b M_b + r_b E_s) \quad (18)$$

where E , r , and e represent total incident illuminance, reflectance, and emittance, respectively, while the subscripts b , s , and t refer to the background, extra source, and target, respectively. Note that in Eq. (18) the effect of illuminance from the target has been ignored. Accordingly, the luminance difference ΔL can be expressed as

$$\begin{aligned} \Delta L &= L_t - L_b \\ &= 1/\pi[e_t M_t + r_t(E_b + E_s) - e_b M_b - r_b E_s] \\ &= 1/\pi[e_t \sigma T_t^4 + r_t E_b + E_s(r_t - r_b) - e_b \sigma T_b^4] \end{aligned} \quad (19)$$

But since $T_i = T_b + \Delta T$, Eq. (19) reduces to

$$\Delta L = 1/\pi [e_i \sigma (T_b^4 + 4T_b^3 \Delta T + 6T_b^2 \Delta T^2 + 4T_b \Delta T^3 + \Delta T^4) + r_i E_b + E_s(r_i - r_b) - e_b \sigma T_b^4] \quad (20)$$

By ignoring the higher order terms, therefore, the graybody MRLD can be given by

$$\text{MRLD}_G = 1/\pi [4e_i \sigma T_b^3 (\text{MRTD}) + \sigma T_b^4 (e_i - e_b) + r_i E_b + E_s(r_i - r_b)] \quad (21)$$

Again, MRLD reduces to MRTD when $e_i = e_b = 1$, $r_i = r_b = 0$, and T_0 is equal to $(1/C)^{1/3}$.

A source is referred to as spectrally selective when its emissivity is dependent on the wavelength. For a spectrally selective target and spectrally selective background, the total luminance L_i and L_b are respectively given by

$$L_i = 1/\pi (M_{in} + r_{in} E_{bn} + r_{in} E_s) \quad (22)$$

$$L_b = 1/\pi (M_{bn} + r_{bn} E_s) \quad (23)$$

where the subscripts in and bn refer to the spectrally selective target and spectrally selective background, respectively, such that

$$M_{in} = \int_{-\infty}^{\infty} e_{in} M_{in}(\lambda) d\lambda \quad (24)$$

$$M_{bn} = \int_{-\infty}^{\infty} e_{bn} M_{bn}(\lambda) d\lambda \quad (25)$$

Also, from the definition of total emissivity of the spectrally selective scene, we know that

$$e_{in} = \frac{M_{in}}{M_i} \quad (26)$$

$$e_{bn} = \frac{M_{bn}}{M_b} \quad (27)$$

Thus, we have

$$M_{in} = e_{in} M_i = e_{in} \sigma T_i^4 \quad (28)$$

$$M_{bn} = e_{bn} M_b = e_{bn} \sigma T_b^4 \quad (29)$$

Equations (22) and (23) can be used to obtain the corresponding spectrally selective MRLD, MRLD_N , as

$$\text{MRLD}_N = 1/\pi [4e_{in} \sigma T_b^3 (\text{MRTD}) + \sigma T_b^4 (e_{in} - e_{bn}) + r_{in} E_{bn} + E_s(r_{in} - r_{bn})] \quad (30)$$

The generalized MRLD, therefore, may be given by

$$\text{MRLD} = 1/\pi [4e_i \sigma T_b^3 (\text{MRTD}) + \sigma T_b^4 (e_i - e_b) + r_i E_b + E_s(r_i - r_b)] \quad (31)$$

When the emittances are equal to unity and the reflectances are zero, the generalized MRLD reduces to that of a blackbody, which in turn reduces to the classical MRTD when T_0 is equal to $(1/C)^{1/3}$.

5. SIMULATIONS FOR MRLD

In this section, Eq. (31), is used to simulate several important MRLD features. Figures 11, 12, and 13 show the influence of the reflectances r_i and r_b on MRLD. In Fig. 11(a), the solid curve corresponds to $r_i = r_b = 0$, while the dashed one indicates the situation when $r_i = 0.9$ and $r_b = 0$ with $T_b = 240.1576$ K, $e_i = e_b = 1$, and $E_i = E_b = 1$. Figure 12 shows the corresponding case where r_b is changed from 0 to 0.5 while $r_i = 0$. Figure 13 shows the case where the solid curve corresponds to $r_i = r_b = 0$ and the dashed one indicates the situation when $r_i = 0.9$ and $r_b = 0.5$. In practical tests, the Nyquist frequency is considered as the reference spatial frequency at which an empirically determined value is assumed to be equal to the predicted one. Figure 11(b) shows the corresponding situation, which we may refer to as the normalized diagram, when the dashed curve is moved upward by a value equal to the MRLD difference (between the two at Nyquist frequency). We find that the two curves in each case are absolutely matched throughout the whole range.

Figures 14, 15, and 16 show the influences of E_b and E_s on MRLD. In Fig. 14, the dashed curve represents the case for which $E_b = 1.0$ and $E_s = 1.5$, while the solid curve corresponds to the case for which $E_b = 2.5$ and $E_s = 1.5$. In Fig. 15, the dashed curve represents the case for which $E_b = 2.5$ and $E_s = 0.5$, while the solid curve corresponds to $E_b = 2.5$ and $E_s = 1.5$. Finally, in Fig. 16, the dashed curve corresponds to $E_b = 2.0$ and $E_s = 0.5$, and the solid one corresponds to $E_b = 2.5$ and $E_s = 1.5$. In all of these cases, we used $e_i = e_b = 1$, $r_i = 0.9$, $r_b = 0.5$, and $T_0 = 240.1576$ K. Figures 14(b) through 16(b) show the corresponding normalized diagrams, which match throughout the whole range of frequency.

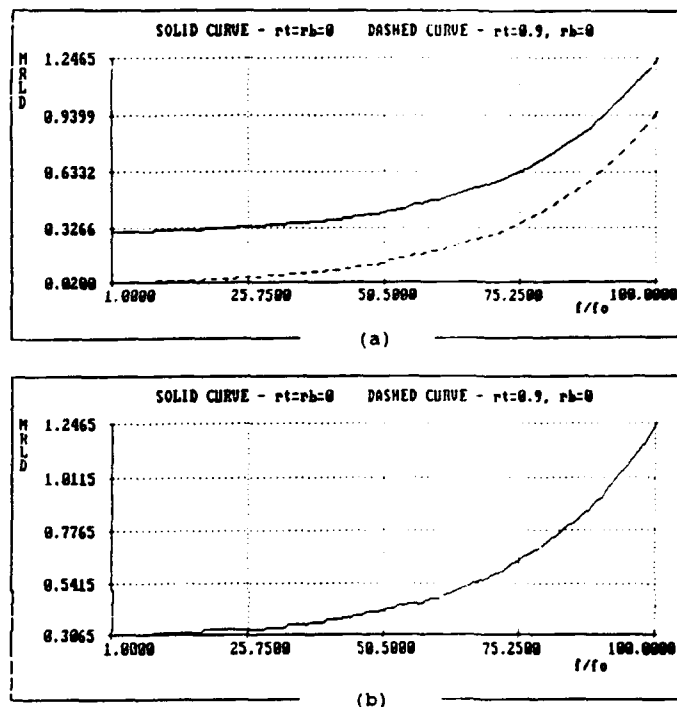
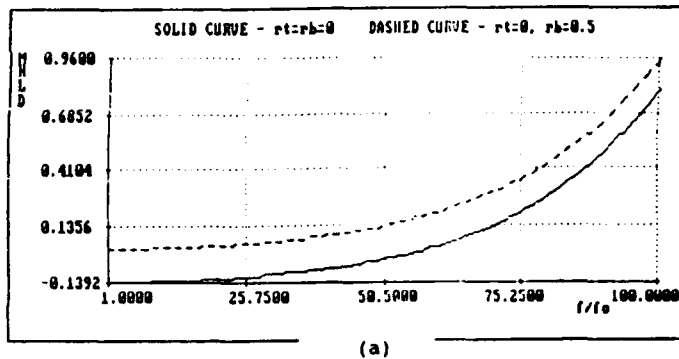
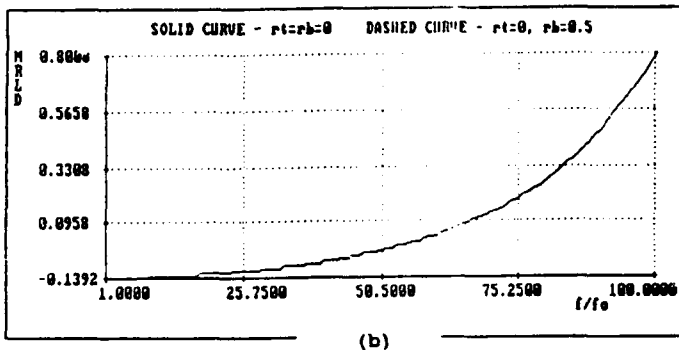


Fig. 11. (a) Influence of reflectances on MRLD and (b) normalized diagram of (a).

The effect of the background emittance e_b on MRLD is shown in Fig. 17(a). The dashed curve is for $e_b = 0.75$; the solid one is for $e_b = 0.79$ when $e_t = 0.8$, $r_t = r_b = 0$, and $T_0 = 240.1576$ K. Again, the corresponding normalized diagram is shown in Fig. 17(b), which is matched throughout the whole range of frequency.

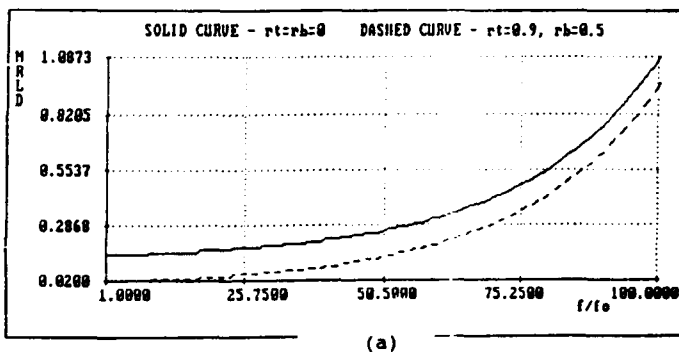


(a)

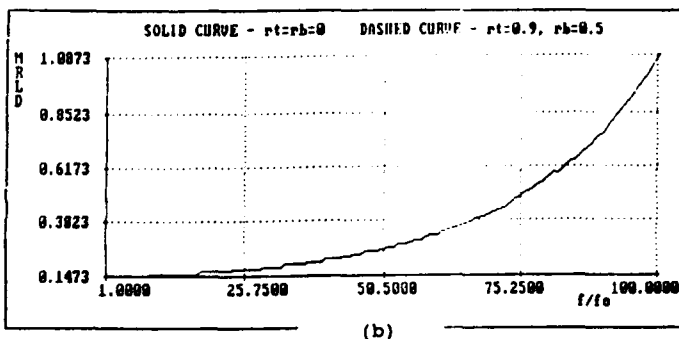


(b)

Fig. 12. (a) Influence of reflectances on MRLD and (b) normalized diagram of (a).



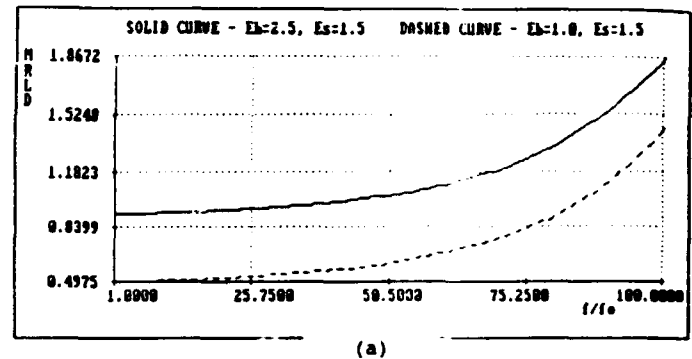
(a)



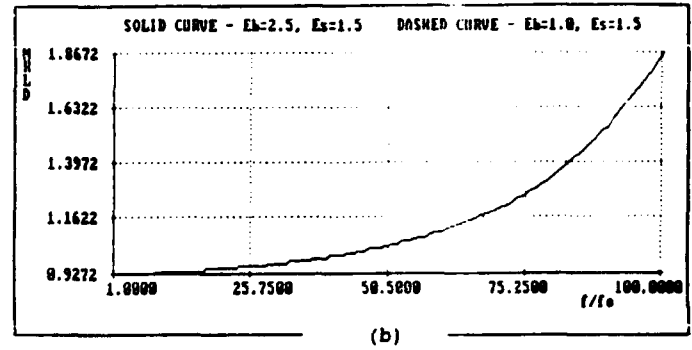
(b)

Fig. 13. (a) Influence of reflectances on MRLD and (b) normalized diagram of (a).

Figures 18(a) and 19(a) show MRTD curves for different target emittances e_t when, for example, $r_t = r_b = 0$ and $T_0 = 240.1576$ K. In Fig. 18(a) the solid curve represents $e_t = e_b = 1$, and the dashed curve is for $e_t = 0.9$ and $e_b = 1.0$. In Fig. 19(a) the dashed curve is for $e_t = e_b = 1$, and the solid curve is for $e_t = 0.8$ and $e_b = 0.79$. Figures 18(b) and 19(b) show the

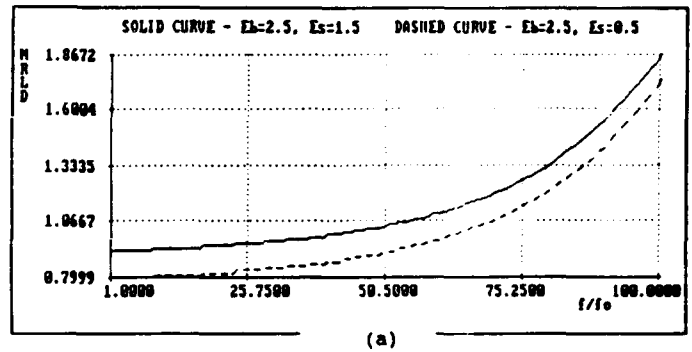


(a)

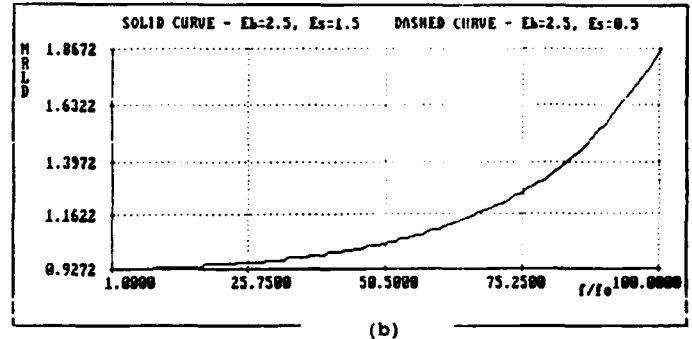


(b)

Fig. 14. (a) Influence of illuminances on MRLD and (b) normalized diagram of (a).



(a)



(b)

Fig. 15. (a) Influence of illuminances on MRLD and (b) normalized diagram of (a).

corresponding normalized diagram where, interestingly, the curves are not matched over the range of frequency considered. Finally, Fig. 20(a) shows the MRLD values for different background temperatures when, for example, $e_t = e_b = 1$ and $r_t = r_b = 0$. The dashed curve is the traditional MRTD, i.e., when $T_0 = 240.1576$ K; and the solid curve represents the situation when $T_0 = 278$ K. Figure 20(b) shows the corresponding normalized diagram where the curves are also not matched.

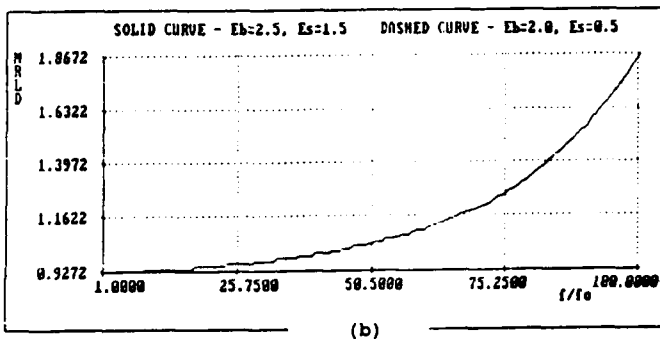
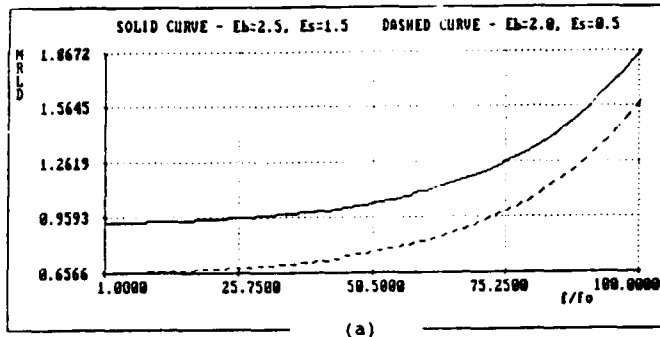


Fig. 16. (a) Influence of illuminances on MRLD and (b) normalized diagram of (a).

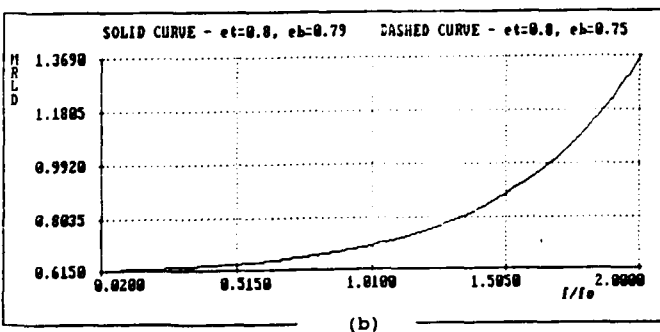
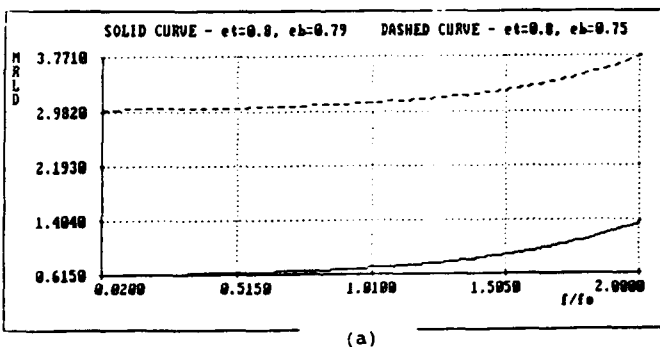


Fig. 17. (a) Influence of background emittance on MRLD and (b) normalized diagram of (a).

6. DISCUSSION

The concept of MRTD is based on the blackbody environment. However, we are also interested in the behaviors of graybody and colored body environments for two reasons: (1) for estimating errors encountered in an actual MRTD test environment and (2) for generalizing the MRTD. Since MRLD is a more generalized version of MRTD, the study of MRLD is expected

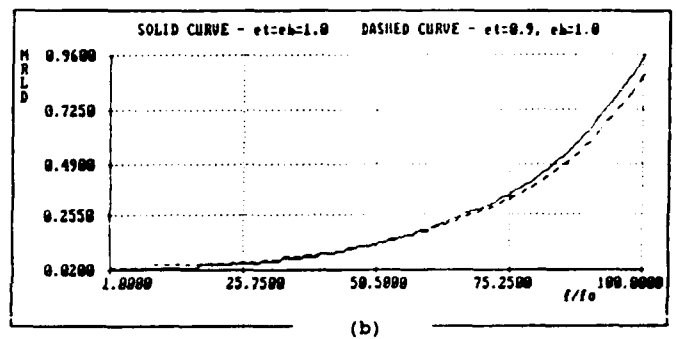
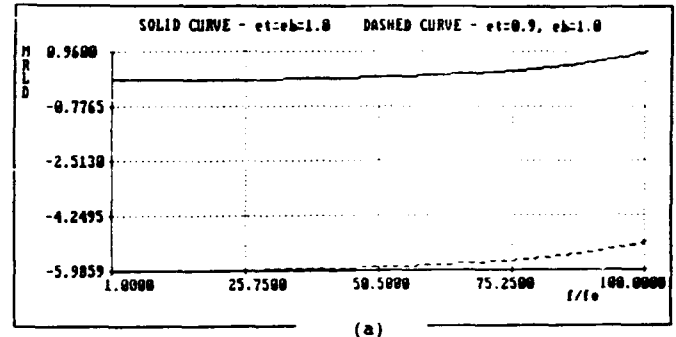


Fig. 18. (a) Influence of target emittance on MRLD and (b) normalized diagram of (a).

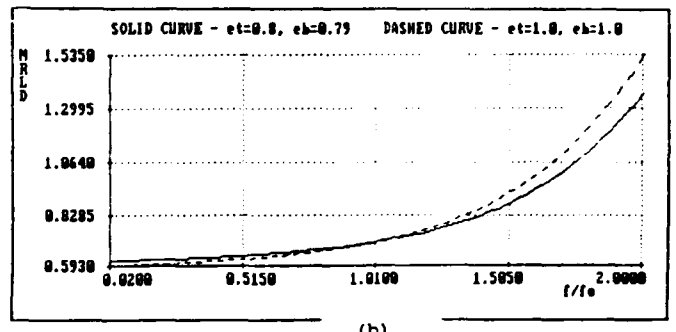
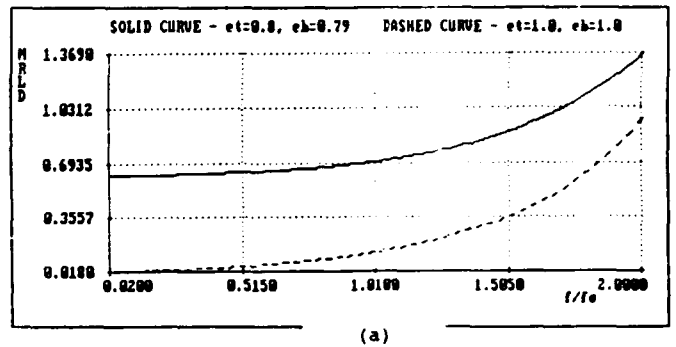


Fig. 19. (a) Influence of target emittance on MRLD and (b) normalized diagram of (a).

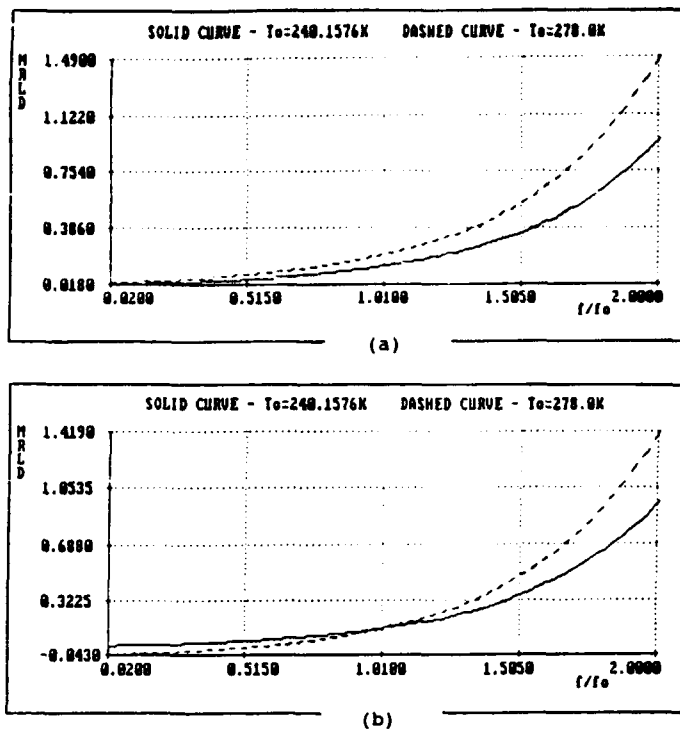


Fig. 20. (a) Influence of background temperature on MRLD and (b) normalized diagram of (a).

to reveal MRTD characteristics for different environment-related parameters.

Equation (31) gives the MRLD formulation, which is affected by three parameters: emittance, reflectance, and illuminance. All three parameters affect MRLD in certain ways. Considering MRTD as the argument in Eq. (31), r , E , and e_b affect MRTD only in terms of the intercept along the MRLD axis, which is evident in Figs. 11 through 16. These parameters affect only the position of the MRTD curve, so the two curves are absolutely matched when the two Nyquist points are matched. Accordingly, the corresponding MRTD errors can be corrected easily by properly tuning the IR system. The parameter e_t , however, affects MRTD both in terms of the slope and ordinate-intercept as shown by Fig. 17(b). This error cannot be eliminated by any means. Note that the discrepancy shown in Fig. 19 corresponds to only a 1% emittance difference, which exists between target and background. Therefore, the standard MRTD test, if it is to deliver accurate measurements, must incorporate the fact that both the target and background are exact blackbodies. In reality, this condition is never met. This is perhaps why the predictions of MRTD are optimistic at lower spatial frequencies and pessimistic at higher spatial frequencies when compared to laboratory measurements. Figures 18(b) and 19(b) similarly justify the fact that emittance is also a critical parameter for accuracy.

Besides these effects, the absolute temperature of background (or target) affects the MRTD very significantly. Figure 20 shows the corresponding situation. The background temperature is set at 240.1576 K for the traditional MRTD, which is shown in Fig. 20 by the dashed curve. The solid curve corresponds to a background temperature of 278 K, which is at the highest end of the range. The maximum error encountered thereby is 55%. Thus, the background temperature is also a critical condition for MRTD accuracy. Thus, the standard specification for an MRTD test must specify the background temperature with a certain specific temperature rather than a range of temperatures.

7. CONCLUSIONS

MRTD formulation is associated with a number of error sources. The most important of these is traced back to eye-brain modeling. In general, the eye-brain model is dependent on the target's shape. Accordingly, an eye-brain model based on the standard four-bar target should only be used for calculating MRTD. Furthermore, the eye model for the signal and that for the noise are not the same.

The discrepancies between experimental data as well as that between data and theory can be traced to two sources: theory as well as experimental conditions. For reliable comparison between the predicted and measured data, a standardized and unambiguous test setup needs to be defined.

We have developed a novel MRLD measure to characterize IR imaging systems. It has the dimension of watt per unit area, while MRTD has the dimension of temperature. MRLD measurements involve the absolute temperature of the target (or background). Furthermore, MRLD is general enough and is not limited to blackbodies. It can be shown that MRTD is a special case of MRLD and that MRTD can be obtained from blackbody MRLD by setting T_0 equal to $(1/C)^{1/3}$.

8. REFERENCES

1. J. M. Lloyd, *Thermal Imaging System*, Plenum Press, New York (1975).
2. J. A. Ratches, W. R. Lawson, L. P. Obert, R. J. Bergemann, T. W. Cassidy, and J. M. Swenson, "Night vision laboratory static performance model for thermal imaging systems," U.S. Army Electronics Command Report 7043 (1975).
3. J. A. Ratches, "Static performance model for thermal imaging systems," *Opt. Eng.* 15(6), 525-530 (1976).
4. W. McCracken and L. Waisfeiner, "MRTD as a figure of merit," in *Thermal Imaging*, Proc. SPIE 636, 31-35 (1986).
5. M. L. Gao, M. A. Karim, and S. H. Zheng, "Device nonspecific minimum resolvable temperature difference for infrared imaging systems characterization," *Opt. Eng.* 29(8), 905-910 (1990).
6. G. M. Cuthbertson, L. G. Shadrake, and N. J. Short, "A technique for the objective measurement of MRTD," in *Infrared Technology And Applications*, Proc. SPIE 590, 179-192 (1985).
7. J. G. Vortman and A. Bar-Lev, "Improved MRTD model for IR imaging system," in *Infrared Technology and Applications*, Proc. SPIE 590, 193-204 (1985).
8. W. L. Wolfe, "Error in minimum resolvable temperature difference charts," *Infrared Physics*, Vol. 17, pp. 375-379 (1977).
9. G. C. Holst and A. R. Taylor, "What eye model should we use for MRT testing," in Proc. SPIE 1309, 67-75 (1990).
10. T. N. Cornsweet, *Visual Perception*, Academic Press, New York (1970).
11. M. A. Karim, *Electro-Optical Devices and Systems*, PWS-Kent Publishing Company, Boston (1990).
12. J. T. Wood, W. J. Bentz, T. Pohle, and K. Helfer, "Specification of thermal imagers," *Opt. Eng.* 15(6), 531-536 (1976).
13. G. R. Cooper and C. D. McGillem, "Probabilistic methods of signal and system analysis," CBS College Publishing, New York (1986).
14. T. R. Corwin, N. B. Carlson, and E. Berger, "Contrast sensitivity norms for the Mentor B-VAT II-SG video acuity tester," *Optometry Vision Sci.* 66(12), 864-870 (1989).
15. F. W. Campbell and J. G. Robson, "Application of Fourier analysis to the visibility of gratings," *J. Physiol.* 197, 551-566 (1968).

Mohammad A. Karim: Biography and photograph appear with the guest editorial in this issue.

Ming L. Gao: Biography and photograph appear with the paper "Device nonspecific dynamic performance model for thermal imaging systems" in this issue.

Song H. Zheng: Biography and photograph appear with the paper "Device nonspecific dynamic performance model for thermal imaging systems" in this issue.